DIRAC MATERIALS WITH SPIN-ORBIT (SO) COUPLING

By
RUCHI SAXENA
PHYS08201204005

Harish-Chandra Research Institute, Allahabad

A thesis submitted to the
Board of Studies in Physical Sciences
In partial fulfillment of requirements
for the Degree of
DOCTOR OF PHILOSOPHY
of
HOMI BHABHA NATIONAL INSTITUTE

August, 2018

Homi Bhabha National Institute[1]

Recommendations of the Viva Voce Committee

As members of the Viva Voce Committee, we certify that we have read the dissertation prepared by Ruchi Saxena entitled "Dirac Materials with Spin-Orbit (SO) Coupling" and recommend that it may be accepted as fulfilling the thesis requirement for the award of Degree of Doctor of Philosophy.

Chairman - Prof. Pinaki Majumdar		**Date:** 26-12-18
Guide / Convener – Prof. Sumathi Rao		**Date:** 26/12/18
Examiner – Prof. G. J. Sreejith		**Date:**
Member 1- Prof. Prasenjit Sen		**Date:** 26/12/18
Member 2- Prof. Ashoke Sen		**Date:** 26/12/18
Member 3- Prof. G. V. Pai	Deceased	**Date:**

Final approval and acceptance of this thesis is contingent upon the candidate's submission of the final copies of the thesis to HBNI.

I/We hereby certify that I/we have read this thesis prepared under my/our direction and recommend that it may be accepted as fulfilling the thesis requirement.

Date: 26.12.2018

Place: Allahabad

Prof. Sumathi Rao
Guide

[1] This page is to be included only for final submission after successful completion of viva voce.

STATEMENT BY AUTHOR

This dissertation has been submitted in partial fulfillment of requirements for an advanced degree at Homi Bhabha National Institute (HBNI) and is deposited in the Library to be made available to borrowers under rules of the HBNI.

Brief quotations from this dissertation are allowable without special permission, provided that accurate acknowledgement of source is made. Requests for permission for extended quotation from or reproduction of this manuscript in whole or in part may be granted by the Competent Authority of HBNI when in his or her judgment the proposed use of the material is in the interests of scholarship. In all other instances, however, permission must be obtained from the author.

Ruchi Saxena

DECLARATION

I, hereby declare that the investigation presented in the thesis has been carried out by me. The work is original and has not been submitted earlier as a whole or in part for a degree / diploma at this or any other Institution / University.

Ruchi Saxena

List of publications arising from the thesis

Journal

1. "Brillouin Wigner Theory for Floquet Topological Phase Transitions in Spin-orbit Coupled Materials", Priyanka Mohan, Ruchi Saxena, Arijit Kundu, *PRB 94, 235419*, **2016** [Arxiv: 1609.06504/cond-mat]

2. "Conductance, valley and spin polarizations, and tunneling magnetoresistance in ferromagnetic-normal-ferromagnetic junctions of silicene", Ruchi Saxena, Arijit Saha, Sumathi Rao, *PRB 92, 245412*, **2015** [Arxiv: 1507.04225/cond-mat]

3. "Bulk-edge correspondence and new topological phases in periodically driven spin-orbit coupled materials in the low frequency limit", Ruchi Saxena, Sumathi Rao, Arijit Kundu, *Arxiv:1712.05916/cond-mat*, **2017**

Conferences/Schools

1. "**Emergent topological phases in periodically driven SO-coupled materials and their exotic bulk-edge correspondence**" - School and Workshop on Fundamentals on Quantum Transport at ICTP, held at Italy, 31 Jul - 11 Aug 2017.

2. "**XXIV International Summer School Nicolas Cabrera on Quantum Transport in Topological Materials** held at INC, Madrid, 4 - 8 September 2017.

Ruchi Saxena

DEDICATIONS

For my parents,
to have faith in me.
For my soulmate Gaurav,
to stand by me all along.

ACKNOWLEDGEMENTS

I express my foremost gratitude to my supervisor Sumathi Rao for continuous support, motivation and patience during these years in Ph.D. Her spirited and resilient personality always propelled me to overcome the stressful period of my academic life at HRI. A special thanks to her! I sincerely thank Ashoke Sen, Pinaki Majumdar, The Late G. V. Pai, Prasenjit Sen for their invaluable feedbacks from time to time but especially after extension period each year. The phenomenal discussions with my collaborators Arijit Kundu, Arijit Saha, Sourin Das and Priyanka Mohan were imperative. I express my sincere appreciation for them. I am very happy to name a few faculty members who have helped me to fertilise research skills over these years - Sumathi Rao, Ashoke Sen, Rajesh Gopakumar, Pinaki Majumdar, Prasenjit Sen, Aditi Sen and The Late G. V. Pai. Thanks a million to each of them!

I had many useful discussions with members of the Condensed Matter group at HRI and, for that, I would like to thank Abhishek Joshi, Udit Khanna, Samrat Kadge, Sauri Bhattacharyya, Arijit Datta, Dibya Kanti Mukherjee, Ajanta Maity and Krishna Mohan for their precious time. I thank to my dear friends at HRI with whom I had numerous enlightened conversations both on academic as well as non-academic matters which have had made a difference in my perception - Sitender Pratap Kashyap, Mritunjay Kumar Verma, Deepak Tiwari, Kasinath Das. I hardly find words to thank each of them for several diverse reasons I am unable to briefly pen down here. There are still many more wonderful people left to thank whom I lovingly remember but unfortunately, cannot list them all here.

Inevitably, this thesis is a witness of hidden affection of my family. I am beholden to my parents for bringing me up to the level where I can withstand against any misery of life and more than that, to have an opportunity to comprehend the life anew. I am indebted to my mother for her eternal faith in me and for her abundance of love ever since I remember. I can not forget to thank my siblings (Sachin, Payal and Puja) and my loving in-law's parents for their heartfelt wishes and support at all times. My amazing and venturous sister, Payal always encouraged to bring out the best in me. I am proud to name my beloved husband, Gaurav to always realise invincibility which enabled me to pass through the difficult time of life ever since we know each other. I have scarcely enough words to thank him.

And finally, last but by no means least, many many thanks to all the academic and non-academic staff at HRI who provided a comfy and homely environment that I will always miss. Special thanks to the Registrar, Ravindra Singh and his administration team including Amit roy, Archana Tondon, Yashpal Singh, Archana Singh, Rachna Parik, Shweta Sriwastava, Rajeev Kumar, Sanjay Verma, Seema Agarwal and Sapna for their support from the first day at HRI!

Contents

SYNOPSIS

Introduction -

Two dimensional Dirac materials are the most widely studied materials in the condensed matter community since Andre Geim and Kostya Novoselov were awarded the Nobel Prize in Physics in 2010 for their breakthrough discovery of graphene. The reason for their significance in condensed matter research lies in their electronic band structure which shows a Dirac-like dispersion *i.e.* the low energy excitations inside these materials behave like relativistic particles [1]. Graphene, a well-known Dirac material is a one atomic thick layer of sp^2 bonded carbon atoms structured in the form of a honeycomb lattice. The Dirac-like spectrum in graphene is stable against electron-electron interactions, disorder and the presence of non-magnetic impurities due to the combination of two underlying lattice symmetries: inversion symmetry and time-reversal symmetry. Graphene is thus, a zero gap semiconductor with excellent electronic properties which makes it an extremely promising material for future electronic devices [2]. However, graphene is gapless. Also, its band gap cannot be tuned. This is a hurdle in device fabrications using this material [4]. There have been several theoretical studies regarding the possibility of opening of a gap in the graphene band structure. Some of them also have been experimentally verified. One possibility is the epitaxial growth of graphene on a substrate [5] which breaks the inversion symmetry but preserves the time-reversal symmetry of the lattice structure. It is like providing different on-site energies for the atoms on the A and B sub lattices. A vertically applied electric field has also been demonstrated to be effective in opening an electronic band gap in bilayer graphene [6]. Yet another possibility of inducing the gap is by the time-reversal breaking of the lattice structure, proposed by Haldane in 1988 [7].

Dirac materials with spin-orbit coupling -

There exists another class of materials *e.g.* silicene, germanene, stanene, etc.[8] belonging to the graphene family which are not completely planar due to the large atomic radii of their atoms which gives rise to the buckled structure of their lattices. This feature of such lattices makes a crucial difference in the electronic properties of the charge carriers. Firstly, they can be shown to possess a significant amount of spin-orbit coupling as compared to graphene. Spin-orbit couplings provide a spin-dependent hopping to the charge carriers which cause the quantum spin Hall effect initially proposed by Kane and Mele in graphene. However, it is easier to observe in these materials like silicene, germanene etc. [9]. Second, due to their buckled structure, a staggered potential term is present in their tight binding Hamiltonian which is positive for the A sublattice and negative for the B sublattice. Both the staggering potential and the spin-orbit coupling give rise to a band gap in the electronic band structure which can be tuned by an external electric field applied perpendicular to the sample. The finite band gap and its external tunability are crucial and important differences between graphene and buckled spin-orbit coupled Dirac materials. Device fabrication in the electronics industry is likely to find spin-orbit coupled materials more useful. Also, the spin-orbit coupling turns out to be an effective tool to manipulate electronic states without the application of an external magnetic field [10].

Periodically driven systems -

In recent times, research in the field of periodically driven systems have become very exciting due to the possibility of efficiently tuning topological states of matter [11]. The possibility of realizing a proposed theoretical model in well-controlled experimental cold atomic setup and optical lattices have also provided additional impetus [12]. Time-periodic Hamiltonian can be studied within the Floquet formalism which provides a set of states, called the Floquet states which are not eigenstates of the original Hamiltonian but are the state vectors of the time evolution operator over one period. The corresponding energies of Floquet states are called the quasienergies which are periodic in nature. These are uniquely defined in the first Floquet Brillouin zone (FBZ) extending from $-\hbar\omega/2$ to $\hbar\omega/2$, where ω is the frequency of the external drive. Periodically driven systems can be studied in two limits: $\omega >$ band width of the system, called the high frequency limit and $\omega <$ band width of the system, called the low frequency limit. Both limits have their own advantages and disadvantages for experimental realizations. Such systems have opened up a new class of topological materials which cannot be characterized just by the Chern number which has been utilized to characterize non-driven or static systems. There exists another invariant, called the winding number, calculated from the eigenstates of the time evolution operator of the Floquet Hamiltonian which has been shown to characterize periodically driven systems [13].

Summary of the research work -

The thesis firstly contains the study of transport in a Ferromagnetic-Normal-Ferromagnetic (FNF) junction of silicene, a 2D Dirac material with a significant amount of spin-orbit coupling. We included the staggered potential term which acts oppositely for the A and B sub lattices and acts as an external tunable parameter which provides an external control over the transport quantities of practical importance. We studied spin and valley polarized conductances and tunneling magneto resistance (TMR) in the FNF setup.

The second focus of the thesis is on time-dependent systems which are driven by external circularly polarised electromagnetic radiation. Due to the non-adiabatic evolution, the system does not necessarily remain in the ground state of the initial Hamiltonian. It turns out that this way of driving the system induces topological structure in the bulk spectrum. These periodically driven systems can be studied using the Floquet formalism. People [11] have extensively studied graphene under the application of light and have shown that it opens a gap in the Dirac spectrum which can also be tuned by the light parameters. Moreover, the Gedik group from MIT [14] reported the emergence of Floquet-Bloch states on the surface of a 3D topological insulator Bi_2Se_3.

In this thesis, we explore the Dirac Hamiltonian including both the intrinsic spin-orbit coupling and the staggered potential term in the tight binding Hamiltonian framework. We use the Brillouin-Wigner perturbation theory to study the system in the high-frequency limit of the external drive. In this limit, the system is not allowed to make real transitions and one can incorporate the effect of light through virtual processes. It turns out that this gives rise

to an effective Hamiltonian with additional terms in the Hamiltonian, besides renormalizing the original terms. It also gives rise to higher range hopping terms in the original Hamiltonian. The band gap of the effective time-independent system can be externally tuned by the frequency of the light, the amplitude of the light and the external electric field. We show that the system exhibits various topological phase transitions as we vary the various parameters of the model. We provide the phase diagrams where we demonstrate the bulk invariant as we vary the drive frequency ω, the amplitude of the drive and the external electric field.

In this thesis, we also investigate the low-frequency limit where the bandwidth of the system is higher than the frequency of the drive. This limit is far more interesting as this may not have any non-driven analog. Once again, we compute the phase diagram in this limit and show that the system exhibits many more topological phase transitions due to the mixing of the Floquet bands. This gives rise to another band gap in the spectrum at the Floquet zone boundary other than the band gap near the zero quasienergy. Also, we computed the edge state spectrum for each individual topological phases and verified that the system does not follow the usual bulk-edge correspondence of static systems where the Chern number, which is a bulk invariant, is equal to the number of edge states in the system when computed in a finite geometry. Rather, it is another invariant which gives the number of the edge states in the two non-equivalent gaps in the Floquet systems. The difference between two invariants corresponding to the two non-equivalent gaps has been shown to be equal to the Chern number of the band [13].

The thesis has four chapters and we summarise the thesis in the fifth chapter. The content of each chapter is briefly described below -

- The first chapter provides a detailed analysis of Dirac materials which includes the study of the tight-binding structure of the honeycomb lattice, consequences of inversion and time-reversal symmetries, buckled Dirac materials *e.g.* silicene, germanene, stanene etc. We also provide the details of the edge state spectrum computation for a nanoribbon geometry.

- The second chapter contains the detailed calculation of transport studies in the FNF geometry together with the Landauer-Buttiker formalism.

- We try to explain the Floquet formalism in the third chapter in detail. Here, we focus on the Brillouin-Wigner perturbation theory to study the high-frequency limit of periodically driven Dirac systems with spin-orbit coupling. We discuss the numerical results and summarize this part.

- Chapter four contains the study of the low-frequency limit of the model. Here, we give a detailed analysis of each of the phases by computing the spin-resolved Chern numbers and finally, the bulk-boundary correspondence of periodically driven systems. We also discuss the method of computing the real space Chern number which is required to study the topological structure in the absence of translational symmetry.

List of Figures

Chapter 1

Introduction

1.1 Dirac materials: Graphene

Graphene is a single layer of graphite which is made up of hexagonal rings of carbon, giving rise to a honeycomb-like lattice structure. This is the lightest [18], strongest [19], thinnest, best conductor of heat at room temperature [20, 21], very high electron mobility conductor [22] ever discovered.

The honeycomb lattice of Graphene is made up of two inequivalent lattice sites A and B (Fig: 1.1, where black and green colour dots represent A and B sublattice points) and hence the unit cell of graphene contains two atoms [23].

The lattice vectors are given by -

$$A_1 = a_0\left(\frac{\sqrt{3}}{2}, \frac{3}{2}\right) \quad \text{and} \quad A_2 = a_0\left(\frac{-\sqrt{3}}{2}, \frac{3}{2}\right) \tag{1.1}$$

where, $a_0 = 1.42\mathring{}\text{Å}$ is the lattice constant. The reciprocal lattice vectors are given by -

$$B_1 = \frac{2\pi}{\sqrt{3}\,a_0}\left(1, \frac{1}{\sqrt{3}}\right), \qquad \text{and} \qquad B_2 = \frac{2\pi}{\sqrt{3}\,a_0}\left(1, \frac{-1}{\sqrt{3}}\right). \tag{1.2}$$

The nearest neighbour vectors are given by -

$$\delta_1 = a_0\,(0, -1)\,, \quad \delta_2 = a_0\left(\frac{\sqrt{3}}{2}, \frac{1}{2}\right), \quad \delta_3 = a_0\left(\frac{-\sqrt{3}}{2}, \frac{1}{2}\right) \tag{1.3}$$

The six next nearest neighbours are same for A and B sub lattice and are placed at -

$$a_{1,2} = \pm A_1,\ a_{3,4} = \pm A_2,\ a_{5,6} = \pm(A_1 - A_2) \tag{1.4}$$

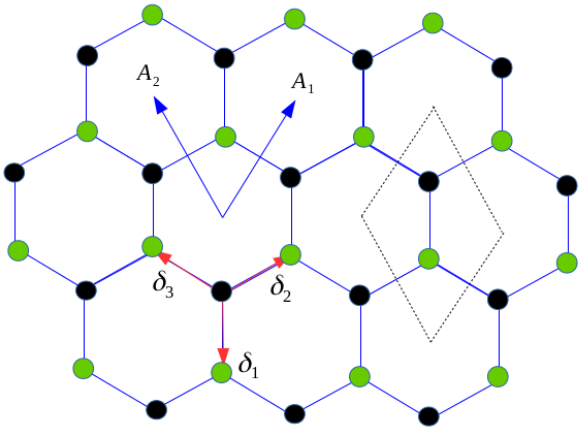

Figure 1.1: Graphene: two dimensional honeycomb lattice structure

We can write down the tight-binding Hamiltonian for the π orbital electrons of Graphene -

$$H = -t \sum_{\langle i,j \rangle} c_i^\dagger c_j + h.c. \tag{1.5}$$

where, t = 2.8 eV (in units of energy) is the nearest neighbour hopping amplitude in graphene. The energy dispersion derived from this Hamiltonian is -

$$E_k = \pm t \sqrt{3 + f(k)} \tag{1.6}$$

where,

$$f(k) = 2\cos(\sqrt{3}k_y a_0) + 4\cos\left(\frac{\sqrt{3}}{2}k_y a_0\right)\cos\left(\frac{3}{2}k_x a_o\right) \tag{1.7}$$

The low energy behavior of graphene is governed by the Dirac electrons which have the linear dispersion at the two valleys K and K'.

1.2 Spin-orbit coupling (SOC) in Dirac materials: Silicene, Germanene, Stanene

Control over the spin degrees of freedom has been the ultimate goal in spintronics. Extensive studies have been conducted in 2D electron gases such as GaAs/$Ga_{1-x}Al_xAs$ [24] and HgTe/CdTe/HgTe quantum wells [25]. More interesting phenomena are expected in low dimensional systems with sufficiently strong SOC.

There exist a class of Dirac materials which are similar to the Graphene, but in contrast to the planar lattice, these materials are buckled and the two triangular sublattices are separated

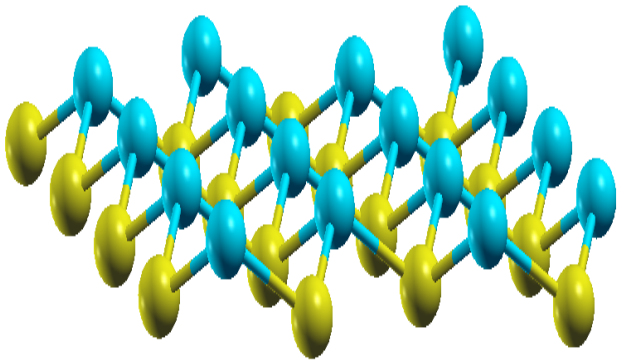

Figure 1.2: Buckled Dirac Materials *e.g.* Silicene, Germanene, Stanene

by a vertical distance $2l$ (Fig: 1.2) and have larger spin-orbit coupling than graphene e.g. silicene has spin-orbit coupling hundred times larger than graphene.

The tight binding Hamiltonian for the buckled Dirac materials including all possible terms [26] -

$$\begin{aligned} H &= -t \sum_{\langle i,j\rangle,\alpha\beta} c^{\dagger}_{i\alpha} c_{j\alpha} + l\, E_z \sum_{i,\alpha} \xi_i\; c^{\dagger}_{i\alpha} c_{j\alpha} - \mu \sum_{i,\alpha} c^{\dagger}_{i\alpha} c_{i\alpha} + \frac{i\lambda}{3\sqrt{3}} \sum_{\langle\langle i,j\rangle\rangle,\alpha,\beta} \nu_{i,j}\; c^{\dagger}_{i\alpha}\, \sigma^{z}_{\alpha\beta}\, c_{j\beta} \\ &\quad + i\,\lambda_{R_1} \sum_{\langle i,j\rangle} c^{\dagger}_{i\alpha} \left(\vec{\sigma} \times \vec{d}_{ij}\right)^{z}_{\alpha\beta} c_{j\beta} - i\,\lambda_{R_2} \sum_{\langle\langle i,j\rangle\rangle,\alpha\beta} \xi_i\; c^{\dagger}_{i\alpha} \left(\sigma \times \hat{d}_{ij}\right)^{z}_{\alpha\beta} c_{j\beta}. \end{aligned} \tag{1.8}$$

We explain each term: the first term represents the nearest neighbour hopping term with t=1.6 eV. The second term is the staggered potential term which is due to the buckled structure of the lattice. The third term is the chemical potential term. The atomic spin-orbit coupling term is given by the fourth term with λ=3.9 eV while the last two are the extrinsic and intrinsic Rashbha spin-orbit coupling respectively. We note the following properties of intrinsic and extrinsic Rashbha spin-orbit couplings present in spin-orbit coupled Dirac materials [27] -

1. The intrinsic Rashbha SO-coupling is zero at the Dirac point K but it has a nonzero value when $\vec{k}$ deviates from K point. Moreover, when the structure returns to the planar structure ($\theta = 90^0$), the intrinsic Rashbha SO-coupling vanishes even when $\vec{k}$ deviates from K. Therefore the intrinsic Rashbha is entirely caused by the buckled geometry.

2. The intrinsic Rashba SOC is quite different from the extrinsic Rashba SOC, which arises from a perpendicular electric field or interaction with a substrate leading to breaking of mirror symmetry in some direction, and thus has finite magnitude at the Dirac point K.

3. The extrinsic Rashbha SO-coupling due to perpendicular electric field may be written as-

$$\lambda_{R_1} = \frac{E_z\, \xi_0\, e\, z_0}{3\, V_{sp\alpha}} \tag{1.9}$$

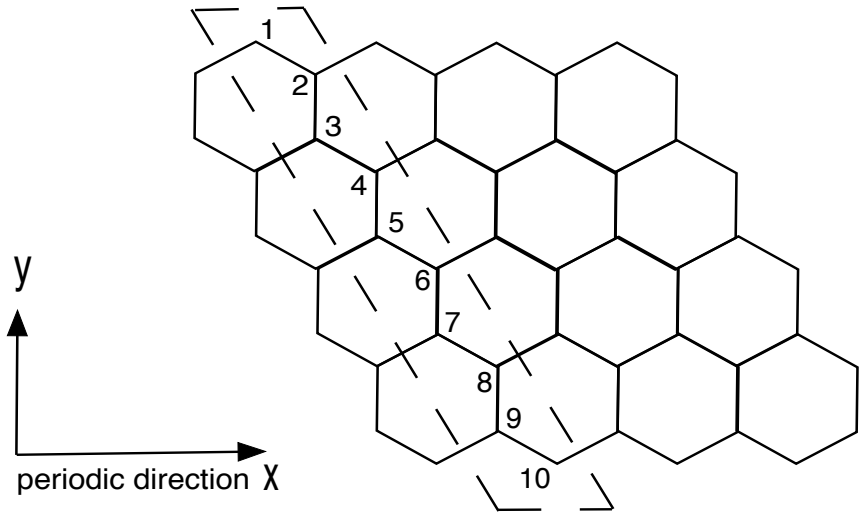

Figure 1.3: Graphene nano ribbon with periodic boundary condition in x-direction and open boundary condition in y-direction.

where, z_0 is proportional to the atomic size of silicon. Its magnitude is about 0.2 meV if we assume a typical electric field $E_z \sim \frac{50V}{300nm}$ and use the value $z_0 \sim 4.5a_B$

4. The extrinsic Rashbha for silicene, $\lambda_{R_1} \propto E_z$, and becomes of the order of 10 μeV at $E_z = \frac{\lambda_{SO}}{l} = 17\,\text{meV}A^{-1}$.

5. For silicene, the atomic SO = 3.9 meV, extrinsic Rashbha = 0.2 meV and the intrinsic Rashbha = 0.7 meV.

We give a detail study of each SO-coupling term in momentum space in Appendix A.

1.3 Edge state computation for nano ribbon geometry

Here, we wish to give the details of a computation to get the edge state spectrum of a zigzag nanoribbon which is assumed to be finite in the y-direction while periodic in the x-direction.

We consider a graphene nanoribbon as in Fig:(6.1). To illustrate the procedure we take the unit cell (dashed line) which has ten lattice points along the y-direction. Since it has periodicity in the x-direction, momentum in this direction is a good quantum number. The number of lattice points along y-direction forms the basis to write down the Hamiltonian matrix. The tight binding Hamiltonian for graphene is given by eq.(1.5) and we write down the Hamiltonian matrix for graphene ribbon below -

$$
\begin{array}{c}
\\
1 \\
2 \\
3 \\
4 \\
5 \\
6 \\
7 \\
8 \\
9 \\
10
\end{array}
\begin{array}{c}
\begin{array}{cccccccccc}
1 & 2 & 3 & 4 & 5 & 6 & 7 & 8 & 9 & 10
\end{array} \\
\left(\begin{array}{cccccccccc}
0 & \alpha & 0 & 0 & 0 & 0 & 0 & 0 & 0 & 0 \\
\alpha^* & 0 & \beta & 0 & 0 & 0 & 0 & 0 & 0 & 0 \\
0 & \beta^* & 0 & \alpha & 0 & 0 & 0 & 0 & 0 & 0 \\
0 & 0 & \alpha^* & 0 & \beta & 0 & 0 & 0 & 0 & 0 \\
0 & 0 & 0 & \beta^* & 0 & \alpha & 0 & 0 & 0 & 0 \\
0 & 0 & 0 & 0 & \alpha^* & 0 & \beta & 0 & 0 & 0 \\
0 & 0 & 0 & 0 & 0 & \beta^* & 0 & \alpha & 0 & 0 \\
0 & 0 & 0 & 0 & 0 & 0 & \alpha^* & 0 & \beta & 0 \\
0 & 0 & 0 & 0 & 0 & 0 & 0 & \beta^* & 0 & \alpha \\
0 & 0 & 0 & 0 & 0 & 0 & 0 & 0 & \alpha^* & 0
\end{array}\right)
\end{array}
$$

where,

$$\alpha = e^{i(k_x\sqrt{3}/2 - k_y/2)} \quad \text{and} \quad \beta = e^{-ik_y}$$

We diagonalise this Hamiltonian and plot the eigenvalues with respect to the momentum in x-direction k_x. If we take even number of sites along y-axis we get the edge spectrum as represented in Fig:(1.4).

The edge spectrum changes if we had odd number of sites along y-direction. In this case, there are dangling bonds on one side of the ribbon which are not zigzag type like the other side of the nano ribbon [29] and hence, there is only one edge mode exactly at zero energy as shown in Fig:(1.5).

We use this method of edge state computation to analyze the bulk-boundary correspondence in Floquet topological insulators [28]. We incorporate the effect of light by the Peierl's substitution in the hopping amplitudes which would change the form of matrix elements of the Hamiltonian discussed above.

1.4 Driven quantum systems

The topological state of quantum matter is known to possess edge states which are robust against disorder as long as the bulk band gap is not closed. These edge states could be potentially useful for applications. However, topological systems are hard to find and so it is interesting to see whether non-trivial topology can be induced in materials by external driving.

Recently, it has been realised that periodic driving can be used as a tool to manipulate the bulk band structure and that it can induce topological structure in trivial insulators. Such insulators are called the Floquet topological insulators. These induced topological phases also possess gapless edge states like topological insulators. But, unlike topological insulators, these driven topological phases can exhibit anomalous topological phases which are not possible in non-driven systems [30, 31]. Moreover, Floquet topological phases have been experimentally discovered in solid state [14],

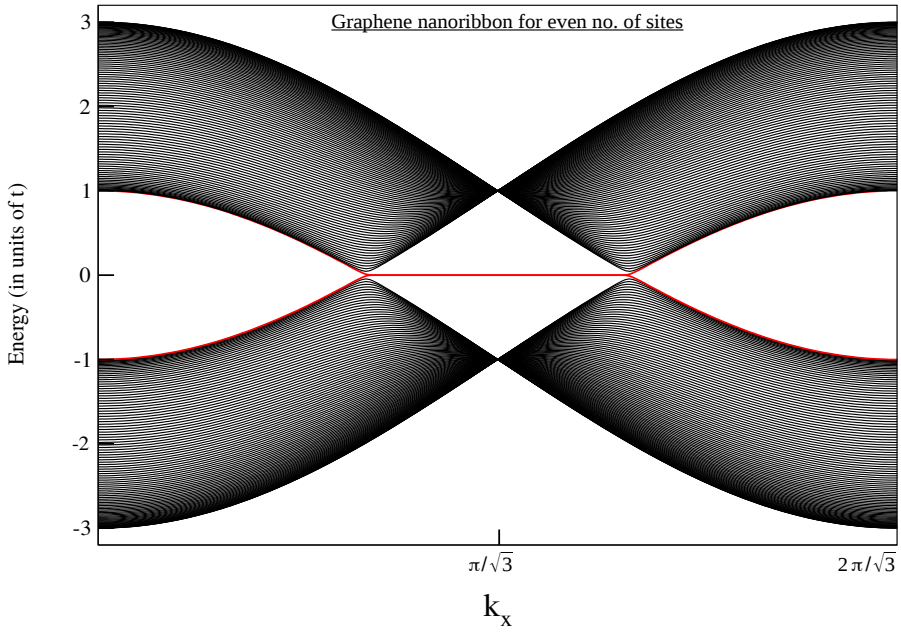

Figure 1.4: Edge states in graphene zigzag nano ribbon for even number of lattice points along y-axes

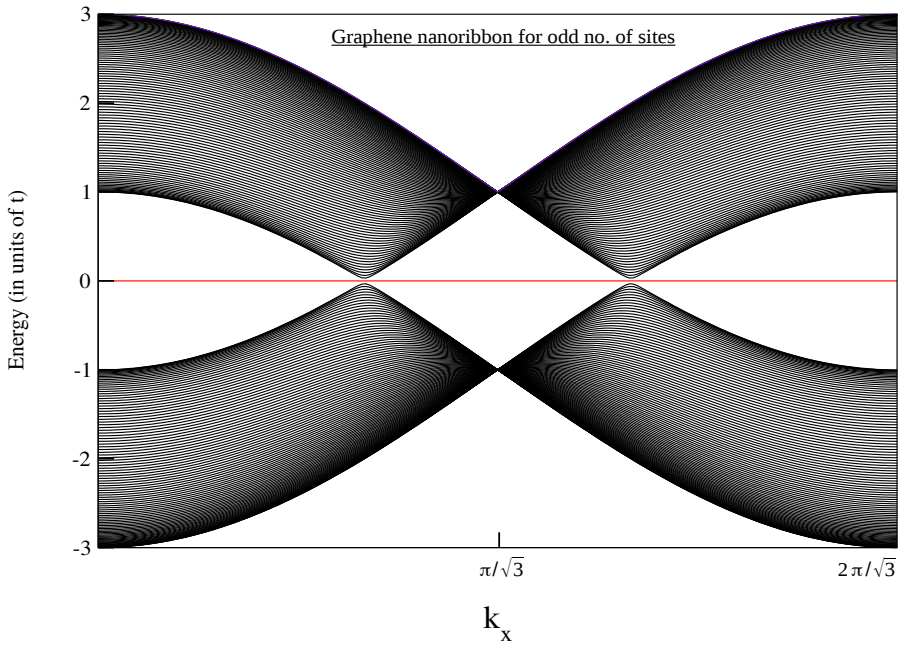

Figure 1.5: Edge states in graphene zigzag nano ribbon for odd number of lattice points along y-axes

optical [32] and cold-atom systems [33].The concept of Floquet engineering has been employed very successfully in various experiments with ultracold atoms in driven optical lattices. This includes dynamic localisation [34], photon-assisted tunnelling [35], the control of the boson superfluid-to-Mott-insulator transition [36], resonant coupling of Bloch bands [37], the dynamic creation of kinetic frustration [38], as well as the realisation of artificial magnetic fields and topological band structures [39, 40]. In quantum gas without a lattice, periodic driving has recently also been employed to tune or induce spin-orbit coupling [41, 42].

In the following section, we review the Floquet formalism to deal with periodically driven systems. Using this formalism and comparing the frequency of the drive ω with the bandwidth of the material, it is possible to derive an effective static Hamiltonian when the frequency is much larger than the bandwidth. There are various perturbative schemes *e.g.* Floquet Magnus expansion [43, 44, 45, 46], Brillouin-Wigner perturbation theory [47] and van Vleck degenerate perturbation theory [48, 49] to get the effective time-independent Hamiltonian in inverse frequency expansion. The B-W perturbation theory has been described in Ref. [47] to obtain the high-frequency effective Hamiltonian for periodically driven systems. In comparison with other similar high-frequency expansions, the B-W expansion has far fewer terms at higher orders. Moreover, the B-W theory has a simple recursive technique to compute higher order terms which is often less cumbersome than the other expansions. We give a detailed study of irradiated spin-orbit coupled materials using the B-W perturbation theory in next chapter. However, the perturbation theory breaks down as the frequency of the drive becomes equal to the bandwidth of the system. This limit corresponds to the low-frequency limit and is discussed at length in the last chapter.

1.4.1 Time-evolution of periodically driven systems

The time-evolution of any quantum state is governed by the Schrödinger equation [50, 51] -

$$i\,\partial_t\,\psi(t) \;=\; H(t)\,\psi(t) \tag{1.10}$$

where, H(t) is the Hamiltonian of the system. If the Hamiltonian is time-independent then we can diagonalise the Hamiltonian to get the complete set of solutions $\{E_n, \Psi_n\}$ of the following Schrödinger equation -

$$H\Psi_n \;=\; E_n\Psi_n \tag{1.11}$$

and this will allow to compute the time-evolution of any state as -

$$\psi(t) \;=\; \sum_n c_n\,\Psi_n\,e^{-iE_nt} \tag{1.12}$$

where, the amplitudes $\{c_n\}$ are constant in time and can be calculated from the initial conditions: $c_n = \langle\psi(0)|\Psi_n\rangle$.

Now, if we have a time-dependent system then one cannot diagonalise the Hamiltonian to get the eigenstates $\{\Psi_n\}$ as the system is changing its state at each instant of time. It simply means that the system does not possess a ground state. But, we can integrate the Schrödinger equation to obtain -

$$\psi(t) \;=\; U(t)\,\psi(0) \tag{1.13}$$

where, the time-evolution operator is given by -

$$U(t) \;=\; \mathcal{T}e^{-i\int_0^t H(t')\,dt'} \tag{1.14}$$

Here, $\mathcal{T}$ is the time-ordering operator. The time-evolution operator is an unitary operator as follows from eq.1.13 *i.e.* U(0)=1. However, we have not achieved much to get an understanding of the behavior of the system as eq.(1.13) is just the restatement of the problem itself. But for time-periodic Hamiltonians *i.e.* H(t+T) = H (t), discrete time-translational symmetry allows the following condition -

$$U(mT,0) \;=\; U(T,0)^m \tag{1.15}$$

We explicitly show how this follows from the periodicity of the Hamiltonian -

$$\begin{aligned} U(mT,0) &= \mathcal{T} e^{-i\int_0^{mt} H(t)\,dt} \\ &= \mathcal{T} e^{-i\sum_{k=1}^{m}\int_{(k-1)T}^{kT} H(t)\,dt} \end{aligned} \tag{1.16}$$

which simplifies to (using H(t+T)=H(t)) -

$$\begin{aligned} U(mT,0) &= \mathcal{T} e^{-i\sum_{k=1}^{m}\int_0^{T} H(t)\,dt} \\ &= \mathcal{T}\prod_{k=1}^{m} e^{-i\int_0^T H(t)dt} \end{aligned} \tag{1.17}$$

Because the terms over a full period are equal, they commute. Hence, one can write -

$$U(mT,0) \;=\; \prod_{0}^{T} \mathcal{T} e^{-i\int_0^T H(t)dt} \tag{1.18}$$

$$\;=\; [U(T,0)]^m \tag{1.19}$$

Thus, the eigenstates of U(T) have evolved into themselves in each driving period gaining a complex phase and the eigenvalue problem for periodically driven systems takes the form -

$$U(T)\,\Psi_n \;=\; e^{-i\epsilon_n T}\,\Psi_n \tag{1.20}$$

Now, we can write down the time-evolution of any initial state using the eigenvalues and eigenstates of the Floquet operator as -

$$\psi(mT) \;=\; \sum_n c_n \Psi_n\, e^{-i\,\epsilon_n\, mT} \tag{1.21}$$

where, $\{c_n\}$ are determined by the initial state: $c_n = \langle\psi(0)|\Psi_n\rangle$. The importance of the time-periodic Hamiltonian lies in the fact that the knowledge of the propagator, the time evolution operator over a period T provides all the information needed to study the long-time dynamics of periodically driven quantum systems.

1.4.2 Time-independent Effective Hamiltonian

We consider an evolution operator for the time-periodic Hamiltonian over a period T as [52]-

$$U(T) \;=\; \mathcal{T} e^{-i\int_0^T H(t)dt} \tag{1.22}$$

Since U(T) is an unitary operator we can write it as -

$$U(T) \simeq e^{-iH_{eff}T} \tag{1.23}$$

One can write the Fourier components of the time-periodic Hamiltonian -

$$H(t) = \sum_{n=-\infty}^{\infty} H_n\, e^{in\omega t} \simeq H_0 + H_1 e^{i\omega t} + H_{-1} e^{-i\omega t} \tag{1.24}$$

Here, we have considered the first Harmonic contribution. Expanding the exponential in eq.(1.22) in Taylor series -

$$U(T) = \mathcal{T} e^{-i\int_0^T H(t)dt} \simeq \mathcal{T}\left\{1 - i\int_0^T H(t)dt + \frac{-i^2}{2}\int_0^T H(t_1)dt_1 \int_0^T H(t_2)dt_2 + ...\right\} \tag{1.25}$$

$$= 1 - i\int_0^T H(t)dt - \frac{1}{2}\left[\int_0^T dt_1 \int_0^{t_1} dt_2 H(t_1)H(t_2) + \int_0^T dt_2 \int_0^{t_2} dt_1 H(t_2)H(t_1)\right] \tag{1.26}$$

We have used the time-ordering operator in the last line. Now, we put the form of H(t) from eq.(1.24) and perform the integrals to get the effective evolution operator -

$$U(T) \simeq 1 - iH_0T - \frac{T}{\omega}\left\{\pi H_0^2 - i\left([H_0, H_{-1}] - [H_0, H_!] + [H_{-1}, H_1]\right)\right\} \tag{1.27}$$

$$\simeq 1 - iH_{eff}T - \frac{1}{2}H_{eff}^2 T^2 + ... \tag{1.28}$$

$\Rightarrow$

$$H_{eff} = H_0 - \frac{1}{\omega}\left([H_0, H_{-1}] - [H_0, H_1] + [H_{-1}, H_1]\right) \tag{1.29}$$

The same equation can be derived by using the Magnus expansion. Other perturbative methods as discussed at the beginning of this section can also be employed to arrive at similar effective time-independent Hamiltonians which is an essential prerequisite for Floquet engineering. These effective Hamiltonians would also be perturbative series in terms of $\frac{1}{\omega}$. The actual dynamics will then follow the dynamics $U_{eff}(t) = e^{-iH_{eff}t}$ induced by the effective Hamiltonian only stroboscopically, but in the regime of fast driving, where ω exceeds the relevant scales of H(t), the effective dynamics is a good approximation also for $t \neq nT$ [53].

Chapter 2

Transport through Ferromagnet-Normal-Ferromagnet junction

The honeycomb lattice structure of graphene causes the Dirac-like dispersion as well as the chirality to its charged particles. These characteristics led to the intensive study of the transport properties of this material. Also, a detailed study of the transport phenomenon of graphene junctions is essential for its potential application in electronics and spintronics. There have been numerous theoretical as well as experimental studies on transport in graphene junctions with other materials like superconductors, ferromagnets, normal metals etc [54, 55, 56, 57, 58, 59, 60, 61, 62]. It has also been predicted that spin transport controlled by a gate electrode is possible in a ferromagnet deposited graphene [58, 60, 61]. Moreover, a single layer of graphene has been shown to exhibit a quantum spin Hall effect due to the presence of spin-orbit interaction and further suggested this phenomenon to be prominent and easily observed in materials with strong spin-orbit interaction [63]. We intend to focus on Dirac materials with large spin-orbit coupling to study the transport in the junction of ferromagnet-normal-ferromagnet, made up of silicene. Silicene has a honeycomb lattice structure with thousand times larger spin-orbit coupling than graphene due to large radii of its constituent atoms. The large radius of atoms give rise to lattice distortion and eventually causes the buckling to its lattice structure. Due to buckling, the charge carriers on two sublattices would feel opposite potential when placed in an external electric field. This feature provides a handle to control the electronic properties by an external electric field. It has been shown that at the critical electric field, K-valley (K') is $\uparrow$-spin ($\downarrow$-spin) polarised. The possibility of using silicene as a spintronic device has also been reported very recently [64, 65, 66, 67]. We analysed charge conductance and spin and valley polarisation along with the tunneling magnetoresistance (TMR) in FNF junction below. TMR is an important quantity in spintronics which occurs at junctions between materials, i.e., ferromagnetic-Normal-ferromagnetic junction. The resistance of the junction is different for parallel and antiparallel spin configurations, and this difference in resistance can be experimentally measured.

2.1 The setup

We wish to study the FNF junction in silicene as shown in Fig.(2.1). Ferromagnetism is induced in silicene by the proximity effect when it is placed in proximity with a magnetic insulator, which we

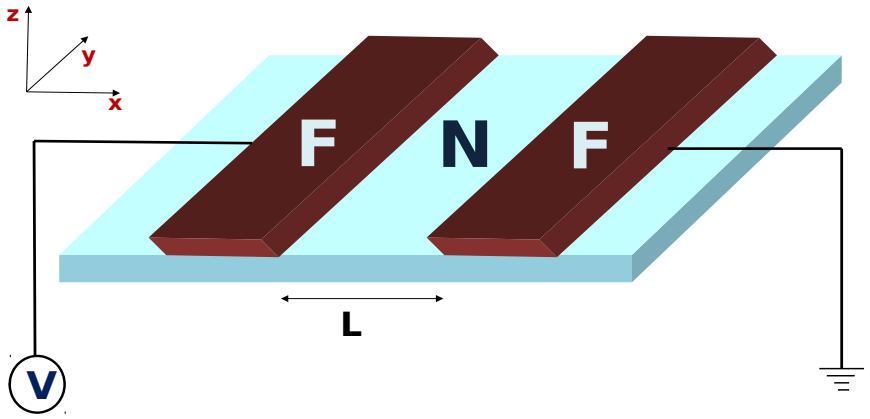

Figure 2.1: Schematic of the FNF junction in silicene in which two ferromagnetic patches (dark brown, dark grey) have been deposited on two sides of a normal silicene sheet (cyan, light grey) to induce ferromagnetism in it. Here L is the length of the normal silicene region.

model by the following Hamiltonian given by [68]

$$H = \hbar v_F(\eta k_x \hat{\tau}_x - k_y \hat{\tau}_y) + (elE_z - \eta\sigma\lambda_{SO})\hat{\tau}_z + V(x) - h(x), \tag{2.1}$$

where v_F is the Fermi velocity of the charge carriers in silicene, e is the charge of the electron and η, σ correspond to the valley and spin indices and $\hat{\tau}$ corresponds to the sublattice (pseudospin) Pauli matrices. λ_{SO} is the parameter that specifies the spin-orbit coupling in silicene. Due to the buckled structure of silicene, the atoms in the two sublattices respond differently to an externally applied electric field E_z [69]. Thus lE_z is the potential difference between the two sublattices A and B due to this applied electric field where l is the separation between the two sublattices. Hence, the potential difference is a tunable parameter and can be tuned by an external electric field [69]. Also, when the Fermi energy is close to the Dirac point, at the critical electric field $E_z^c = \eta\sigma\lambda_{SO}$, one of the valleys in silicene is up-spin polarized and the other one is down-spin polarised [69]. Here $\eta = \pm 1$ denotes the $\mathbf{K}$ and $\mathbf{K}'$ valleys respectively and $\sigma = \pm 1$ denotes the spin indices. $V(x)$ denotes the profile for the potential barrier in the normal silicene region and $h(x)$ corresponds to the exchange splitting or the energy difference between the up and down spin electrons in the Ferromagnetic Silicene regions. Note, however, that in real materials the proximity of a ferromagnet to silicence can actually change the band structure of silicene itself. In that case, the only way to proceed will be to perform first-principles calculations as has been done in graphene [70].

We now consider the geometry shown in Fig. 2.1 and assume that the system is translationally invariant along the y direction. The interfaces between the normal and the FS are located at $x = 0$ and $x = L$ where L the length of the normal silicene region sandwiched between the ferromagnetic patches. Here $V(x) = U\Theta(x)\Theta(L - x)$ is the profile of the potential barrier modelled in the normal silicene region and $h(x) = h[\sigma s\Theta(-x) + \sigma' s'\Theta(x - L)]$ denotes the exchange field or Zeeman field in the two ferromagnetic regions with $s = s'$ corresponding to the parallel (P) configuration and $s = -s'$ corresponding to the antiparallel (AP) spin configurations of magnetization respectively. We show

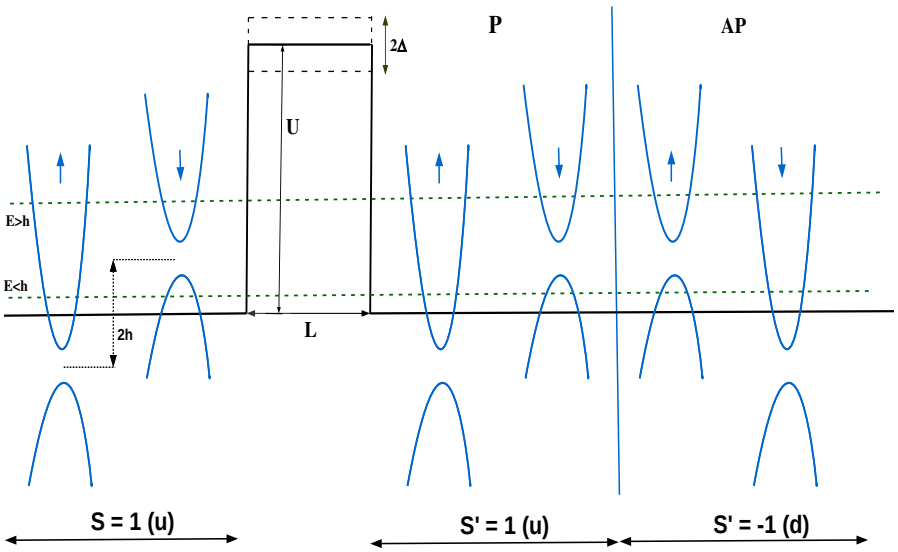

Figure 2.2: Schematic of the configurations with P (uu) and AP (ud) spin polarizations for one of the valleys of the FNF silicene junction.

the schematic of up and down spin in left region (for $s = 1$) and in right region for parallel ($s' = 1$ or P or uu) and antiparallel ($s' = -1$ or AP or ud) configurations in FNF junction for both $E < h$ and $E > h$ regions in Fig. 2.2. The orientation of the exchange field in the left region is kept fixed by keeping $s = 1$ and then $s' = 1$ and $s' = -1$ in the right region corresponds to the parallel (P or uu) and antiparallel (AP or ud) configuration respectively. Note that the $E < h$ line crosses the same band in the third region for the P configuration, but crosses the other band for the AP configuration. As reported earlier [71], this feature gives rise to negative TMR in graphene. In silicene, also, the same feature is responsible for negative TMR which we discuss later in next section.

2.2 The band structure analysis

In Fig.(2.3) we demonstrate the spin polarization of both the $\mathbf{K}$ and $\mathbf{K}'$ valleys for FS with the magnetisation directions up (u defined by $s = +1$) and down (d defined by $s = -1$) via an energy band diagram. The diagram clearly shows that different spin orientations behave differently in the $\mathbf{K}$ and $\mathbf{K}'$ valleys at different values of the exchange field h. To further explain, we fix $\lambda_{SO}/h = 0.5$ and show the dispersion for $\mathbf{K}\uparrow$, $\mathbf{K}\downarrow$, $\mathbf{K}'\uparrow$ and $\mathbf{K}'\downarrow$ for four different values (represented by red, green, blue and magenta for $E_z/\mathrm{h} = 0.1, 0.5, 1.0, 2.0$ respectively) of the tunable parameter E_z/h, for the cases u and d. Note that we use $\uparrow, \downarrow$ to denote the spins of the incoming (also reflected and transmitted) charge carriers and we use u, d to denote the orientation of magnetic exchange. For the u or $s = +1$ case, at $E_z/h = \lambda_{SO}/h = 0.5$ both $\mathbf{K}\uparrow$ and $\mathbf{K}'\downarrow$ have a vanishing band gap. On the other hand, for $E_z/h = 0.1$, $E_z/h = 1$, and $E_z/h = 2$, the valleys at $\mathbf{K}\uparrow$, $\mathbf{K}\downarrow$, $\mathbf{K}'\uparrow$, $\mathbf{K}'\downarrow$ are all gapped. Also note that due to the exchange splitting h, the $\mathbf{K}'$ valley is shifted upwards for the $\downarrow$ spin while the $\mathbf{K}$ valley is shifted downwards for the $\uparrow$ spin. The case for d or $s = -1$ is the other way around. Hence, it is clear that unlike in graphene, the contributions to the conductances from various spin configurations will not be identical for the $\mathbf{K}$ and $\mathbf{K}'$ valleys.

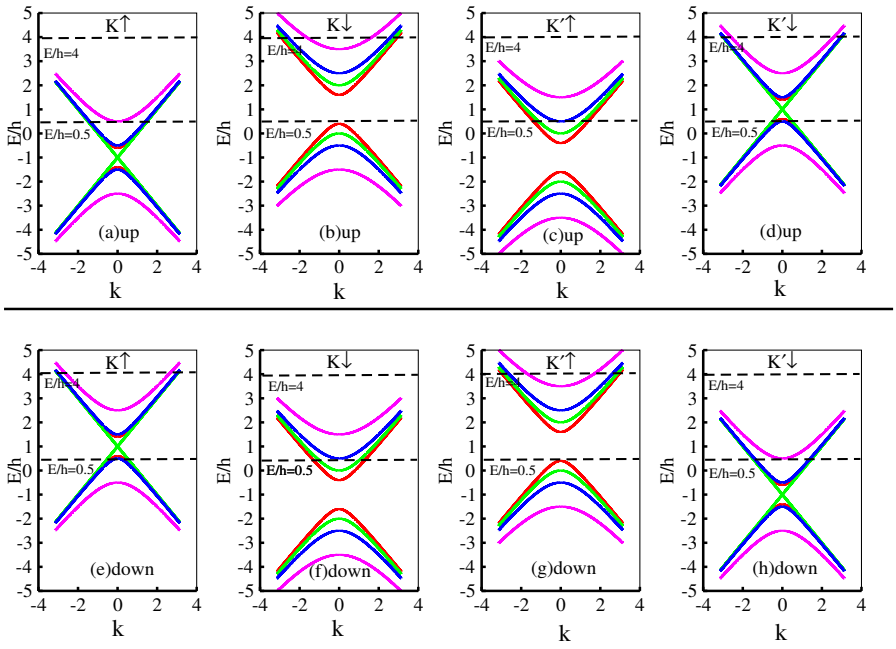

Figure 2.3: (a) to (d) gives the schematic of the band structure for $s = +1$, at $\mathbf{K}$ (for both $\uparrow$ and $\downarrow$ spin) and $\mathbf{K}'$ (for both $\uparrow$ and $\downarrow$ spin) valleys for ferromagnetic silicene for four different values of the dimensionless parameter E_z/h (red (0.1), green (0.5), blue (1.0) and magneta (2.0)). On the other hand (e) to (h) gives the same for $s = -1$. We use these diagrams to qualitatively explain the dependence of conductances on the electric field as mentioned in the text.

2.3 Scattering Matrix Approach

We model our FNF setup within the scattering matrix formalism [72] where we match the wave functions at each ferromagnet−normal interface to obtain the scattering matrix and find the conductances and the TMR . The wave functions for the valley η in each of the three regions, $x < 0$, $0 < x < L$ and $x > L$ can be written as

$$\begin{aligned}\psi_i &= a_i \frac{e^{ik_{ix}x}}{\sqrt{2E\tau_i}} \begin{pmatrix} \eta k_i S_i e^{i\eta\theta_i} \\ \tau_i \end{pmatrix} \\ &+ b_i \frac{e^{-ik_{ix}x}}{\sqrt{2E\tau_i}} \begin{pmatrix} -\eta k_i S_i e^{-i\eta\theta_i} \\ \tau_i \end{pmatrix}, \end{aligned} \tag{2.2}$$

where $a_1 = 1, b_1 = r$ for $x < 0$, $a_2 = a, b_2 = b$ for $0 < x < L$ and $a_3 = t, b_3 = 0$ for $x > L$. Note that we keep track of the sign of the charge carriers by including the index S_i in all the regions (the sign of the charge carriers changes from electron-type to hole-type when S_i is negative in any region). This actually happens for the anti-parallel configuration when energy of the incident charge carrier is below the induced magnetic field energy *i.e.* $(E < h)$. This charge reversal actually qualitatively changes the conductances, as was shown in graphene [71].

We obtain the scattering matrix both for $E > h$ and $E < h$ by matching the wave functions (see Eq.(2.2)) at $x = 0$ and $x = L$ and solving Eq.(2.3) numerically.

$$\begin{bmatrix} \frac{-\eta k_1 S_1 e^{-i\eta\theta_1}}{\sqrt{2E\tau_1}} & -2\eta k_2 S_2 e^{i\eta\theta_2} & \eta k_2 S_2 e^{-i\eta\theta_2} & 0 \\ \sqrt{\frac{\tau_1}{2E}} & -\tau_2 & -\tau_2 & 0 \\ 0 & 2\eta k_2 S_2 e^{i\eta\theta_2} e^{ik_{2x}L} & -2\eta k_2 S_2 e^{-i\eta\theta_2} e^{-ik_{2x}L} & \frac{\eta k_3 S_3 e^{i\eta\theta_3} e^{-ik_{3x}L}}{\sqrt{2E\tau_3}} \\ 0 & \tau_2 e^{ik_{2x}L} & \tau_2 e^{-ik_{2x}L} & -e^{ik_{3x}L}\sqrt{\frac{\tau_3}{2E}} \end{bmatrix} \begin{bmatrix} r \\ a \\ b \\ t \end{bmatrix} = \begin{bmatrix} \frac{-\eta k_1 S_1 e^{i\eta\theta_1}}{\sqrt{2E\tau_1}} \\ -\sqrt{\frac{\tau_1}{2E}} \\ 0 \\ 0 \end{bmatrix} \quad (2.3)$$

Further,

$$\begin{aligned} k_i &= \sqrt{{E_i}^2 - (elE_z - \eta\sigma_i\lambda_{SO})^2} \\ \text{and} \quad \tau_i &= E_i - (elE_z - \eta\sigma_i\lambda_{SO}) \ , \end{aligned} \quad (2.4)$$

with $\sigma_1 = \sigma$, $\sigma_3 = \sigma'$, $E_1 = E + sh$, $E_3 = E + s'h$ and $S_i = sgn[E_i - (elE_z - \eta\sigma_i\lambda_{SO})]$. Since momentum is conserved in the y direction and does not change, it is convenient to write the x-component of the wave-vectors as

$$k_{xi} = \sqrt{{k_i}^2 - {k_y}^2} \ . \quad (2.5)$$

where k_y is the conserved momentum in the y direction.

In Eqs. (2.4 and 2.5) we consider $i = 1, 3$ only. For simplicity we assume that $E_z = 0$ in the middle region which makes the momentum in the middle region independent of valley and spin (σ_2). Hence for the central region,

$$\begin{aligned} k_2 &= \sqrt{E_2^2 - \lambda_{SO}^2} \ , \\ k_{x2} &= \sqrt{k_2^2 - {k_y}^2} \ , \\ \text{and} \quad \tau_2 &= E_2 \ . \end{aligned} \quad (2.6)$$

where $E_2 = E - U$ and U is the height of the potential barrier in the normal silicene region.

2.4 Results

In this section we present our numerical results for the FNF junction for different parameter regimes.

We first study the model described in Eq.(2.1) which has a spin-independent barrier in the normal silicene region. We compute the conductance using the transmission coefficients obtained in Eq.(2.3) for both the parallel ($s = s'$) and the anti-parallel ($s = -s'$) configurations of spins, using the Landauer−Buttiker formalism [72]. We use the scattering matrix to compute the total transmission probability $T^{ss'}(\theta_1) = |t|^2 k_{x3}/k_{x1}$ for parallel and anti-parallel configurations by choosing the spins appropriately and for a particular incident angle θ_1 (which fixes the angles in the other regions as well). The factor of k_{x3}/k_{x1} in the transmission function is needed because the probability flux density includes a factor of the velocity which is essentially $\hbar k/m$. Since experimentally, it is not easy to control the angle of incidence of the impinging electron, we then compute the conductance by integrating over the possible angles of incidence and multiplying by the number of modes within the width W of the silicene sample. At zero temperature, this leads us to a conductance given by

$$G^{ss'} = \frac{e^2}{h}\frac{Wk_1}{\pi}\int_0^{\theta_C} T^{ss'}(\theta_1)\cos\theta_1 d\theta_1 \ . \quad (2.7)$$

Here, θ_C is the critical angle of the incident particles which is needed to ensure propagating particles

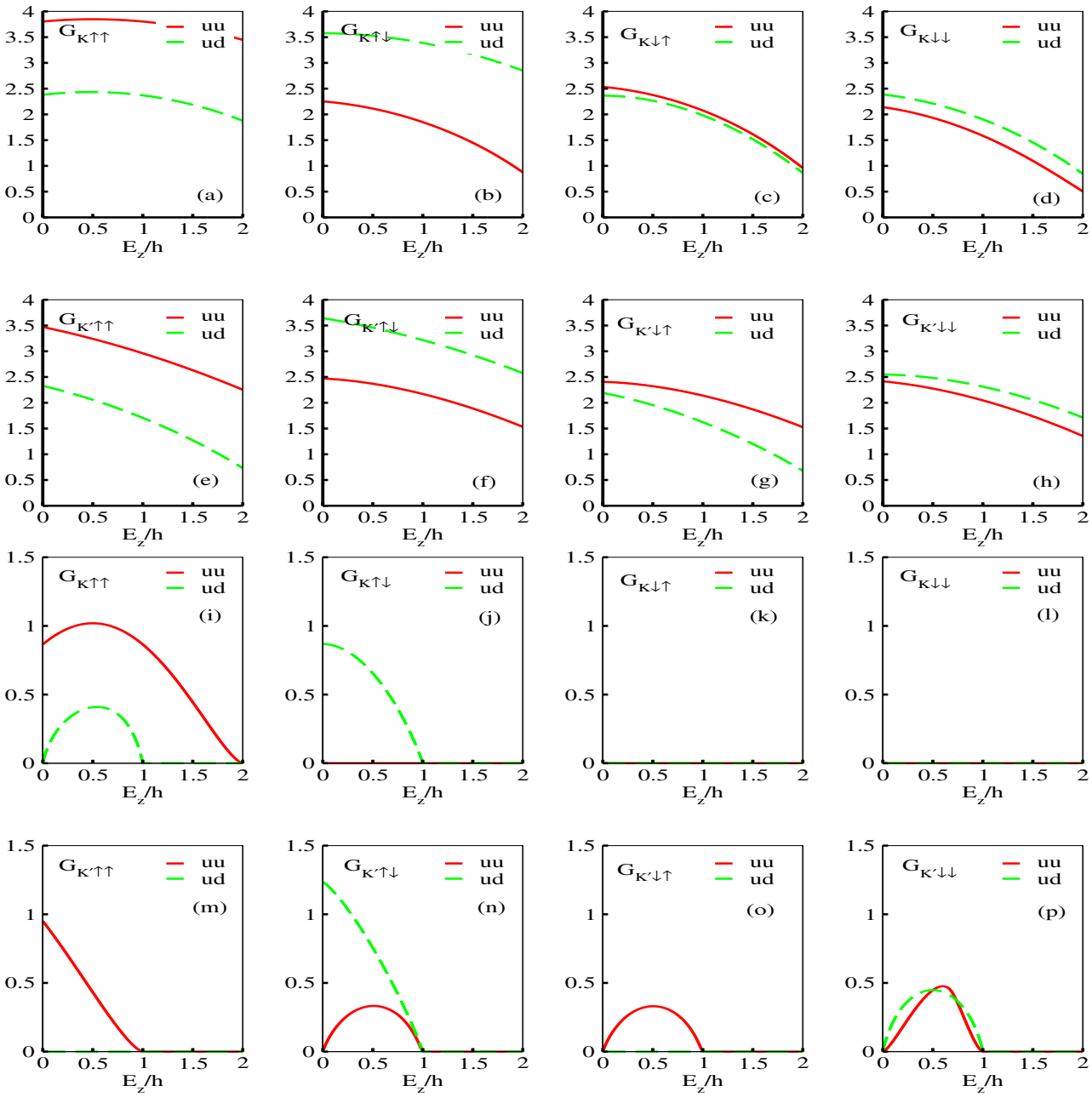

Figure 2.4: Conductances ($G_{V\sigma\sigma'}$) in units of $e^2W/\pi h$, for the P (uu) and AP (ud) configurations of a FNF junction are shown as a function of the dimensionless parameter E_z/h for $E > h$ [upper panels, (a-h)] and $E < h$ [lower panels, (i-p)] respectively. Here E_z is the external electric field and h is the ferromagnetic exchange field. The value of the other parameters are chosen to be $\lambda_{SO}/h = 0.5$, $U/h = 30$. Energy of incident electron, for $E > h$ is $E/h = 4.0$ and for $E < h$ is $E/h = 0.5$.

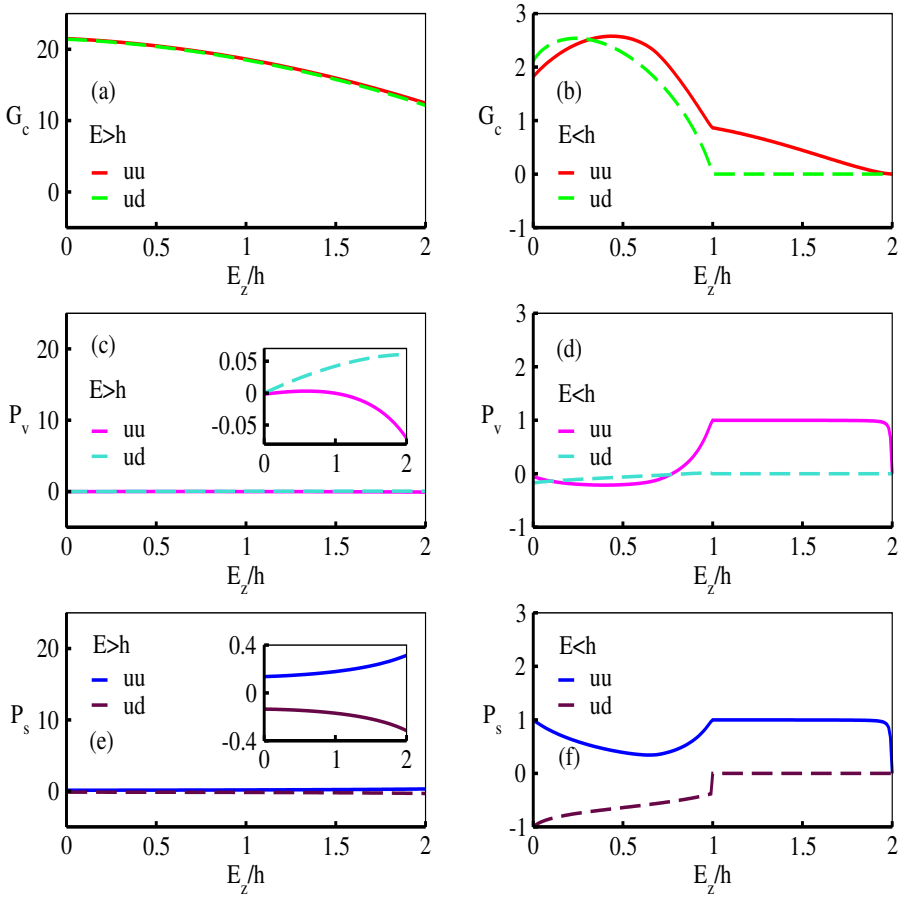

Figure 2.5: Total charge conductance (G_c) in units of $e^2W/\pi h$, valley polarization ($\mathcal{P}_v$) and spin polarization ($\mathcal{P}_S$) for P and AP configurations of a FNF junction are shown as a function of the dimensionless parameter E_z/h for $E > h$ [left panels, (a), (c) and (e)] and $E < h$ [right panels, (b),(d) and (f)] respectively. The value of the other parameters are chosen to be the same as in Fig. 2.4. The insets emphasize that $\mathcal{P}_v$ and $\mathcal{P}_S$ are actually different in magnitude for the uu and ud configurations for $E > h$ regime.

in the first and third regions and is given by $\theta_C = \pi/2$ for $k_1 \leq k_3$ and $\theta_C = \arcsin(k_1/k_3)$ for $k_1 > k_3$. Note that unlike the case for graphene, in silicene, the contributions at the two valleys are not identical and hence, we do not get the degeneracy factor of two. Instead, the contributions at both the valleys have to be computed independently and added to obtain the total conductance through the junction. Thus we define the total charge conductances G_c, valley and the spin polarizations $(\mathcal{P}_v, \mathcal{P}_S)$ and TMR through the FNF junction in terms of the following constituent conductances– $G^{ss'}_{V\sigma\sigma'}$. Here, ss' denotes uu (P) or ud (AP) spin configurations, V denotes the valley ($\mathbf{K}$ or $\mathbf{K'}$) and σ denotes the spin of the incoming charge carrier in region 1 and σ' denotes the spin of the outgoing charge carrier in region 3, which can be different, because we have spin-orbit coupling in the system. These conductances have been shown in Fig. 2.4 for both $E > h$ and $E < h$. It is now easy to realize, in reference to the band diagrams given in Fig. 6.1 that the conductances go to zero when there is a gap in the density of states either in region 1 or 3. The maxima can also be understood by noting that the density of states at those values of E_z/h are maximum and both reduce when E_z/h is reduced or increased. This can be checked for each of the various conductances on a case by case basis.

The total charge conductance $G_c^{ss'}$ and the valley $\mathcal{P}_v^{ss'}$ and spin $\mathcal{P}_S^{ss'}$ polarizations for both the P $(s = s')$ and AP $(s = -s')$ configurations are now defined as

$$\begin{aligned} G_c^{ss'} &= \sum_{V\sigma\sigma'} G^{ss'}_{V\sigma\sigma'} \ , \\ \mathcal{P}_v^{ss'} &= \frac{\sum_{\sigma\sigma'}(G^{ss'}_{\mathbf{K}\sigma\sigma'} - G^{ss'}_{\mathbf{K'}\sigma\sigma'})}{G_c^{ss'}} \ , \\ \text{and} \quad \mathcal{P}_S^{ss'} &= \frac{\sum_{V\sigma}(G^{ss'}_{V\sigma\uparrow} - G^{ss'}_{V\sigma\downarrow})}{G_c^{ss'}} \ . \end{aligned} \tag{2.8}$$

Note that the indices ss' in Eq.(2.8) gives rise to four possible spin configurations uu, ud, du, dd for a FNF junction, of which uu and dd imply P configurations with $s = s'$ and ud and du denote AP configurations with $s = -s'$.

Now from the knowledge of all the possible conductances, one can define the tunneling magnetoresistance (TMR) through the FNF geometry as

$$\text{TMR} = \frac{G_c^{uu} - G_c^{ud}}{G_c^{uu}} \ . \tag{2.9}$$

Note that the standard definition of TMR has G_c^{ud} in the denominator. However it is also sometimes defined with G_c^{uu} [73] and we choose this definition because in our case, G_c^{ud} vanishes at $E_z = h$. This implies a singularity in the TMR which is avoided in our definition. Note that for $E_z > h$, the difference in TMR between the two definitions is negligible. For $E_z < h$, there are numerical differences, but no qualitative difference in the behavior of TMR with the two definitions.

The results are different for the energy regimes $E > h$ and $E < h$, because of the difference in band structure, which has band gaps and hence no propagating states available for transport (see Fig. **??**), for certain ranges of E_z/h for $E < h$. Since the main difference of silicene from graphene is the fact that the gap in silicene is tunable by the external electric field E_z, we choose to focus on the dependence of conductances on E_z. In cases, where we study the conductances as functions of other parameters such as the barrier strength U or the exchange splitting Δ, we present our results for three different values of E_z/h.

Note that when $E_z = \lambda_{SO}$, silicene is actually coplanar, *i.e.* the two sublattices are in same plane like in graphene. But the spin-orbit coupling in silicene is much stronger than in graphene [74]. This increases or decreases the momentum of the incident charge carrier (see Eq.(2.4)) depending on the spin-polarization of the ferromagnetic silicene. Hence, we do not expect to reproduce the results of

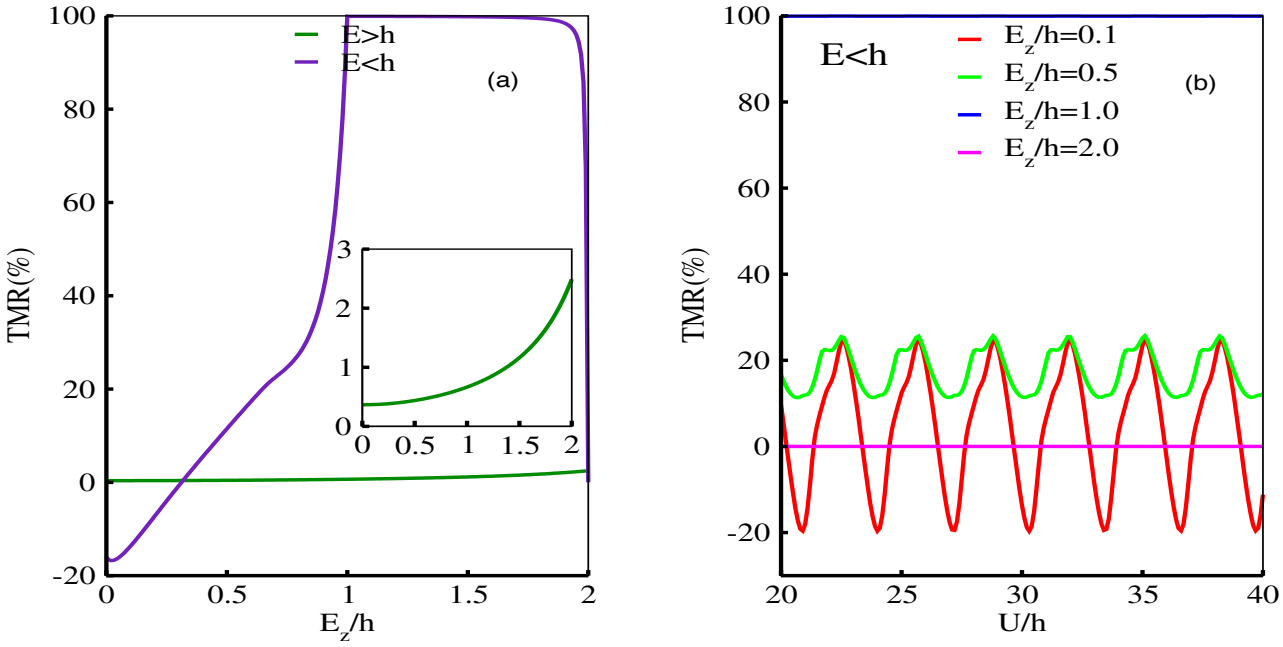

Figure 2.6: TMR is shown as a function of the dimensionless scale E_z/h in panel (a) with green and purple lines corresponding to $E > h$ and $E < h$ regime respectively. In panel (b) TMR is shown as a function of U/h for $E < h$ for three values of E_z/h. The other parameters are chosen to be the same as in Fig. 2.4. In the inset of panel (a) we emphasize the very slow rate of increase of TMR in the $E < h$ regime.

FNF junctions in graphene in the gapless regime.

2.4.1 Spin-independent Barrier

Here we discuss the case where we have a finite spin-independent (scalar) barrier in the normal silicene region. The energy of the incident electron can be in the regime $E > h$ or $E < h$ and we present the behavior of the conductances and the TMR below. To carry out our numerical analyses, we have chosen to normalise all our energy scales by the Zeeman energy h, so that all our results are in terms of dimensionless quantities. We also choose to measure conductances in units of $e^2W/\pi h$.

We first present the results for the various constituent conductances for the P and AP configuration in Fig. 2.4 in order to understand the behavior of the conductances, the valley and spin polarizations and the TMR in various parameter regimes. The conductances are shown independently at the **K** and the **K′** valleys as well as independently for the incoming (σ) and the outgoing (σ') spins of the charge carriers. In Figs. 2.4(a-h), we show the behavior of the conductances at the **K** and **K′** valleys, with respect to the dimensionless parameter E_z/h for the four possibilities $(\uparrow\uparrow, \uparrow\downarrow, \downarrow\uparrow, \downarrow\downarrow)$ in the $E > h$ regime for both the uu and ud configurations. Here the uu configuration corresponds to the majority spin density of states in the left and right FS regions being up spin (parallel to each other) and the ud configuration corresponds to the majority spin being opposite (anti-parallel) in the two regions. When $\uparrow$ charge carrier comes in from the left then it can either go to $\uparrow$ state or $\downarrow$ state in right region. So $\uparrow\uparrow$ etc, denote spins of the incoming and scattered charge carriers. The behavior of the various conductances in Figs. 2.4(a-h) can now be understood easily when analysed in terms of the band structure presented in Fig. 2.3.

For $E > h$, the results have been presented for $E/h = 4$. Using the band diagram, it is easy to

check that both at **K** and **K′**, there are always electron states available for conductance for both the P and AP configurations and for all possible incoming and outgoing spins. The differences in the magnitude both at **K** and **K′** valleys stems from the decrease in the momentum of the propagating states at the Fermi energy, as can be seen from the band diagram.

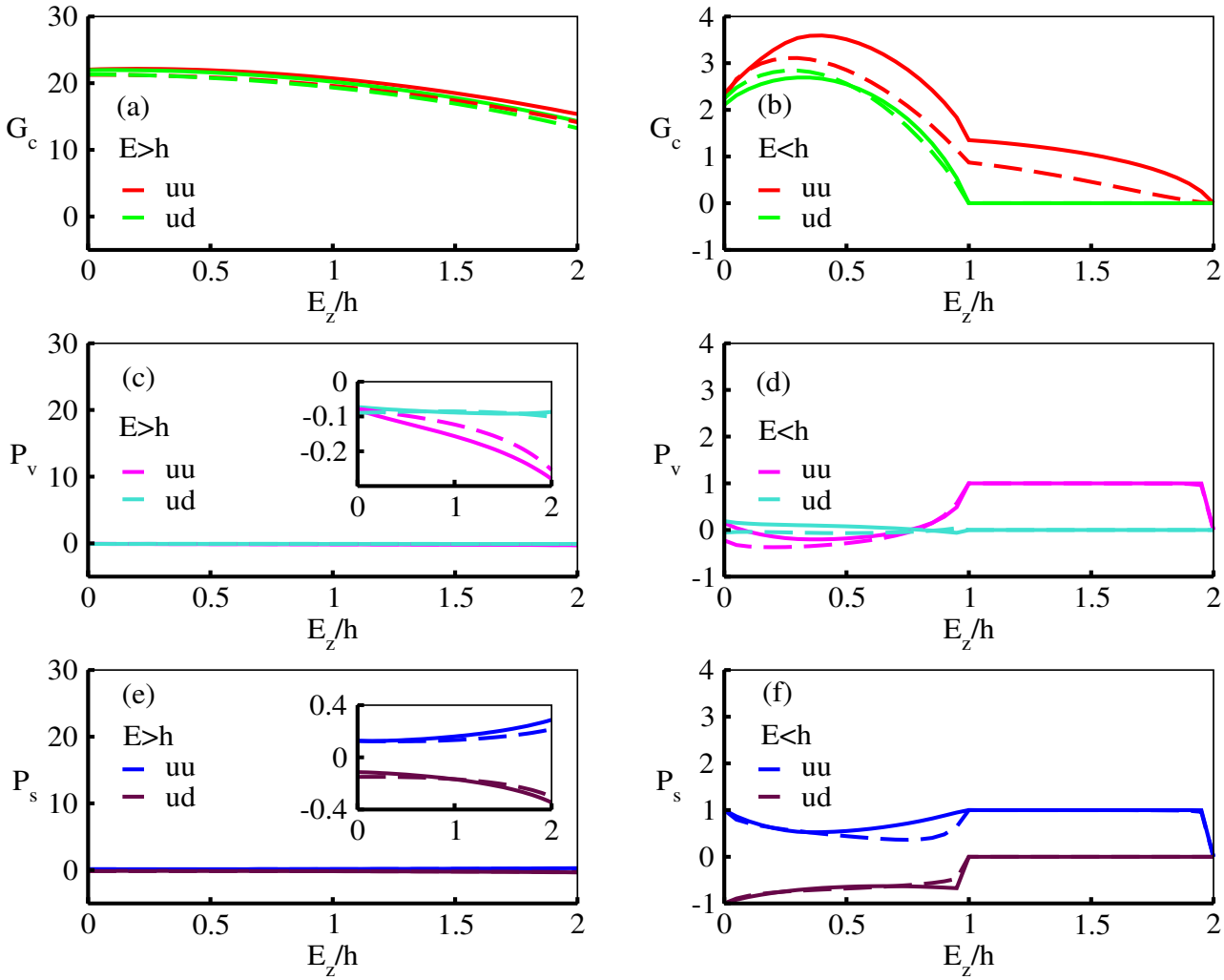

Figure 2.7: In the left panels, we show the total charge conductance (G_c) in units of $e^2W/\pi h$, valley and spin polarizations ($\mathcal{P}_v^{ss'}$, $\mathcal{P}_S^{ss'}$) for $E > h$ and on the right panels for $E < h$ respectively. The dashed and solid lines correspond to two different exchange splittings (Δ/h) due to the spin-dependent barrier in the normal silicene region. The value of the other parameters are chosen to be $\lambda_{SO}/h = 0.5$, $U/h = 30$. Energy of the incident electron, for $E > h$, is $E/h = 4.0$ and for $E < h$, $E/h = 0.5$. The small difference in magnitude of $\mathcal{P}_v^{ss'}$ and $\mathcal{P}_S^{ss'}$ is highlighted in the insets for $E > h$ regime.

The results for $E < h$ is shown in Figs. 2.4(i-p) for $E/h = 0.5$. Consider the uu case for the valleys **K** and **K′**. For $G_{\mathbf{K},\mathbf{K}'\uparrow\uparrow}$, (red lines shown in Fig. 2.4(i) and Fig. 2.4(m)), the band diagram (see Fig. 2.3) shows that if we start with a spin up electron at the **K** valley, (Fig. 2.4(i)) then there is a non-zero density of states for $\uparrow$ electrons in the third region for all values of E_z/h until it reaches the value of 2 (the magenta line goes above the value of $E/h = 0.5$). On the other hand, for the **K′** valley, (shown in Fig. 2.4(m)), there is no density of states for the $\uparrow$ electrons beyond $E_z/h = 1.0$ (the

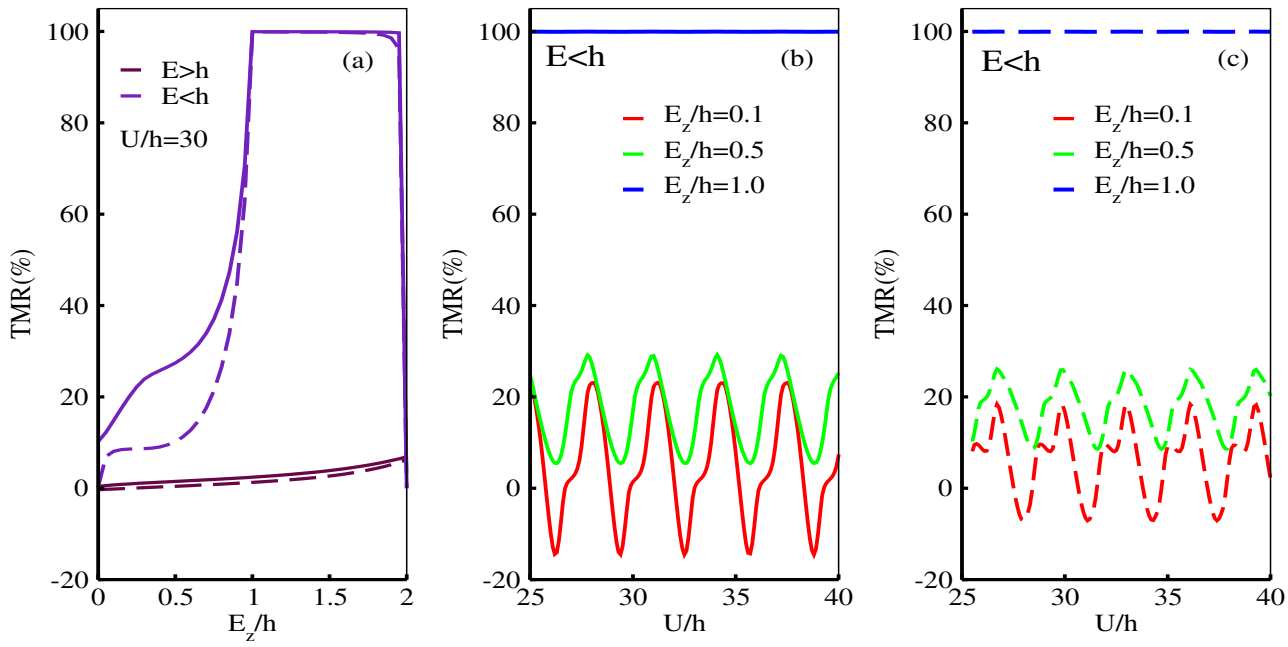

Figure 2.8: The variation of the TMR with respect to E_z/h and U/h is shown for two values of Δ/h. In the panels, the dashed and the solid lines correspond to $\Delta/h = 0.5$ and $\Delta/h = -0.5$ respectively. We choose the same value of the other parameters as mentioned in Fig. 2.7.

blue line goes above the value $E/h = 0.5$) in the third region. This explains why beyond $E_z/h = 2$ for the $\mathbf{K}$ valley and beyond $E_z/h = 1$ for the $\mathbf{K}'$ valley, the conductances $G^{uu}_{\mathbf{K}\uparrow\uparrow}$ and $G^{uu}_{\mathbf{K}'\uparrow\uparrow}$ are zero. It is also clear from the band diagram that for $G^{uu}_{\mathbf{K}\uparrow\uparrow}$, its value increases from the value at $E_z/h = 0$, because the momenta of the electrons at $E/h = 0.5$ grows (comparing the red and green lines) and beyond that it decreases (comparing the green, blue and magenta lines). On the other hand, for $G^{uu}_{\mathbf{K}'\uparrow\uparrow}$, it is clear that the momentum of the electrons at $E/h = 0.5$ decreases as a function of E_z/h (comparing the red, green and blue lines). This explains why the conductance rises initially and then falls beyond $E_z/h = 0.5$ for $G^{\uparrow\uparrow}_{\mathbf{K}}$ and why it falls monotonically for $G^{\uparrow\uparrow}_{\mathbf{K}'}$.

A similar detailed analysis can also be made for the ud case as well as each of the other graphs in Figs. 2.4(j,k,l) and Figs. 2.4(n,o,p), which explains each feature of the graph. However, since the method is similar to what has been described above, we will not go through each one of the graphs in detail. The behavior of the charge conductance, the valley and spin polarizations and the TMR are also now understandable, since we can explain how each of the constituents $G^{ss'}_{V\sigma\sigma'}$ behave as a function of E_z/h from the band diagram.

(a) $E > h$

In Figs. 2.5(a), 2.5(c) and 2.5(e), we show the behavior of the charge conductance ($G^{ss'}_c$) and the valley and spin polarizations ($\mathcal{P}^{ss'}_v$ and $\mathcal{P}^{ss'}_S$) with respect to the dimensionless parameter E_z/h for the P and AP configurations (uu and ud) in the $E > h$ regime. Note that in Fig. 1.3(a), G^{uu}_c and G^{ud}_c are both finite at $E_z/h = 0$ and start decreasing as we increase the value of E_z/h. G_c is obtained by summing $G^{ss'}_{\mathbf{K}}$ and $G^{ss'}_{\mathbf{K}'}$, which in turn are obtained as

$$\begin{aligned} G^{ss'}_{\mathbf{K}} &= (G^{ss'}_{\mathbf{K}\uparrow\uparrow} + G^{ss'}_{\mathbf{K}\uparrow\downarrow}) + (G^{ss'}_{\mathbf{K}\downarrow\uparrow} + G^{ss'}_{\mathbf{K}\downarrow\downarrow}) \\ &\equiv \sum_{\sigma'} G^{ss'}_{\mathbf{K}\uparrow\sigma'} + G^{ss'}_{\mathbf{K}\downarrow\sigma'} \end{aligned} \tag{2.10}$$

and similarly for $G^{ss'}_{\mathbf{K}'}$. In other words, the total charge conductance $G^{ss'}_c = G^{ss'}_{\mathbf{K}} + G^{ss'}_{\mathbf{K}'}$ is obtained by summing over all the conductances in the panels (a) to (h) in Fig. 2.4.

In Fig. 2.5(c), $\mathcal{P}^{uu}_v$ and $\mathcal{P}^{ud}_v$ are plotted which are close to zero on the scale of the charge conductance. However, they are not identical, as shown in the inset. But it appears that in this regime, silicene has negligible valley polarization, similar to graphene, which in fact has no valley polarization at all, since the two valleys are identical. This can be understood because the valley polarization $\mathcal{P}_v$ is simply proportional to $G^{ss'}_{\mathbf{K}} - G^{ss'}_{\mathbf{K}'}$, and as can be seen from Fig.2.4 that the magnitudes of the conductances at $\mathbf{K}$ and $\mathbf{K}'$ are almost the same for $E > h$. In Fig. 2.5(e), the behavior of the spin polarization has been shown for both P (uu) and AP (ud) configurations, which is also very small in this regime. As shown in the inset, the spin polarization is positive for the P and negative for the AP configurations and increases as a function of E_z/h. This difference is due to the spin-orbit coupling in silicene, whereas in graphene, they are much smaller, since the spin-orbit coupling is vanishingly small. Finally, in Fig. 2.6(a), the behavior of the TMR is shown as a function of E_z/h by the green solid line in the $E > h$ regime. In this regime, the TMR is close to zero.

(b) $E < h$

The right panels in Fig. 2.5 shows the behavior of the charge conductance $G^{ss'}_c$ and the valley and spin polarizations $\mathcal{P}^{ss'}_v$, $\mathcal{P}^{ss'}_S$ with respect to the dimensionless parameter E_z/h, in the $E < h$ regime, for the same spin and polarization configurations mentioned earlier. These are just the appropriate sums and differences of the constituent conductances in Figs. 2.4(i-p). Here also, their behavior is easy to understand by comparing each of the graphs in Figs. 2.4(i-p) with the band diagrams in Fig. 2.3 and noting when there is no density of states for the configuration in either the incoming or the outgoing spin configuration of the charge carriers. For instance, for the uu case, there is only one contribution for $E_z/h > 1$ in Fig. 2.4(i) and for the ud case, there is no contribution for $E_z/h > 1$. This is because we have chosen $E/h = 0.5$ and the blue line ($E_z/h = 1.0$) in the band diagram goes above that line either for the incoming or scattered region for all cases in the ud configuration and all but one case in the uu configuration. In other words, their behavior follows what is expected from the availability or non-availability of propagating states at the $\mathbf{K}$ and $\mathbf{K}'$ valleys as explained above in the discussion of Fig. 2.4.

The most interesting point to note is that the valley polarization and the spin polarization for the parallel or uu configuration is unity for $E_z/h > 1$ in $E < h$ regime. This is simply because of the entire contribution to the conductance in this regime originates from $G^{uu}_{\mathbf{K}\uparrow\uparrow}$. So the conductance is both fully valley and spin polarised and would be an important regime to achieve by tuning the incident electron energy $E/h < 1$ and the electric field $E_z/h > 1$. In the anti-parallel or ud regime, the spin polarization can be tuned to negative values when $E_z/h < 1$, but without any valley polarization.

The behavior of TMR is demonstrated in Figs. 2.6(a) and 2.6(b) for the $E < h$ regime. For $E_z/h = 0$, the TMR is negative and reaches its maximum negative value. Then the TMR increases as we increase the value of E_z/h and changes sign and reaches saturation at $E_z/h \simeq 1$ since the conductance becomes fully spin polarised at that point. Note that we need to restrict the value of E_z/h below two as the TMR takes an indeterminate form at $E_z/h = 2$ due to the vanishing of both G^{uu}_c and G^{ud}_c (see Fig.1.3(c) and Eq.(2.9)) for all spin configurations. This is a consequence of our choice of the incident energy at $E/h = 0.5$.

The striking feature of positive to negative transition in the TMR also arises as we vary the strength of the potential barrier U in the middle normal silicene region for different values of E_z/h. This feature is shown in Fig. 2.6(b) where the TMR oscillates between positive and negative values with respect to U for $E_z/h = 0.1$. Such oscillations of the TMR from positive to negative values have been reported earlier in Ref. [71] in graphene, due to the change in the type of the charge carrier in the third region. Note also there is no significant qualitative change in the behavior of TMR even

if we choose $U \sim h$. This extra tunability of the TMR with respect to an external electric field is a unique feature of silicene that we wish to emphasize here.

2.4.2 Spin-dependent Barrier

Here we discuss the effect of a spin-dependent barrier on the total charge conductance, valley and spin polarizations and the TMR. The barrier is modelled in the normal silicene region as $U_\sigma = U - \sigma\Delta$ which is shown in Fig. 2.2. Here positive (negative) Δ represents the exchange splitting in the silicene barrier with its magnetization parallel (anti parallel) to the spin orientation of the FS in the first region.

In Figs. 2.7(a-f) we show the behavior of the total charge conductances $G_c^{ss'}$, spin and valley polarizations $\mathcal{P}_S^{ss'}$ and $\mathcal{P}_v^{ss'}$, in the $E > h$ and $E < h$ regimes, for $\pm\Delta/h$. Since the qualitative behavior of all the conductances remain similar to the spin independent barrier case, we do not show the behavior of the conductances at the **K** and **K′** valleys independently, or analyse the graphs in detail via the band structure. Similarly, in Figs 2.8(a-c), we show the behavior of the TMR as a function of E_z/h and as a function of U/h as well (for $E_z < h$), for both $\pm\Delta/h$. We find that the results are fairly similar to the spin-independent barrier case.

2.5 Conclusion

To summarize, in this paper, we have investigated the transport properties (charge conductance as well as spin and valley polarizations) and the TMR through an FNF junction in silicene. Here we have adopted the Landauer-Buttiker formalism to carry out our analysis. We show that the conductances and the TMR in this geometry can be tuned by an external electric field E_z for each case ($\uparrow\uparrow$, $\uparrow\downarrow$, $\downarrow\uparrow$, $\downarrow\downarrow$) in the left and right ferromagnetic silicene regions, for both parallel (uu or dd) and anti-parallel (ud or du) configurations. For specific values of the electric field, we analyse both the charge conductance and valley and spin polarization in terms of the independent behavior of the conductances at the two valleys and the band structure at specific incident energies. We find that we can tune a full valley polarised and also a fully spin polarised current through our setup via the external electric field. We also find that the TMR can be tuned to 100 % in this geometry via the electric field. This is one of the main conclusions of our analysis. We also show that the TMR through our setup exhibits an oscillatory behavior as a function of the strength of the barrier (both spin independent and spin-dependent) in the normal silicene region. The TMR also changes sign between positive and negative values and such a transition can be tuned by the external electric field. This is another conclusion of our analysis. Hence, from the application point of view, our FNF geometry may be a possible candidate for making future generation spintronic devices out of silicene.

As far as the practical realization of such an FNF structure in silicene is concerned, it should be possible to fabricate such a geometry with the currently available experimental techniques. Ferromagnetic exchange in silicene may be achieved via proximity effect using a magnetic insulator, for instance, EuO [70, 75]. The typical spin orbit energy in silicene is $\lambda_{SO} \sim 4$ meV [74]. For an incident electron with energy $E \sim 4$ meV and exchange energy $h \sim 8$ meV, the maximum value of the spin and valley polarization as well as sign change of TMR from positive to negative value occur at an electric field $E_z \sim 0.03$ V$\mathring{\text{A}}^{-1}$, potential barrier of height $U \sim 160$ meV, exchange splitting in the normal silicene region $\Delta \sim 4$ meV and width of the barrier $L \sim 100$ nm.

Chapter 3

Periodically Driven Systems

Topological insulators and topological phase transitions [76] have been at the forefront of research in the last several years. More recently, it has been realized that driving systems periodically is an effective way to obtain and control topological phases [39, 77, 78, 79]. In the last few years, the concept of engineering such periodically driven systems, often called Floquet systems, has gained prominence, particularly due to the feasibility of experiments in solid state[80] as well as in photonic[32] and cold atom systems[33]. Floquet topological systems have been studied extensively to predict non-equilibrium Majorana modes[81, 82, 83, 84], non-trivial transport properties[85, 86, 87, 88, 89] as well as to control the band-structure[78, 90, 91].

Despite this progress, there remain many unresolved questions involving driven topological systems, mainly because the presence of the driving implies that the system is out of equilibrium. With the lack of energy conservation, the bands in a driven system can be characterized by *quasienergies* [92]. But the standard picture of assuming that the quasi-energy levels are similar to the usual energy levels of a band is not quite right because the distribution function for the electrons in the quasi-energy bands cannot be assumed to be the usual Fermi distribution function. Furthermore, a driven system has a much richer topological phase structure than its static counterpart[30] and may even possess phases that have no analog in the static system [31]. This has led to the proposal of characterising the topological indices of a periodically driven topological insulator as a combination of winding numbers instead of a single Chern number.

3.1 Floquet-Bloch band theory

Floquet theory is a framework to deal with the periodic quantum system either in space (static system) or in time (dynamic system). We are interested in the Hamiltonians which are periodic in time i.e.

$$H(t) = H(t+T) \tag{3.1}$$

The Schrödinger equation for a quantum system can be written as -

$$\left(H(r,t) - i\hbar\frac{\delta}{\delta t}\right)\Psi(r,t) = 0 \tag{3.2}$$

According to Floquet theorem, there exist solutions to the above equation that have the form -

$$\Psi_\alpha(r,t) = e^{-i\epsilon_\alpha t/\hbar}\Phi_\alpha(r,t) \tag{3.3}$$

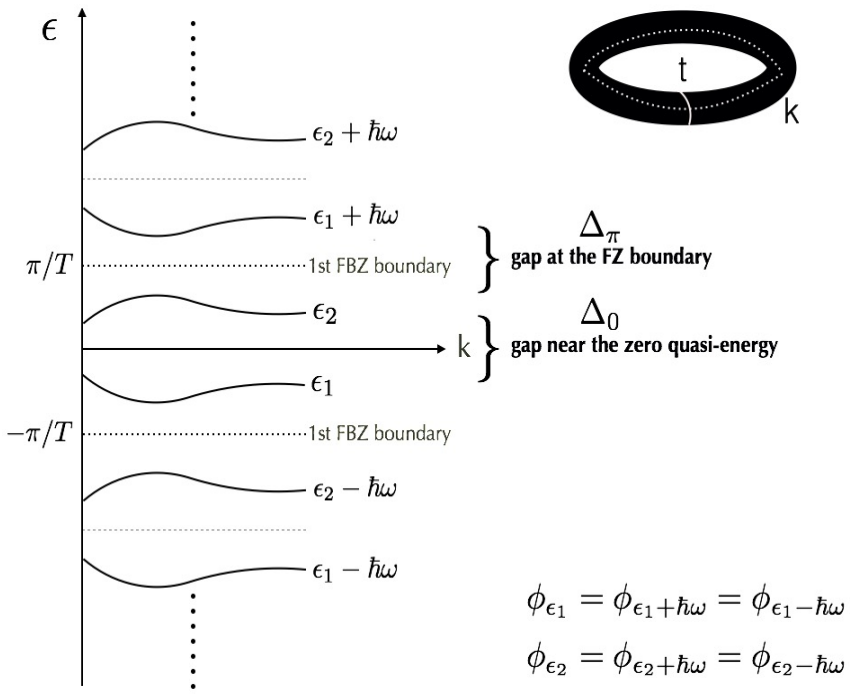

Figure 3.1: The schematic diagram of extended Floquet zone scheme for a two band model.

where, Φ_α are periodic function in time i.e. $\Phi_\alpha(r,t) = \Phi_\alpha(r,t+T)$. Putting eq.(3.3) into the Schrödinger equation -

$$\mathcal{H}(r,t)\Phi_\alpha(r,t) = \epsilon_\alpha \Phi_\alpha(r,t) \tag{3.4}$$

where, $\mathcal{H}(r,t) = H(r,t) - i\hbar\frac{\partial}{\partial t}$ and ϵ_α is the quasienergy for the eigenvalue equation 3.4. Since the Floquet modes Φ_α are periodic in time we notice that

$$\Phi'_\alpha(r,t) = \Phi_\alpha(r,t)\ e^{-in\omega t} \equiv \Phi_{\alpha n}(r,t) \tag{3.5}$$

gives the same solution as eq.(3.3)

$$\begin{aligned}\Psi_\alpha(r,t) &= e^{-i\epsilon_\alpha t/\hbar} e^{-in\omega t}\Phi_\alpha(r,t) \\ &= e^{-i(\epsilon_\alpha + n\hbar\omega)t/\hbar}\Phi_\alpha(r,t)\end{aligned} \tag{3.6}$$

but with the shifted quasienergy $\epsilon'_\alpha = \epsilon + n\hbar\omega$. Here, the index α corresponds to a whole class of solutions indexed by $\alpha' = (\alpha, n)$; $n = 0, \pm1, \pm2, ...$ The eigenvalues ϵ_α therefore can be mapped into a Brillouin zone, $-\hbar\omega/2 \leq \epsilon \leq \hbar\omega/2$. It means all states eq.(3.5) with n being an integer number $n = 0, \pm1, \pm2, ..$ gives identical solutions which belong to the same physical state $\Psi_\alpha(r,t)$. We now introduce the composite Hilbert space $\mathcal{R} \otimes \mathcal{T}$ where $\mathcal{T}$ is the space of time-periodic functions. We explain this extended zone scheme schematically for a two-band model below.
Suppose that we have a two-level system characterized by two energy labels ϵ_1 and ϵ_2 which now exposed to an external periodic electromagnetic radiation. Due to the time periodicity, the conjugate variable, energy is conserved and it is called the quasienergy like we have conserved quasi-momentum for translationally invariant systems. The inequivalent quasienergies lie within the range $[-\pi/T,$

$\pi/T]$. There exist infinitely many states $\phi_{\epsilon_1 \pm \hbar\omega}, \phi_{\epsilon_1 \pm 2\hbar\omega}, \phi_{\epsilon_1 \pm 3\hbar\omega}, ..$ which are equivalent to ϕ_{ϵ_1} but have shifted quasienergies $\epsilon_1 \pm \hbar\omega, \epsilon_1 \pm 2\hbar\omega, \epsilon_1 \pm 3\hbar\omega, ..$ respectively as shown in fig.(3.1). The same is true for the other state at ϵ_2. We notice that we have an inequivalent gap at the Floquet zone boundary other than the gap near zero quasienergies. We label the gap at Floquet zone boundary by Δ_π and the gap near zero quasienergies by Δ_0. These gaps can close and reopen as we vary the parameters of the system and the edge states can appear at any of these gaps or at both gaps.
It is clear that when the drive frequency is larger than the bandwidth then the Floquet zone boundary is not accessible and hence the system can exhibit edge states only near zero quasienergy but when system couples with the external light resonantly then the gap at Floquet zone boundary makes a crucial difference in determining the correspondence between the bulk topology and the number of edge states in periodically driven system. We analyse this interesting consequence at length in the next chapter.

3.2 Brillouin-Wigner (B-W) Perturbation Theory

A simple theoretical idea that has been used in the field of Floquet systems is to realize that at very high frequencies when the frequency of the drive is larger than the bandwidth, the system cannot follow the rapid oscillations of the external drive and hence, the effective Hamiltonian is just the time-averaged one. An effective Hamiltonian is then systematically constructed using perturbation theory, at high frequencies, to include virtual photon absorption and emission processes to give corrections of $O(\omega^{-n})$, where ω is the frequency. Here, it has been shown that at least at high frequencies, in models like graphene, the assumption that the quasi-energies can be treated as usual energy levels works well.

In an earlier work, Ezawa[97] investigated photo induced phase transitions in silicene and showed that at high frequencies, various new phases such as the quantum Hall insulator, spin-polarized quantum Hall insulator, spin polarized metal and spin-valley polarized metal are realized. However, his study was restricted to high frequencies of $O(\omega^{-1})$ in the high-frequency expansion and also to low energies, close to the Dirac cone. Here, we study a systematic Brillouin-Wigner (B-W) expansion [47] of the effective Hamiltonian of systems with a spin-orbit coupling term, and obtain the effective Hamiltonian to $O(\omega^{-2})$, without restricting ourselves to the low energy limit. To obtain the phase diagram, which should be qualitatively applicable to all materials with spin-orbit couplings such as silicene, germanene, and stanene, we keep the spin-orbit term small but arbitrary. Thus we are able to access many more phases in the spin-polarized, buckled systems.

In this paper, we will only use the B-W theory, since, with the addition of spin-orbit couplings, we have even more terms and the recursive technique can be conveniently used to compute the higher order terms. We start with a time-periodic Hamiltonian $H(\tau + T) = H(\tau)$, where $T = 2\pi/\omega$ is the period, given by its Fourier components

$$H_n = \int_0^T \frac{d\tau}{T} H(\tau) e^{in\omega\tau}. \tag{3.7}$$

The B-W perturbation theory can now be used to obtain the effective Hamiltonian order by order in $1/\omega$ as[47]

$$H_{\mathrm{BW}} = \sum_{n=0}^{\infty} H_{\mathrm{BW}}^{(n)} \tag{3.8}$$

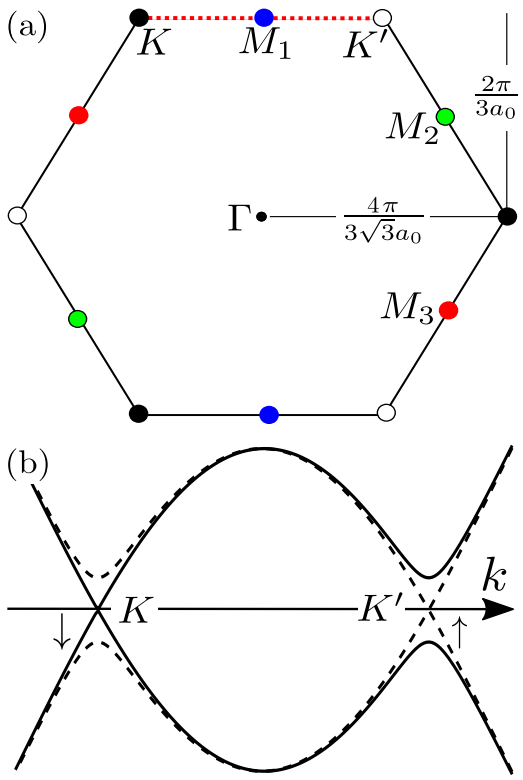

Figure 3.2: (a) The hexagonal Brillouin zone for the model that we consider with various high-symmetry points (discussed in the text) marked. (b) The band structure with momenta along the red dotted line in (a) in the presence of spin-orbit coupling and a staggered electric field E_z. It is possible to have Dirac nodes for different spins at different valleys. A spin-orbit coupling constant of $\lambda = 0.1t$ and a staggering potential of $lE_z = 0.1t$ have been used to obtain the schematic diagram presented here.

where, the first few orders are:

$$\begin{aligned} H^{(0)}_{\rm BW} =& H_0 \\ H^{(1)}_{\rm BW} =& \sum_{n\neq 0} \frac{H_{-n}H_n}{n\omega} \\ H^{(2)}_{\rm BW} =& \sum_{n,m\neq 0} \left(\frac{H_{-n}H_{n-m}H_m}{nm\omega^2} - \frac{H_{-n}H_nH_0}{n^2\omega^2} \right). \end{aligned} \tag{3.9}$$

As an example-system, it is useful to consider electrons in a honeycomb (hc) lattice (say, graphene) irradiated by circularly polarized light. The time independent Hamiltonian is modelled by a lattice Hamiltonian of fermions with uniform nearest neighbour (NN) hoppings given by

$$H^{\rm hc} = -t \sum_{\langle i,j\rangle,\sigma} c^\dagger_{i\sigma} c_{j\sigma} \ . \tag{3.10}$$

The effect of the radiation can be taken into account by the vector potential $\mathbf{A}(\tau) = A_0(\cos\omega\tau, \sin\omega\tau)$. The Hamiltonian, using Peierls substitution, is then given by

$$H^{\rm hc}(\tau) = -t\sum_{\langle i,j\rangle} e^{-i\alpha\sin(\omega\tau - 2\pi l/3)} c_i^\dagger c_j \ . \tag{3.11}$$

where $l = 0, 1, 2$ for the three NNs in the honeycomb lattice, i.e. $R_j = R_i + \delta_l$ and $\alpha = A_0 a_0$ with a_0 being the lattice constant. We have dropped the spin index as the Hamiltonian is the same for either spin sector. The Fourier components of the Hamiltonian are,

$$H_n^{\rm hc} = -t\sum_{\langle i,j\rangle} e^{i\frac{2\pi n l}{3}}\ J_n(\alpha) c_i^\dagger c_j, \tag{3.12}$$

where J_n is the Bessel function of order n. Using Eq. (3.9) one obtains the effective B-W Hamiltonian upto the first order in (t/ω) as

$$H_{\rm BW}^{\rm hc} = -\sum_{\langle i,j\rangle} J c_i^\dagger c_j + \sum_{\langle\langle i,j\rangle\rangle} i\nu_{ij}\Lambda c_i^\dagger c_j, \tag{3.13}$$

where,

$$J = tJ_0(\alpha), \quad \Lambda = -\frac{t^2}{\omega}\sum_{n\neq 0}\frac{J_n^2(\alpha)}{n}\sin\frac{2\pi n}{3}. \tag{3.14}$$

$\nu_{ij} = \pm 1$ depending on whether the next to nearest neighbour (NNN) hopping is clockwise or anti-clockwise. The first term represents a renormalized hopping amplitude, whereas the second term can open a gap in the system, driving the system to the topological regime.

Now, we introduce a generic 2D Hamiltonian on a honeycomb lattice to describe systems with spin-orbit (SO) coupling as well as to allow a buckled structure where the atoms of the sub-lattices are separated in the direction perpendicular to the plane of the lattice. Materials such as silicene, germanene and stanene can be effectively described by such a model. Cold-atom systems can also be used to simulate these kinds of effective models.

The SO coupling can be introduced by adding a next to nearest neighbour (NNN) term in the Hamiltonian [93]

$$H^{\rm SO} = \frac{i\lambda}{3\sqrt{3}}\sum_{\langle\langle i,j\rangle\rangle\sigma}\sigma\nu_{ij}c_{i\sigma}^\dagger c_{j\sigma}. \tag{3.15}$$

λ controls the strength of the SO coupling, σ is the spin index and stands for $\uparrow$ and $\downarrow$ as indices and ± 1 in equations. We note that this takes into account only the time-reversal (TR) invariant *intrinsic* SO coupling. The other prominent SO effect, Bychkov-Rashba effect, has been neglected in the following discussions and is expected to be small in the systems of our interest[94].

The staggered sub-lattice potential originating from a buckled structure can be represented as an onsite potential [97] given by

$$H^{\rm ST} = \sum_{i\sigma}(\zeta_i l E_z - \mu)c_{i\sigma}^\dagger c_{i\sigma}, \tag{3.16}$$

where $2l$ is the separation between the atoms on the A and B sub-lattices and E_z is the applied

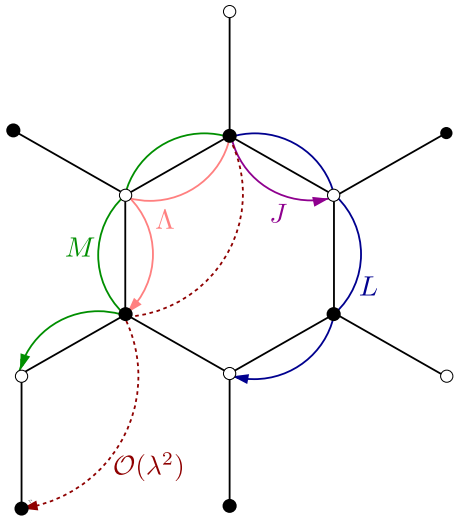

Figure 3.3: The various effective coupling paths in a honeycomb lattice obtained by B-W expansion. Note that for the L- paths, there are two ways, both involving three hoppings, to reach the B sublattice from A. (Only one of them is shown). They contribute equally and we write them together in the amplitude Eq. (3.24) that enters the Hamiltonian. The $\mathcal{O}(\lambda^2)$ contribution (dotted path) vanishes.

electric field. $\zeta_i = +1/-1$ for A/B sub lattices. The full Hamiltonian is thus

$$H = H^{\text{hc}} + H^{\text{SO}} + H^{\text{ST}}. \tag{3.17}$$

We briefly note that the low energy limit of the above Hamiltonian near the K and K' points in the Brillouin zone has a Dirac structure given by

$$H^{\eta}_{\sigma} = \begin{pmatrix} \Delta^{\eta}_{\sigma} - \mu & v(\eta q_x - i q_y) \\ v(\eta q_x + i q_y) & -\Delta^{\eta}_{\sigma} - \mu \end{pmatrix} \tag{3.18}$$

where $v = 3ta_0/2$, $\Delta^{\eta}_{\sigma} = lE_z + \eta\sigma\lambda$ and $\eta = \pm 1$ are the valley indices for the two valleys K and K' (see Fig. 3.2) at momenta $\left(\pm\frac{4\pi}{3\sqrt{3}a_0}, 0\right)$. Squaring the Hamiltonian, we get the eigenvalues $E_{\eta}(q) = -\mu \pm \sqrt{v^2(q_x^2 + q_y^2) + \Delta^{\eta}_{\sigma}{}^2}$. The Dirac mass term or the gap in the system is controlled by Δ^{η}_{σ}. The Hamiltonian Eq. (3.17) is time-reversal symmetric, but the system can be tuned from a trivial semimetal to a spin-hall insulating state by an applied electric field E_z, by tuning Δ^{η}_{σ} through zero.

3.3 Effective time-independent Hamiltonian

In this section, we describe the procedure followed in the B-W calculation. We will start by performing a Peierls substitution on Eq. 3.17 to incorporate the effect of shining circularly polarized laser. The time-dependent Hamiltonian thus obtained is used to calculate the Floquet Hamiltonian using Eq. 3.7. Using Eq. 3.9, the B-W effective Hamiltonian up to $O(\omega^{-2})$ is computed.

We first rewrite the static Hamiltonian in Eq. 3.17 in terms of a and b electrons for the A and B

sublattice as

$$H \equiv \sum_{\langle i,j\rangle\sigma} J_\sigma a^\dagger_{i\sigma} b_{j\sigma} + \sum_{\langle\langle i,j\rangle\rangle\sigma} (i\Lambda^0_\sigma \nu^A_{ij} + \Lambda^A) a^\dagger_{i\sigma} a_{j\sigma} + \sum_{i\sigma} \tilde{\mu}^A a^\dagger_{i,\sigma} a_{i,\sigma} + \text{all terms with } a, A \leftrightarrow b, B \tag{3.19}$$

with $J_\sigma = -t$, $\Lambda^0_\sigma = \frac{\sigma\lambda}{3\sqrt{3}}$, $\Lambda^{A,B} = 0$, $\nu^A_{ij} = -\nu^B_{ij} = \nu_{ij}$. The reason for the introduction of the new notation will become clear when we start computing the corrections to the various terms using the B-W expansion. In comparison with the earlier work on the honeycomb lattice, this model has an NNN term because of the spin-orbit coupling and also a potential difference between the A and B sublattices due to the applied electric field E_z. Our aim is to see how this affects the terms in the B-W expansion.

As mentioned earlier, the effect of shining circularly polarized light with a vector potential $\mathbf{A}(\tau)$ on the two-dimensional honeycomb lattice is obtained by using the Peierls substitution. Note that, $\mathbf{A}\cdot\delta_A = \alpha\sin(\omega\tau - 2\pi l/3)$ whereas $\mathbf{A}\cdot\delta_B = -\alpha\sin(\omega\tau - 2\pi l/3)$, for the A and B sublattices. The band gap at the two valleys K and K' can be tuned by the applied electric field E_z and also by the spin-orbit coupling term λ, whose value can be changed by the time-dependent perturbation, as we shall see below. Hence, the tunability of the band gap is highly enhanced by time-dependent perturbations.

The electric field from the irradiation couples with both the NN and the NNN hopping. Among the nearest neighbor (NN) hopping terms, the sites in the A and B sub-lattices have three neighbours each. In addition, the Peierls substitution has to be performed for the six next to nearest neighbour (NNN) sites in both the sub-lattices. The computation is more tedious than that of the NN case. The Floquet Hamiltonian is calculated by integrating the resulting time dependent Hamiltonian using Eq. 3.7.

We now use the B-W expansion defined in Eq. (3.9) to obtain the effective Hamiltonian to $\mathcal{O}(\omega^{-2})$ in real space. The real space expansion is specially useful for obtaining a physical understanding of the perturbation. In realistic materials, the intrinsic spin-orbit coupling can range from a few milli-electron volts (silicene) to a few tens of milli-electron volts (germanene and stanene) [95, 96]. The band-width of these materials, on the other hand, are of the order of a few electron volts. This difference in magnitude allows us to neglect higher order terms in λ, at higher orders in $\mathcal{O}(1/\omega)$, while showing the results below. In general, such approximations are not necessary, and the B-W effective Hamiltonian can be obtained exactly at each order, particularly for numerical purposes. We briefly sketch the procedure for this in the Appendix.

With this in mind, we compute all the terms to $\mathcal{O}(1/\omega)$ and find that terms of $\mathcal{O}(\lambda^2)$ cancel. To the next order, we keep only $\mathcal{O}(t^3/\omega^2)$ terms. First, the expansion renormalizes various hopping amplitudes J_σ, Λ^0_σ, $\Lambda^{A,B}_\sigma$ and $\tilde{\mu}^{A,B}_\sigma$ in Eq. (3.19) and we call the renormalized Hamiltonian $H^I_{\rm BW}$. Second, the expansion also produces longer range hopping terms of the form

$$H^{II}_{\rm BW} = \sum_{i,j,\sigma}^{L-\text{path}} L_\sigma a^\dagger_{i\sigma} b_{j\sigma} + \sum_{i,j,\sigma}^{M-\text{path}} M_\sigma a^\dagger_{i\sigma} b_{j\sigma} + \text{h.c.} \tag{3.20}$$

The different L and M paths as well as the nearest neighbour J and next nearest neighbour Λ paths are shown in Fig. 3.3. The total effective B-W Hamiltonian is then

$$H_{\rm BW} = H^I_{\rm BW} + H^{II}_{\rm BW}. \tag{3.21}$$

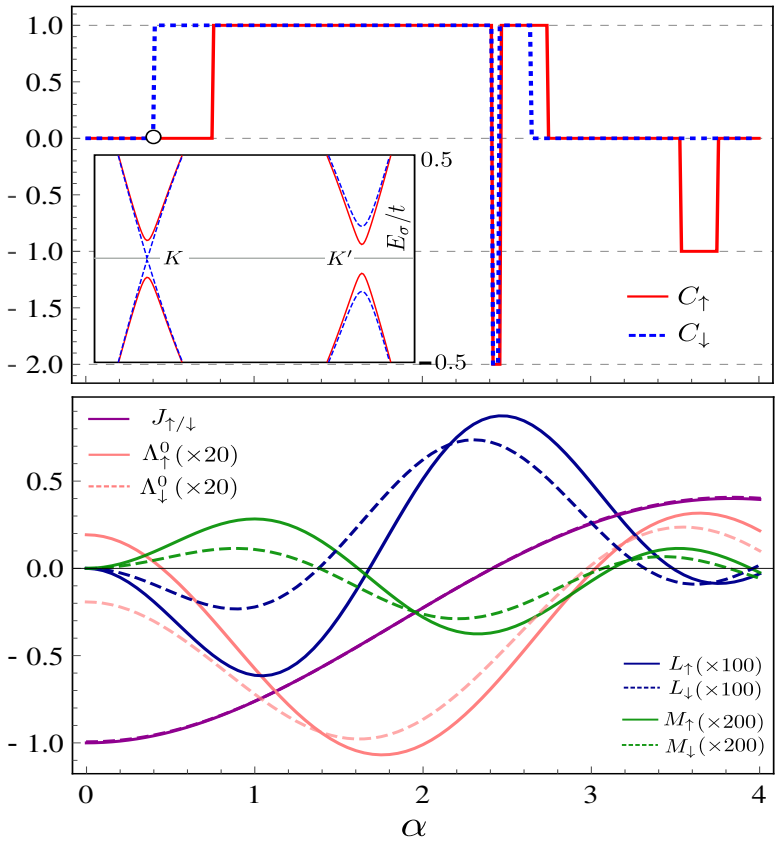

Figure 3.4: The Chern numbers (above) and the various amplitudes of hopping (below) are shown as a function of $\alpha = a_0 A_0$. An arbitrary spin orbit coupling $\lambda = 0.05$, a staggered potential $lE_z = 0.08t$ and $\omega = 10$ have been used. The original hopping amplitude t is taken as the unit of energy. We note that, as the hopping amplitudes differ between the two spin sectors, it is possible to achieve a spin-filtered system in the presence of SO coupling and the staggered potential. In one such situation, denoted by the white dot, we note that there is band-touching only for the $\downarrow$ spin, whereas the $\uparrow$ spin is in the gap. The band-structure near the K, K' point is shown in the inset.

Explicit forms of the various hopping amplitudes are given below:

$$J_\sigma = -tJ_0(\alpha) + \frac{4t\sigma\lambda}{3\omega}\sum_{n\neq 0}\beta_n \sin\frac{\pi n}{6} + \frac{t^3}{\omega^2}\left[\sum_{n\neq 0}\gamma_n\left(2\cos\frac{2\pi n}{3}+3\right) + \sum_{m,n\neq 0}\chi_{nm}\left(4\cos\frac{2\pi n}{3}+1\right)\right], \tag{3.22}$$

$$\Lambda^0_\sigma = \frac{\sigma\lambda J_0(\alpha\sqrt{3})}{3\sqrt{3}} - \sum_{n\neq 0}\frac{t^2 J_n^2(\alpha)}{\omega n}\sin\frac{2\pi n}{3}, \tag{3.23}$$

$$L_\sigma = -\frac{4t\sigma\lambda}{3\omega}\sum_{n\neq 0}\beta_n \sin\frac{\pi n}{2} + \frac{2t^3}{\omega^2}\left(\sum_{n\neq 0}\gamma_n\cos\frac{2\pi n}{3} + \sum_{m,n\neq 0}\chi_{nm}\cos\frac{2\pi(m-n)}{3}\right), \tag{3.24}$$

$$M_\sigma = -\frac{2t\sigma\lambda}{3\omega}\sum_{n\neq 0}\beta_n \cos\pi n\,\sin\frac{\pi n}{6} + \frac{t^3}{\omega^2}\left(\sum_{n\neq 0}\gamma_n\cos\frac{2\pi n}{3} + \sum_{m,n\neq 0}\chi_{nm}\cos\frac{2\pi(m+n)}{3}\right), \tag{3.25}$$

$$\Lambda^{A/B} = -\frac{t^2\,(\pm lE_z-\mu)}{\omega^2}\sum_{n\neq 0}\frac{J_n^2(\alpha)}{n^2}\cos\frac{2\pi n}{3}, \quad \tilde{\mu}^{A/B} = \left(1-\frac{3t^2}{\omega^2}\sum_{n\neq 0}\frac{J_n^2(A)}{n^2}\right)(\pm lE_z-\mu), \tag{3.26}$$

where $\beta_n = J_n(\alpha)J_n(\alpha\sqrt{3})/\sqrt{3}n$, $\gamma_n = J_n^2(\alpha)J_0(\alpha)/n^2$ and $\chi_{nm} = J_m(\alpha)J_n(\alpha)J_{m+n}(\alpha)/mn$. We mention here a few important points to be noted. The presence of the SO coupling gives rise to spin-dependent nearest neighbour hopping amplitudes J_σ. Furthermore, the NNNN hopping amplitudes, the L and M terms, also become spin-dependent. The staggered onsite electric field E_z plays an important role in controlling the NNN hopping amplitudes $\Lambda^{A,B}$ but appears only as a second order (in $1/\omega$) contribution. Various amplitudes have been shown in Fig. 3.4, where we note that by controlling a single parameter, α (which controls the strength of the driving term), their strengths can be tuned and can give rise to topological phase transitions.

Next, we proceed to write the Hamiltonian in momentum space by Fourier transforming the B-W effective Hamiltonian, Eq. 3.21. Alternatively, the B-W expansion can also be performed directly in the momentum space, which we have briefly sketched in the Appendix B. In the basis of the sublattices, in the spin sector σ, the B-W Hamiltonian has the form

$$H_{\mathrm{BW}\sigma} = \begin{pmatrix} \delta_{\Lambda\sigma}+\xi_A+\tilde{\mu}^A & \delta_{J\sigma}+\delta_{L\sigma}+\delta_{M\sigma} \\ \delta^*_{J\sigma}+\delta^*_{L\sigma}+\delta^*_{M\sigma} & -\delta_{\Lambda\sigma}+\xi_B+\tilde{\mu}^B \end{pmatrix}, \tag{3.27}$$

where

$$\begin{aligned}
&\delta_{J\sigma} = J_\sigma\left(1+2e^{-i3k_ya_0/2}\cos\left(\sqrt{3}k_xa_0/2\right)\right), \quad \delta_{L\sigma} = L_\sigma\left(e^{-3ik_ya_0}+2\cos\left(\sqrt{3}k_xa_0\right)\right)\\
&\delta_{M\sigma} = 2M_\sigma\left(e^{-i3k_ya_0/2}\cos\left(3\sqrt{3}k_xa_0/2\right)+e^{-3ik_ya_0}\cos\left(\sqrt{3}k_xa_0\right)+e^{3ik_ya_0/2}\cos\left(\sqrt{3}k_xa_0/2\right)\right)\\
&\delta_{\Lambda\sigma} = -4\Lambda^0_\sigma\sin\left(\sqrt{3}k_xa_0/2\right)\left(\cos\left(\sqrt{3}k_xa_0/2\right)-\cos\left(3k_ya_0/2\right)\right)\\
\text{and}\quad &\xi_{A/B} = 2\Lambda^{A/B}\left(\cos\left(\sqrt{3}k_xa_0\right)+2\cos\left(\sqrt{3}k_xa_0/2\right)\cos\left(3k_ya_0/2\right)\right).
\end{aligned} \tag{3.28}$$

This gives the energy eigenvalues

$$E_\sigma^{\rm BW} = \frac{\xi_A + \xi_B + \tilde{\mu}^A + \tilde{\mu}^B}{2} \pm \sqrt{|\delta_{J\sigma} + \delta_{L\sigma} + \delta_{M\sigma}|^2 + \left(\delta_{\Lambda\sigma} + \frac{\xi_A - \xi_B + \tilde{\mu}^A - \tilde{\mu}^B}{2}\right)^2}.$$

For an undoped system, $\mu = 0$, $\xi_A|_{\mu=0} = -\xi_B|_{\mu=0} = \xi$ and $\tilde{\mu}^A\big|_{\mu=0} = -\tilde{\mu}^B\big|_{\mu=0} = \mu_0$. Using this, the above expression reduces to

$$E_\sigma^{\rm BW}\big|_{\mu=0} = \pm\sqrt{|\delta_{J\sigma} + \delta_{L\sigma} + \delta_{M\sigma}|^2 + (\xi + \delta_{\Lambda\sigma} + \mu_0)^2}.$$

$\xi + \delta_{\Lambda\sigma} + \mu_0$ is the effective staggered potential and a finite μ simply shifts the energies. The various amplitudes appearing in the energy expression vanishes at various high-symmetry points in the Brillouin zone, as shown in Fig. 3.5. As, at the K, K' points, the parameters $\delta_{J\sigma}, \delta_L, \delta_M = 0$, $\delta_{\Lambda\sigma} = \pm 3\sqrt{3}\Lambda_\sigma^0$ and $\xi = -3\Lambda^A$, the condition for a band touching point is

$$\begin{aligned} & \xi + \delta_{\Lambda\sigma} + \mu_0 = 0, \\ \Rightarrow \quad & \mu_0 = \mp 3\sqrt{3}\Lambda_\sigma^0 + 3\Lambda^A. \end{aligned} \tag{3.29}$$

Real solutions of ω from this (quadratic) equation provides the band-touching frequencies at K/K' points. At the Γ point, $\delta_{\Lambda\sigma} = 0$, $\xi = 6\Lambda^A$ and $\delta_{J\sigma} + \delta_L + \delta_M = 3(L_\sigma + 2M_\sigma + J_\sigma)$. So, here the condition for band-touching is to simultaneously satisfy

$$\mu_0 = -6\Lambda^A \ \text{ and } L_\sigma + 2M_\sigma + J_\sigma = 0. \tag{3.30}$$

Finally, for the various M points, $\delta_{\Lambda\sigma} = 0$, $\xi = -2\Lambda^A$ and $\delta_{J\sigma} + \delta_L + \delta_M = \pm(J_\sigma - 3L_\sigma + 2M_\sigma)$. So, for a band touching at any of the M points, the condition is to simultaneously satisfy

$$\mu_0 = 2\Lambda^A \ \text{ and } (J_\sigma - 3L_\sigma + 2M_\sigma) = 0. \tag{3.31}$$

With appropriate limit Eq. 3.31 and Eq. 3.30 recovers the results quoted in Ref. [47]. A final comment is to note that as $J_\sigma, L_\sigma, M_\sigma, \Lambda_\sigma^0$ differ between the two spin sectors in the presence of the SO coupling, it is generally not possible to have the bands touching at any of these high-symmetry points for both the up and down spins simultaneously.

To obtain the low energy effective Hamiltonian, we first need to identify the band-touching points in momentum space. In general, finding the band-touching points is not easy, because the various terms in the effective Hamiltonian are only known as a power series in the photon coupling strength. It is possible, however, to expand the Hamiltonian about a generic Dirac point, (which need not be one of the symmetric points in the Brillouin zone) which would be useful if we could find the band-touching points. In this section we will assume that the gap closes at the K and K' points in the Brillouin zone, and write down the effective Hamiltonian, so that we can compare it with the Hamiltonian to $O(\omega^{-1})$ in the high frequency limit, obtained by Ezawa[97], who made this assumption. In the basis of the two sub-lattices, as can be seen from Eq. (3.27), around the K and K' points, the effective Hamiltonian reduces to

$$H_{\rm BW}|_{\mathbf{k}=K/K'} \approx \mathcal{T}_\sigma\left(\eta q_x \tau_x + q_y \tau_y\right) + \mathcal{D}_\sigma^\eta \tau_z - \mu\mathcal{R}I, \tag{3.32}$$

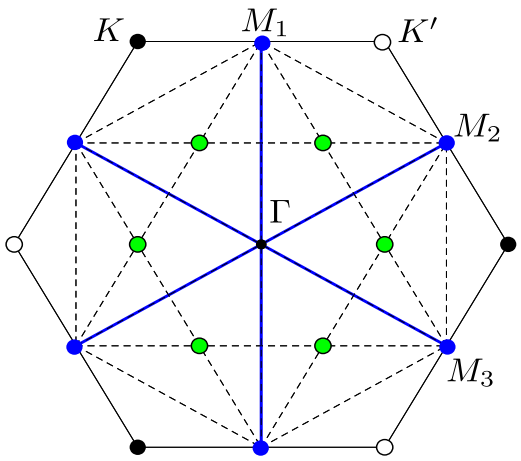

Figure 3.5: The various amplitudes in Eq. (3.28) vanish at high-symmetry points in the hexagonal Brillouin zone. The $\delta_{\Lambda\sigma}$ term vanishes at lines (blue) joining the various M points. All three $\delta_{J\sigma}, \delta_{L\sigma}, \delta_{M\sigma}$ terms vanish at K and K' points, whereas $\delta_{L\sigma}$ additionally vanishes at six other high symmetry points in the Brillouin zone, as noted by the green dots.

with

$$\mathcal{T}_\sigma = \frac{3a_0}{2}\left(2L_\sigma - J_\sigma + M_\sigma\right)$$
$$\mathcal{R} = 1 + \frac{3t^2}{\omega^2}\sum_{n\neq 0}\frac{J_n^2(A)}{n^2}\left(\cos\frac{2\pi n}{3} - 1\right)$$
$$\mathcal{D}_\sigma^\eta = \left(lE_z\mathcal{R} + 3\sqrt{3}\eta\Lambda_\sigma^0\right),$$

$\eta = \pm 1$ for expansions around K and K' points respectively and τ_i are the Pauli matrices in the sub-lattice space. We note that the contributions from L and M paths, making the NN hopping spin-dependent was absent in Ref. [97], where the effect of the time dependent vector potential was taken into account by Peierls substitution only in the NN hopping amplitude but not in the SO coupling. Although these contributions should be negligible in the case of silicene, it may not be small for other compounds with larger SO coupling and also for cold atom systems where the value of the SO coupling is arbitrary. We compute the eigenvalues of the Hamiltonian in Eq. (3.32) by squaring it, and find

$$E_\eta(q,\sigma) = -\mu\mathcal{R} \pm \sqrt{\mathcal{T}_\sigma^2(q_x^2+q_y^2) + \mathcal{D}_\sigma^{\eta 2}}. \tag{3.33}$$

This gives the gap at the K/K' point as $2\mathcal{D}_\sigma^\pm$ for spin sector σ. The condition for the vanishing of the gap is the equivalent of the condition given in Eq. (3.29) (without taking the low energy limit). The change in sign of the gap $\mathcal{D}_\sigma^\pm$ as a function of a parameter signals a topological transition, which is characterized by the change in the spin Chern number C_σ of ± 1. The gap function at low energies was earlier computed by Ezawa[97]. Our results agree at low values of the strength of the electromagnetic field since the work by Ezawa[97] also approximates the value of the Bessel function $J_0(A)$ by its leading quadratic dependence on the strength of the electromagnetic field.

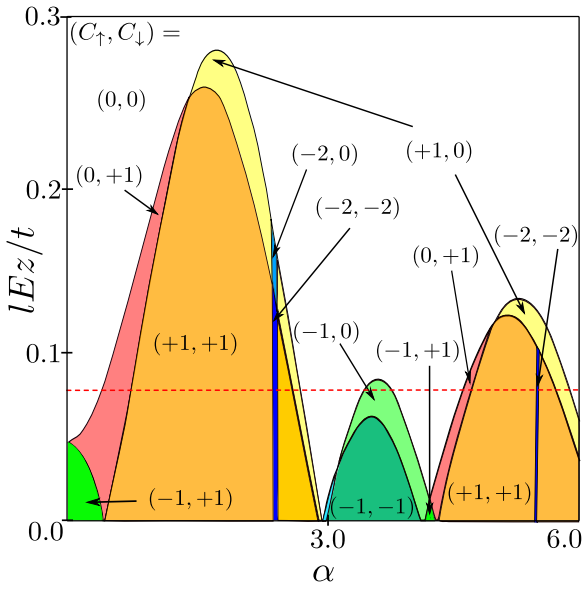

Figure 3.6: The phase diagram of the effective B-W Hamiltonian, Eq. (3.21) characterized by the spin Chern numbers $(C_\uparrow, C_\downarrow)$. Chern numbers along the dashed (red) line is shown in Fig. 3.4. We have taken a small but arbitrary spin orbit coupling constant $\lambda = 0.05t$ and $\omega = 10t$. We use the standard method for Chern number computation, c.f, Ref. [118].

3.4 Numerical Results

Although, in general time-periodic systems possess a much richer topological classification than static systems [30], the B-W Hamiltonian Eq. (3.21) is an effective static Hamiltonian and allows us to study the model in terms of the standard topological classification of time independent systems. Neither Eq. (3.17) nor Eq. (3.21) mixes the two spin sectors, so the spin Chern numbers C_σ, (independent for each spin), can classify the topology of the system. For Eq. (3.17), which is valid in the absence of any time-dependent perturbation, time-reversal (TR) symmetry is intact, and we expect to have the total Chern number of the ground state $C = C_\uparrow + C_\downarrow = 0$. This is not necessarily true for the case of the B-W Hamiltonian in Eq. (3.21), as the polarization of the time dependent field breaks the TR symmetry explicitly.

First, we compute the phase diagram of the static B-W Hamiltonian, and the results are shown in Fig 3.6 and 3.7. A phase diagram similar to that in Fig 3.6, but only for a much smaller range of parameters (both for the strength of the electromagnetic field or light and the applied electric field E_z) was obtained in Ref. [97]. The TR symmetric phase, *i.e.*, when $C = C_\uparrow + C_\downarrow = 0$ is present only when both the TR breaking vector potential of the drive or the staggered potentials are small. In most of the phase-space, $C_\uparrow = C_\downarrow$ instead. In relatively small regions of the phase-space, it is possible to have $|C_\uparrow| \neq |C_\downarrow|$ and at the boundaries of these regions, the gap closes for only one variant of the spin. Now, if the Fermi energy is in the gap of the other spin band, low energy excitations become completely spin-filtered. The size of such regions depend on the strength of the spin-orbit coupling. One such case is shown in Fig. 3.4.

To compare the Chern numbers obtained from the B-W expansion with the Chern numbers of the time dependent system, one critical issue is that the occupations of the *quasienergy levels* (defined below) are generally not known. Our approach is similar to that of Ref. [30], and we compute the Chern number of the quasienergy band below the quasienergy $\epsilon = 0$ which can also be defined in terms

of the winding numbers of the time evolution operator above and below the band. For a time-periodic system on a lattice, the quasienergies $\epsilon_n(\mathbf{k})$ of band n satisfy the Schrödinger equation for the Floquet Hamiltonian,

$$H_F(\mathbf{k},\tau)|u_n(\mathbf{k},\tau)\rangle = \epsilon_n(\mathbf{k})|u_n(\mathbf{k},\tau)\rangle, \tag{3.34}$$

where $H_F(\tau) = i\partial_\tau - H(\tau)$, $\mathbf{k}$ is the Bloch momentum and the *Floquet states* $|u_n(\mathbf{k},\tau)\rangle$ are time-periodic functions with the same period as that of $H(\tau)$. Numerically, the eigenstates of the time evolution operator $U(T) = \mathcal{T}\exp[-i\int_0^T H(\tau)d\tau]$ ($\mathcal{T}$ represents time-ordered product and $T = 2\pi/\omega$) provides the Floquet states $|u_n(\mathbf{k},0)\rangle$. As these Floquet states are defined in the Brilloiun zone, one can compute (using the standard technique[118]) the Chern number for each band. Finally we compare the Chern number of the up-spin sector obtained from the time-dependent Hamiltonian with that of the effective B-W Hamiltonian in Fig. 3.7, where the boundaries obtained from the time-dependent Hamiltonian have been shown by dotted lines. Note that the B-W results are given both for up-spin and down-spin, whereas to avoid cluttering the diagram, the exact results are given only for the up-spin sector. Generally, in the large frequency regime, we expect to have excellent agreement as, in fact, is seen in the figure. Note that for silicene, the spin-orbit coupling is one order of magnitude smaller than that shown in the figures, and hence the region of splitting between the up and down spins will be extremely narrow and not visible at the scales shown. For germanene and stanene, the order of magnitude of the spin-orbit coupling is almost the same as that used in the figure, and so the phase diagram for both of them will be quite similar to the one shown here. As mentioned earlier, a time-periodic system possesses a richer topological structure than its static counterpart [30]. Broadly speaking, the Chern number of our time-periodic system can be written as $C = C_0 - C_\pi$, where C_0 and C_π are the number of chiral edge states (with the $\pm$ signs for opposite chiralities) at the quasi-energy $\epsilon = 0$ and $\omega/2$ respectively [86]. Starting from larger frequencies and reducing it, once the frequency becomes equal to the band-width, direct transitions from the bottom of one band to the top of the next band can occur, giving rise to band foldings. This may lead to band crossings in the extended quasi-energy zone resulting in non-zero C_π [86]. So we expect, as long as ω is larger than the band-width, an effective Hamiltonian that is obtained by using a high-frequency expansion such as the B-W expansion, should reproduce the Chern number correctly. What is further interesting is that with increasing driving amplitude A, the electrons lose their kinetic energy (J_σ, Eq. (3.22)), resulting in a shrinking of the band-width. This, in turn, results in a larger range of frequency where the B-W Hamiltonian can reliably predict the Chern number. This is shown in Fig. 3.7, where we see that at low values of the amplitude of the light, the B-W expansion breaks down at $6t$, which is the band-width. But with increasing amplitude of light, the regime of validity of the B-W Hamiltonian in Fig. 3.7 increases.

Further, even if the B-W expansion does not break down at smaller frequencies, the higher order contributions of the expansion may no longer be negligible. Such situations, where the effective Hamiltonian fails to predict the correct Chern numbers occurs with smaller values of ω/t. In the Fig. 3.7, such discrepancies occur only a very small region (red line) and extends below $\omega/t < 2$.

3.5 Conclusion

In summary, we have discussed a high-frequency effective Hamiltonian, using the Brillouin-Wigner expansion method, to describe periodically driven honeycomb lattice systems with spin-orbit coupling and staggered potentials. Our effective Hamiltonian successfully predicts the topological nature of the system for a wide range of parameters and also provides the opportunity to explore non-trivial topological phases with external controls.

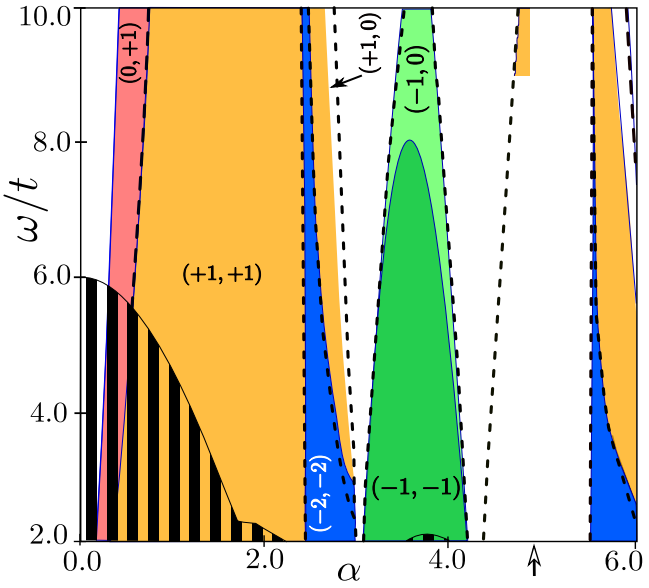

Figure 3.7: The phase diagram of the effective B-W Hamiltonian for both up and down spins, Eq. (3.21), with the frequency of the drive ω and the strength of the drive α. In the shadowed region, when the band width of the effective Hamiltonian becomes bigger than the driving frequency, the Chern number fails to match with the exact computation discussed in the text. We do not show other phases that appear in this shadowed region for the exact computation. We compare the phase boundaries of the up-spin sector of the B-W Hamiltonian with those from the exact numerical results (indicated by dashed lines) and see that they match exactly at high frequencies. In other regions, even for comparatively small ω/t up to 2, the match is still excellent. In the red region near $\alpha \approx 5.0$ (marked along the axis), the Chern number fails to match with exact computation, which is generally true for smaller ω/t as higher order expansion becomes necessary. Other phases are similar to that in Fig. 3.6.

Although the B-W and other similar high-frequency expansions provide effective time-independent Hamiltonians of the time periodic system, that does not necessarily mean that they can capture and predict correct physical properties. The time-periodic system is inherently a non-equilibrium system and in general possesses no ground state. The lack of clarity of the occupation statistics of the electrons remain a critical issue to be resolved in such systems [101, 98, 99], which in turn may limit predictions of transport properties. Preparing such non-equilibrium *Floquet ground state* [100, 102] and predicting their transport properties are also being intensely investigated. If the driving frequency is much larger than the band width, then the energy absorption in the system is likely to be negligible [103, 104, 48, 105], and in this limit the system might be represented as being in quasi-equilibrium, at least for a finite time [106]. In this case, it can be described by an effective Hamiltonian such as the B-W Hamiltonian. Nevertheless, it may be interesting to see how well the transport properties as computed from a B-W Hamiltonian compares with the other methods of computing non-equilibrium transport of the time-dependent system. We hope to return to such studies in the future.

Chapter 4

Bulk-Edge Correspondence for Periodically Driven Systems

4.1 The low frequency analysis

This chapter aims to study the periodically driven systems when these are exposed to the radiation of frequency less than the bandwidth of the system. We have discussed the high frequency analysis where we performed the systematic Brillouin-Wigner expansion of the Hamiltonian to second order in the inverse of the frequency, not only in silicene, but in other spin-orbit coupled materials [107, 47]. But, as was discussed in the last chapter, the BW expansion breaks down when the frequency ω becomes smaller than the band-width of the effective Hamiltonian. The real constraint on the applicability of the BW expansion is a combined bound on both ω and the amplitude of driving and in fact, the validity of BW increases, even for lower frequencies when the amplitude increases. However, the physical reason for the breakdown of the earlier studies at low frequencies is because, at frequencies comparable to the band-width, it is no longer possible to neglect the topology of the *quasienergy* space, which forms a periodic structure with the single valuedness of the eigenfunction requiring the quasienergies to be within a "Floquet zone". Low frequency driving can lead to crossings between the bottom of one Floquet band and the top of the next Floquet band. These crossings are neglected in the BW expansion and hence, the study of the driving at low frequencies requires a new formalism which goes beyond the effective static approximation of a dynamical Hamiltonian.

Such a formalism has been studied[30] recently, where it was shown that although the Floquet spectrum can be organised into quasi-energy bands, and the Chern numbers of these bands can be computed, just this one number was not sufficient to classify the system completely and to predict the edge spectrum. It was shown instead, that the Chern number of the band which is computed by integrating the Berry curvature over the whole Brillouin zone is actually the difference between the number of chiral edge modes leaving the band from above and those entering the band from below. Since in a static system, the spectrum is bounded from below, the edge states entering the band were always zero; hence, the Chern number of the band was sufficient to determine the edge spectrum. But for Floquet systems, this is no longer true and it is possible to have edge states even when the Chern number of the band is zero. So to really characterise the edge states, one needs to have access to full time-dependent bulk evolution operator U(t), evaluated for all intermediate times within the driving period[30]. The invariant thus computed predicts the complete Floquet edge-state spectrum.

It was shown that the number of the edge states, counted with a sign corresponding to their chirality, is related to the winding number of the bulk time evolution operator and it was also shown

that the difference in the winding numbers at two different energies was precisely equal to the sum of all the Chern numbers that lie between these energies. More specifically, for a two band model with the Fermi energy at zero quasi-energy, it was shown that the gaps at zero quasi-energy and at the zone boundary $\omega/2$ gave rise to winding numbers C_0 and C_π, whose difference gave the Chern number of the band. In other words, a Floquet topological insulator is characterized by two integers, in contrast to the single Chern number for static topological insulators.

While this formalism is, of course, applicable both in the high frequency as well as the low frequency regime, at high frequencies, since the frequency is much larger than the band-width, the zone boundary is not accessible. Hence, in the high frequency limit, computation of the Chern numbers at zero quasi-energy is sufficient to characterize all the phases.

However, in most cases, the high frequency, strong amplitude limit needed for obtaining new topological phases is currently experimentally unattainable and in recent times, the focus on low frequencies has increased. Early work in this area focussed on graphene [108, 109, 110, 111] and showed not only the existence of several new phases and resulting chiral edge modes, but also how disorder could enhance conductance by several orders of magnitude. Broad dips in the conductance at resonances between valence and conduction bands in graphene nano-ribbons have been predicted [112] and more recently studied [113] in detail. New states with optically induced changes of sub-lattice mixing have been identified [114]. Quantum resonances have been studied in irradiated graphene *n-p-n* junctions [115]. The role of the symmetries of the instantaneous Hamiltonian and the time-evolution operator in determining the phase diagram at ultra-low frequencies in irradiated graphene using the adiabatic impulse method has also been recently emphasized [116]. More recently, universal fluctuations of the topological invariants have also been studied [117].

Here, we will compute the Chern numbers of a silicene [1] band, both at zero quasi-energy and at the zone boundary, and for both spin up and spin down electrons, since the up-down symmetry is broken in the presence of spin-orbit coupling. We will work in the low frequency regime, where the static approximation does not hold; however, it is still possible to reliably compute Chern numbers using numerical methods. We will show explicitly that the bulk-boundary correspondence holds, by checking that the C_0^σ and C_π^σ as obtained by counting the number of edge states at the right and left edges of the sample, agrees with the Chern number of the bulk obtained from $C_\pi^\sigma - C_0^\sigma$.

4.2 Computation of dynamical band structure

We start with two dimensional Dirac systems which are buckled due to the large ionic radius of the silicon atoms and consequently have a non-coplanar structure unlike graphene. These materials can be described by a four-band tight binding model in a hexagonal lattice given by

$$H = -t \sum_{\langle i,j\rangle,\sigma} c_{i\sigma}^\dagger c_{j\sigma} + \frac{i\lambda}{3\sqrt{3}} \sum_{\langle\langle i,j\rangle\rangle,\sigma} \sigma \nu_{i,j} c_{i\sigma}^\dagger c_{j\sigma} + lE_z \sum_{i\sigma} \xi_i c_{i\sigma}^\dagger c_{i\sigma} \ . \tag{4.1}$$

Here, the first term is the kinetic term where t is the hopping parameter. The second term represents the spin-orbit coupling term where the value of λ depends on the material and $\nu_{i,j} = \pm 1$ depending on whether the next-nearest neighbour hopping is clock-wise or anti-clock-wise. The last term represents the staggered sub-lattice potential due to the buckling. When a beam of circularly polarised light is incident on the sheet, the corresponding electro-magnetic potential $\mathbf{A} = (A_0 \cos(\omega\tau), A_0 \sin(\omega\tau), 0)$ is

[1] We will generically use the name silicene to denote materials with non-zero spin-orbit coupling and buckling.

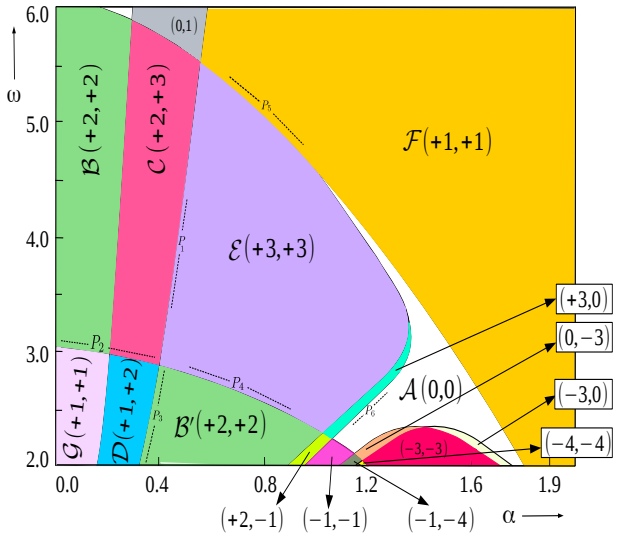

Figure 4.1: The phase diagram for the model Hamiltonian in Eq. 4.1 as we vary the amplitude α and the drive frequency ω, with the external electric field fixed at $lE_z = 0.08t$. Each phase is characterized by the spin resolved quantum numbers $(C_\uparrow, C_\downarrow)$. We label the phases by calligraphic letters. The dotted lines P_i indicate the topological phase boundaries, inferred from the gap closing in momentum space, shown only for the $\uparrow$ spin sector.

introduced into the Hamiltonian using Peierls substitution. ω is the frequency of light and A_0 is its amplitude. In the Fourier transformed space, this is written as

$$H(\tau) = \begin{pmatrix} lE_z - \delta_\lambda & \delta_t & 0 & 0 \\ \delta_t^* & -lE_z + \delta_\lambda & 0 & 0 \\ 0 & 0 & lE_z + \delta_\lambda & \delta_t \\ 0 & 0 & \delta_t^* & -lE_z - \delta_\lambda \end{pmatrix} \tag{4.2}$$

where

$$\delta_\lambda(\tau) = \frac{2\lambda}{3\sqrt{3}} \left[\sqrt{3}a_0 \sin\tilde{k}_x - \sin\left(\frac{\sqrt{3}a_0}{2}\tilde{k}_x + \frac{3a_0}{2}\tilde{k}_y\right) - \sin\left(\frac{\sqrt{3}a_0}{2}\tilde{k}_x - \frac{3a_0}{2}\tilde{k}_y\right)\right] \tag{4.3}$$

with $\tilde{k}_x = k_x + A\cos\omega\tau$ and $\tilde{k}_y = k_y + A\sin\omega\tau$ and

$$\begin{aligned} \delta_t(\tau) = t\,[&\exp(-i\alpha\sin\omega\tau) \\ &+T_+\exp\frac{i\alpha(\sqrt{3}\cos\omega\tau + \sin\omega\tau)}{2} \\ &+T_-\exp\frac{i\alpha(-\sqrt{3}\cos\omega\tau + \sin\omega\tau)}{2}\Bigg] \end{aligned} \tag{4.4}$$

with $T_\pm = \exp(ia_0(\pm\sqrt{3}k_x + 3k_y/2))$. Here, we have defined $\alpha = Aa_0$, where a_0 is the lattice constant.

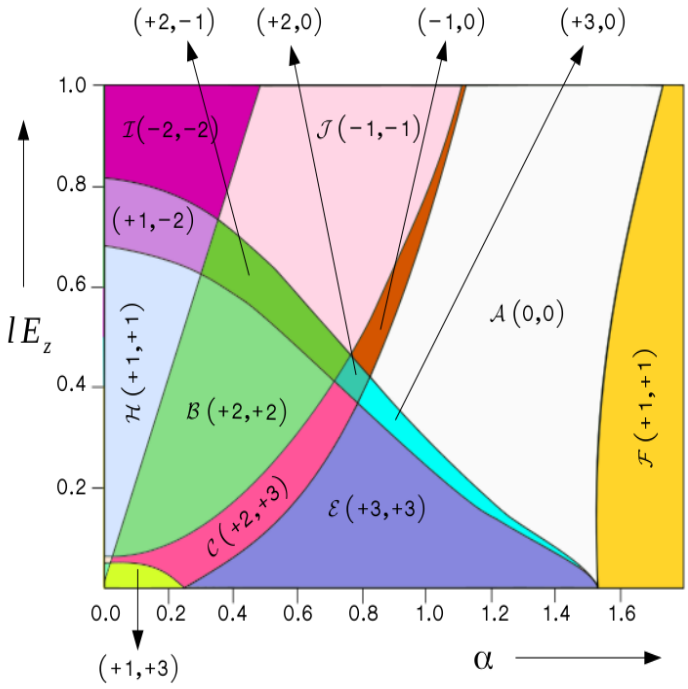

Figure 4.2: The phase diagram as a function of the amplitude α and the external electric field lE_z. A low drive frequency is chosen ($\omega = 3.0t$) since we wish to study the system in the low frequency limit. All the phases are the same as those found in Fig.4.1 except for three new phases - $\mathcal{H}$, $\mathcal{I}$ and $\mathcal{J}$. The labelling of the phases follows the same convention as in Fig. 4.1.

For the bulk system, the vector potential and hence the Hamiltonian is periodic in both the x and y directions. This implies that we can rewrite the Hamiltonian in terms of a Floquet eigenvalue problem with the Hamiltonian given by

$$H_F = -i\frac{\partial}{\partial\tau} + H(\tau), \tag{4.5}$$

the eigen functions given by

$$\psi_{\mathbf{k},b}(x,y,\tau) = u_b(k_x,k_y,\tau)e^{i\mathbf{r}\cdot\mathbf{k}-i\epsilon_b\tau} \tag{4.6}$$

with $u_b(k_x,k_y,\tau) = u_b(k_x,k_y,\tau+2\pi/\omega)$, and where ϵ_b are the quasienergies or the eigenvalues of H_F. The Hamiltonian can now be solved numerically as a function of the amplitude A_0, frequency ω and the sub-lattice potential E_z, both for the quasienergy eigenvalues and for the wave-functions.

At high frequencies, ω constitutes a large gap between unperturbed subspaces, and the extended Floquet Hilbert space splits into decoupled subspaces with different photon numbers. Since the perturbation scale of the Hamiltonian, which is the band-width t, is much smaller than ω, one can use systematic perturbation theory to include virtual processes of emitting and absorbing photons, and upto a given order in perturbation theory, one can obtain an effectively static Hamiltonian as shown in Ref. [107]. The Chern numbers for the model can then be computed by integrating the Berry curvature over the whole Brillouin zone [118] using the eigenvectors of the effective Hamiltonian. However it is expected that such an expansion in $1/\omega$ would fail to predict the correct Chern numbers once the frequency of the drive, ω, becomes comparable to the bandwidth. This is the part of the phase diagram that we shall complete in this paper.

4.3 The phase diagram of the Floquet Hamiltonian

As the frequency of the drive becomes comparable to the effective bandwidth of the system, it is essential to now consider the complete nature of the quasi-energy bands in the computation of the topological invariants of the system. As was mentioned in the introduction, the quasi-energy bands (of the two band system) are now identified with two topological invariants, C_0 and C_π and the net Chern number of a band is given by $C = C_0 - C_\pi$ (independently for each of the spins).

The Fourier-transformed time-dependent Hamiltonian (Eq. 2) is block-diagonal in the spin space. For either the $\uparrow$ or the $\downarrow$ spin, it is a 2×2 Hermitian matrix which encodes the bulk properties of the system. The time evolution operator at stroboscopic times can then be written as

$$U(\mathbf{k}, 2\pi/\omega) = \mathcal{T} e^{-i \int_0^{2\pi/\omega} H(\mathbf{k},\tau) d\tau}. \tag{4.7}$$

and the Floquet states $u_b(k_x, k_y, 0)$ are the eigenstates of this operator. The Chern number of each Floquet band is then defined by integrating the Berry curvature of the Floquet states over the whole Brillouin zone -

$$C = \frac{1}{2\pi} \int_{BZ} dk_x dk_y (\nabla \times \mathcal{A}_{\text{lower}}(\mathbf{k})), \tag{4.8}$$

where $\mathcal{A}_{\text{lower}}$ is the Berry connection in terms of Floquet states of the quasi-energy band with quasienergy lying between $(-\omega/2,\ 0)$. We numerically compute the Chern numbers of the lower band (of both $\uparrow$ and $\downarrow$ spins) following the work by Fukui et al [118].

When the parameter ranges are such that a high frequency approximation would be valid, the Chern number computed using the effective static Hamiltonian would exactly match the one obtained by considering the Floquet states. In this sense, the following phase diagram that we present complements what has been obtained earlier in Ref. [107], and completely specifies the topological phases of the system for all parameter regimes.

The phase diagrams for both the up spin and the down spin bands are presented in Figs. 4.1 and 4.2. In Fig. 1, we show the Chern number of the lower quasienergy band as a function of the amplitude of the drive versus the frequency, whereas in Fig. 2 we show it as a function of the amplitude of the drive versus the sub-lattice potential. For lower frequencies, many different phases appear and appear to follow a fractal structure, as was seen for graphene in Ref.[119]. But as such phases are not expected to be protected by a large enough band-gap, we have only shown phases which are 'large enough' (occupy enough area in the phase diagram) and we have ignored tinier phases. As $\alpha \to 2$ and $\omega \to 6$, these phases smoothly go over to the high frequency phases in Ref. [107]. We have also chosen to name only those phases that are large enough to be possible stable phases in calligraphic letters as $\mathcal{A}, \mathcal{B} \ldots \mathcal{J}$, with $\mathcal{A}, \mathcal{B}, \mathcal{C}, \mathcal{E}, \mathcal{F}$ being present in both Figs. 4.1 and 4.2, and $\mathcal{B}', \mathcal{D}, \mathcal{G}$ in Fig.4.1 and $\mathcal{H}, \mathcal{I}, \mathcal{J}$ in Fig. 4.2. Note that there are two phases $\mathcal{B}$ and $\mathcal{B}'$ which have identical values of the Chern numbers for both the $\uparrow$ spin band and the $\downarrow$ spin band. Nevertheless, they are two distinct phases since they occur for different values of ω and α and are not continuously connected to each other and they could have different edge state structures. Note also the existence of a phase $\mathcal{A}$ which has zero Chern numbers for both spin $\uparrow$ and spin $\downarrow$ electrons. We will see later in the next section, that this is a topological phase and has edge states despite having zero Chern numbers.

The lines that separate the phases are when the gap closes and the gap closing typically occurs at the high symmetry points of the Brillouin zone as shown in Fig. 4.3. For the lines P_2, P_4 and P_5, the gap closes at the Γ point whereas for the P_1 and P_3 lines, it closes at the K point and for the P_6 line, the closure happens at the half-way point between the Γ point and the K point. Note that we have concentrated on the spin $\uparrow$ bands and hence have lines separating region $\mathcal{C}$ from $\mathcal{E}$, which have different Chern numbers for $\uparrow$ spin, but no line separating regions $\mathcal{C}$ from $\mathcal{B}$, which have the same

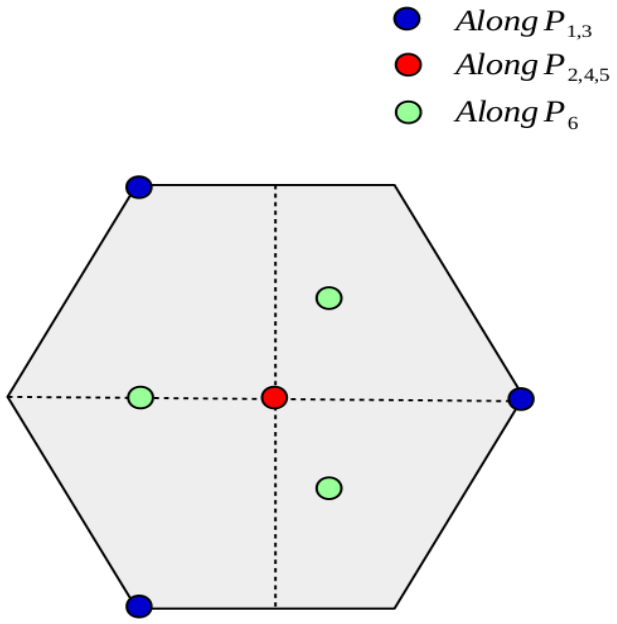

Figure 4.3: Gap closing points in the Brillouin zone along the P_i $(i = 1 \ldots 6)$ phase boundaries (drawn in Fig.1) as described in the caption of Fig.1.

Chern number for $\uparrow$ spin. A similar analysis can be done for the $\downarrow$ spin case.

We note that the Chern number changes by ± 2 at the P_5 crossing, which essentially implies a quadratic touching of the bands. This is similar to the transition explained in Ref. [108] where the Hamiltonian for the first Γ point transition at the Floquet zone boundary was obtained perturbatively, and was shown to lead to a Chern number change of ± 2. This can only happen at the spherically symmetric Γ point. Along P_1, P_2, P_3 and P_4, the change in the Chern number is ± 1 and the band touching happens at the Γ or K points. Along P_6, however, the change in the Chern number is ± 3. This happens at 3 points in the Brillouin zone, symmetric around the Γ point as shown in Fig. 4.3. We have also checked that a change of the chirality of the circularly polarized light, besides changing signs of all the Chern numbers also breaks inversion symmetry with respect to the gap closing diagram in Fig. 4.3. The blue points are at K' instead of K points and the green points are placed so as to complete the smaller hexagon.

However, the computation of the Chern number does not specify the C_0 and C_π invariants individually. As the bulk-boundary correspondence in our system comes from these invariants, to discover these two indices, we need to consider the edge-state structure in a system with edges - *e.g.*, a ribbon geometry. This is what we shall discuss in the next section.

We complete the study of the phase boundaries and their relation to the high symmetry points of the Brillouin zone for down spin also. Below we draw the phase boundaries for down spin and label them by $Q_1, Q_2, ...Q_7$ in the phase diagram shown in Fig.4.5. Next, we show that the gap closing points for the $\downarrow$ spin also occur at one of the high symmetry points of the Brillouin zone Fig.4.6.

4.4 Connection of bulk topology to the boundary

In this section, we study the quasi-energy band-structure of the model in an infinite zigzag nanoribbon geometry, with a finite width. We identify the four integers $C_0^\uparrow, C_0^\downarrow, C_\pi^\uparrow, C_\pi^\downarrow$ (defined later) that

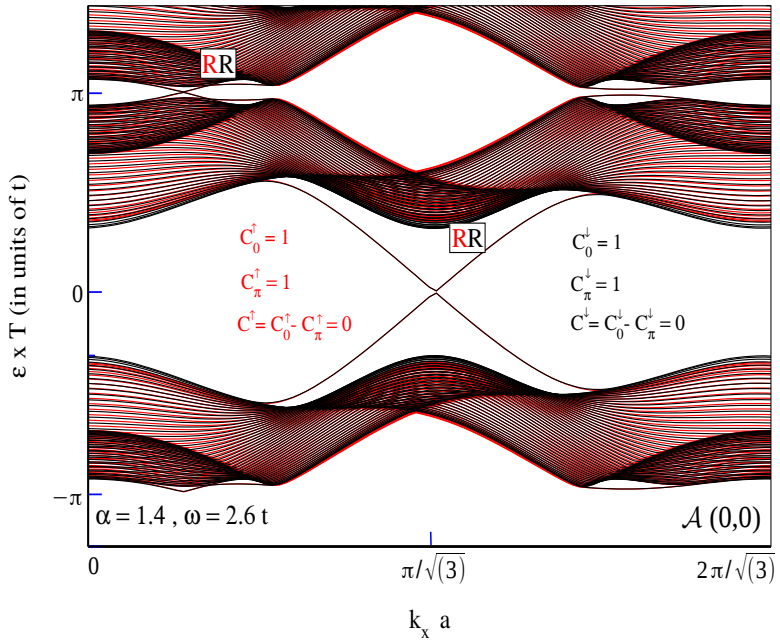

Figure 4.4: The quasi-energy band structure of a zigzag nanoribbon of the periodically driven spin-orbit coupled system for phase $\mathcal{A}$. Both spin sectors, $\uparrow$ and $\downarrow$ (shown in red and black respectively) possess one pair of chiral edge states both at zero quasi energy and Floquet zone boundary. We also label the chirality of the left edge state at the two inequivalent gaps by R or L depending on whether the state is right-moving or left-moving. The system is finite in the y-direction while the x-direction is periodic.

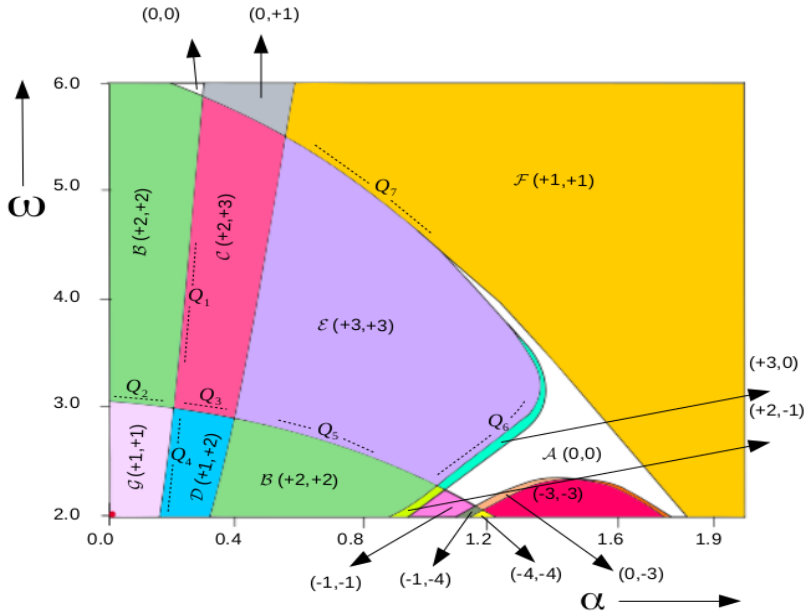

Figure 4.5: Phase diagram for the model Hamiltonian in Eq.4.1 as we vary the amplitude α and the drive frequency ω in the resonant coupling limit, fixing the external electric field at E_z=0.08 t. Each phase is characterised by spin resolved quantum numbers $(C_\uparrow, C_\downarrow)$. We label the phases by calligraphic letters. The dotted lines Q_i indicate the phase boundaries (gap closing points) in momentum space along the topological phase boundaries for the $\downarrow$ spin sector only. A similar analysis for the $\uparrow$ sector has been shown before.

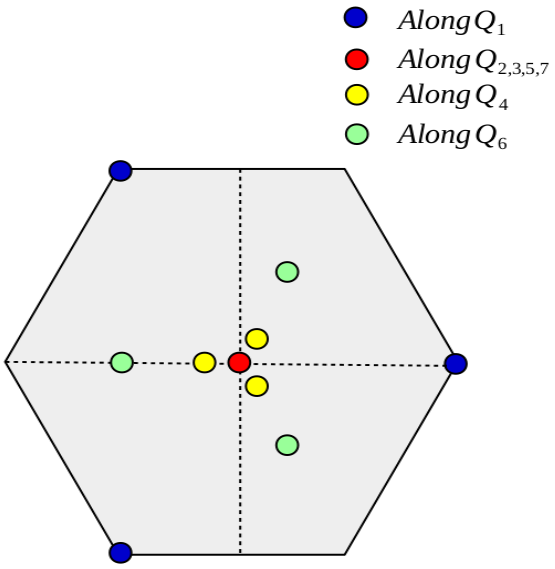

Figure 4.6: Gap closing points in the Brillouin zone along the $Q_i, i = 1 \ldots 6$ phase boundaries (drawn in Fig.1) as described in the caption of Fig.1.

Table 4.1: Spin-resolved topological quantum numbers and the edge states for phases in Figs.4.1, 4.2

Phases	$(C^{\uparrow}, C^{\downarrow})$	$C_0^{\uparrow}$	$C_{\pi}^{\uparrow}$	$C_0^{\downarrow}$	$C_{\pi}^{\downarrow}$
$\mathcal{A}$	(0,0)	1	1	1	1
$\mathcal{B}, \mathcal{B}'$	(+2,+2)	0	-2	0	-2
$\mathcal{C}$	(+2,+3)	0	-2	1	-2
$\mathcal{D}$	(+1,+2)	-1	-2	0	-2
$\mathcal{E}$	(+3,+3)	1	-2	1	-2
$\mathcal{F}$	(+1,+1)	1	0	1	0
$\mathcal{G}$	(+1,+1)	-1	-2	-1	-2
$\mathcal{H}$	(+1,+1)	0	-1	0	-1
$\mathcal{I}$	$(-2,-2)$	0	2	0	2
$\mathcal{J}$	$(-1,-1)$	0	1	0	1

characterize Floquet topological insulators in our model, in each of the phases in Fig. 4.1 and 4.2, by choosing appropriate values of ω, α and lE_z. A representative diagram for the phase $\mathcal{A}$ has been shown in Fig. 4.4 and the remaining diagrams have been relegated to the appendix. The spectrum has been shown slightly beyond the 'first Floquet-Brillouin zone', $-\omega/2 < \epsilon_b < \omega/2$, so that the edge states at the zone boundary are clearly visible.

The first point that we note is the gaps and the edge states at the zone boundaries (at $\epsilon_b = \omega/2 \equiv -\omega/2$). In the high frequency regime studied earlier, we had restricted ourselves to frequencies below the zone boundaries (i.e, at $\epsilon = \pm\omega/2$), and hence the edge states at the zone boundary do not appear. However, in this work, our main focus is on the low frequency regime, and one of our aims is to explicitly check that the Chern number of the band is given by the difference between the number of chiral edge states above and below the band. How do we count the number of chiral edge states? As shown in Ref. [30], the number of edge modes are related to the winding number of the Floquet operator. Unlike the Chern number of a band, which depends only on the stroboscopic dynamics of the Floquet operator, the winding number has information about the circulation direction, which gets related to the direction of propagation of the edge states. In a Floquet system, the chirality at a given edge depends on details of the driving and can be either positive or negative, independent of the chirality of the driving force[120]. The chirality of the driving force only provides the required time-reversal breaking. However, at low frequencies, there is no direct relation between the chirality of the drive and the chirality of the edge states, since the drive can lead to multiple gap closings and openings with multiple edge states. Hence, the edge state chirality needs to be explicitly computed for each phase.

Let us now focus on the Floquet band structure in the various different phases. For illustration, let us confine ourselves to the spin up band. Let us also confine our attention to the left edge (L). The determination of the chirality of the edge state as shown on the graph is made by actually checking whether the right-moving state (positive slope) is at the left edge or at the right edge and similarly whether the left-moving slope (negative slope) is at the left or right edge. This can be done explicitly since we have numerically obtained all the wave-functions. We can now easily count the number of chiral edge states at the band-gap at zero, and at the band gap at $\omega/2$, in the various plots in the panels in Fig. 4.4 and in the appendix. We choose a convention where a right-moving (positive slope in the energy versus momentum plot) at the left L edge state is assigned a winding number or chirality -1 and a left moving (negative slope) state is assigned a chirality $+1$. We then compute C_0^{σ} by taking it to be $-1/+1$ depending on whether the L state (or states) in the band-gap at zero frequency is

right-moving or left-moving and adding up the values. Similarly, in the band-gap at frequency $\omega/2$, we compute C_π^σ by taking $-1/+1$ for each right-moving/left-moving state and adding up the values. For instance, in Fig. 4.3, for the spin-up band, at zero frequency, there is a single edge state at the left edge which has negative slope; thus $C_0^\uparrow = +1$. At the frequency $\omega/2$ also, there is a single edge state at the left edge with negative slope, thus $C_\pi^\uparrow = +1$ as well. The Chern number of the $\uparrow$ band in phase (A) was computed earlier to be $C^\uparrow = 1$ which precisely agrees with $C_0^\uparrow - C_\pi^\uparrow$, as expected from Ref. [30].

Using the same method, C_0^σ and C_π^σ can be computed for each of the phases in Fig. 4.1 and 4.2 and the results are tabulated in Table 1. Note that, as expected, the Chern number of the band, $C^\sigma = C_0^\sigma - C_\pi^\sigma$ in each case. Note also that the phases $\mathcal{A}, \mathcal{B}, \mathcal{C}, \mathcal{E}, \mathcal{F}$ in the table are present in both Figs. 4.1 and 4.2, whereas $\mathcal{B}', \mathcal{D}$ and $\mathcal{G}$ occur only in Fig.4.1 and $\mathcal{H}, \mathcal{I}$ and $\mathcal{J}$ only in Fig. 4.2.

We also compute the Floquet band structure in a zigzag nano ribbon in all the different phases which have been shown in Figs.4.1 and 4.2. The name of the phase, as well as the values of C_0 and C_π are given in the figure itself Fig.4.7. As described above, C_0 and C_π are computed by taking it to be $-1/+1$ depending on whether the L state (or states) in the appropriate band-gap is right-moving or left-moving at the left edge of the sample and adding up the values. We note that the phase $\mathcal{A}$ which has zero Chern number but has two pair of edge states appearing at the Floquet zone boundary and near the zero quasienergy is similar to the anomalous Floquet Anderson insulator studied by Rudner et. al [30].

4.5 Conclusions

In comparison with earlier studies of irradiated graphene, the main difference for spin-orbit coupled materials is the fact that the phase boundaries for the spin $\uparrow$ electrons and the spin $\downarrow$ electrons occur at different points in the parameter space. Besides, due to the buckling, an external electric field can be applied which can tune the masses at the K and K' points . This external tuning parameter helps in finding new phases as seen in Fig. 4.2, which do not exist in graphene.

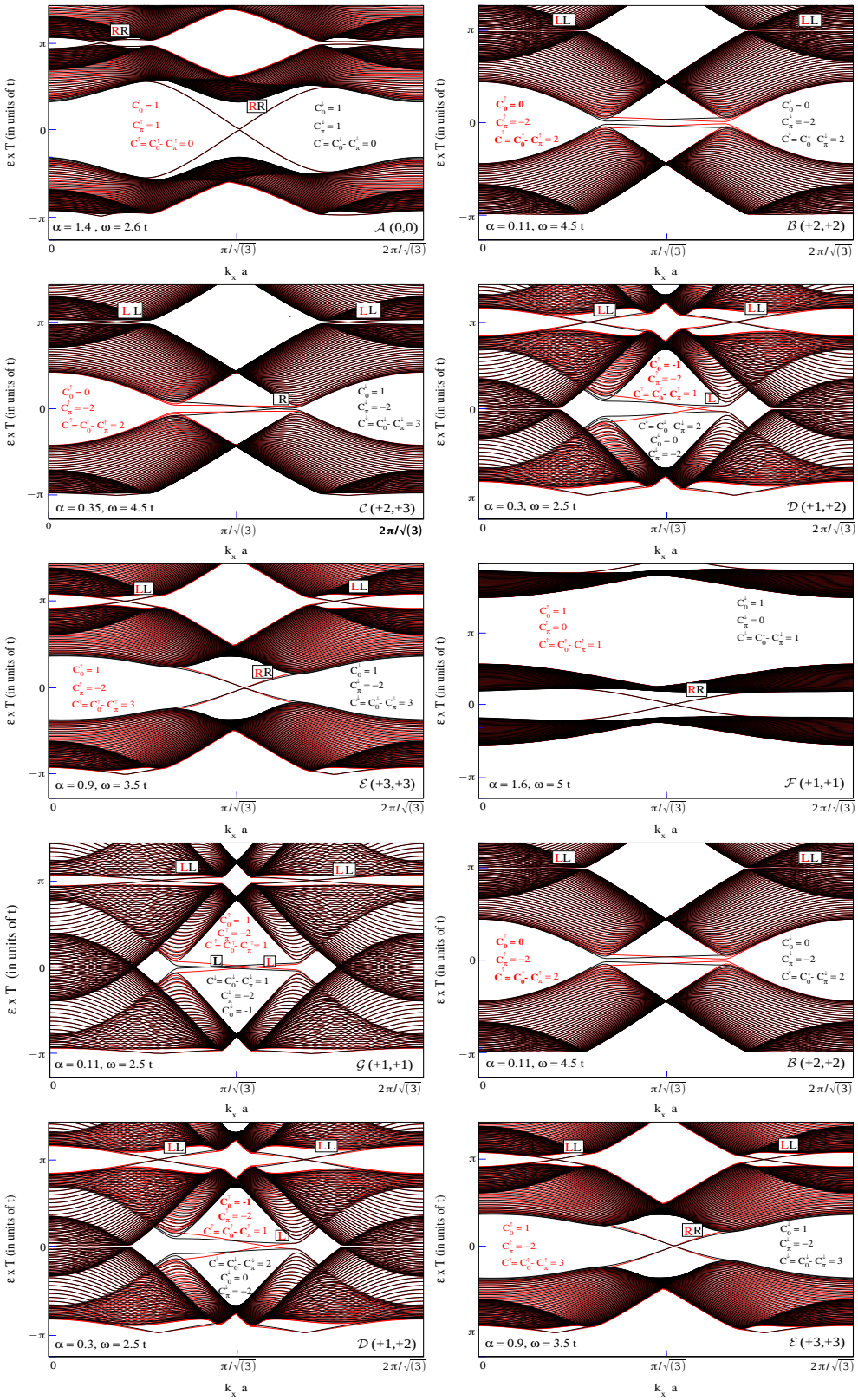

Figure 4.7: The quasi-energy band structure of a zigzag nanoribbon of the periodically driven spin-orbit coupled system for the phases $\mathcal{A}, \mathcal{B}, \mathcal{B}', \mathcal{D}, \mathcal{E}, \mathcal{F}$. The drive parameters, amplitude and frequency for each phase are given in each diagram. Other labelings are same as fig.4.4.

Chapter 5

Summary

In this thesis, we have mainly studied the effect of including spin-orbit coupling in Dirac materials. This is applicable to materials such as silicene, germanene and stanene. An understanding of the role of spin-orbit coupling is crucial, for applications in the field of spintronics, where the spin, rather than the charge of the electron is utilised. Current research in the field focuses on manipulating the band structure of materials such a graphene, as well as spin-orbit coupled materials like silicene, so that they can be used for spintronic applications.

In this context, we have studied silicene junctions, where part of the material is polarised by coupling it via the proximity effect to a ferromagnet. In particular, we have studied a ferromagnet-normal material-ferromagnet junction. In this geometry, we have obtained spin and valley polarisations in terms of the independent conductances of the different spins at the two valleys and the band structure of ferromagnetic silicene, and saw how one could obtain pure valley or spin polarisation by modulating the external electric field. The spin-orbit coupling was crucial to get this result, which does not occur in graphene. We also investigated the oscillatory behaviour of the transverse magneto-resistence (TMR) with respect to the strength of both spin independent and spin-dependent barrier potentials and showed how the TMR can even change sign as a function of the external electric field.

We have also studied the effect of shining light on spin-orbit coupled materials. Similar to earlier work on graphene, we showed that the parameters of the Hamiltonian and the band structure are affected by driving the system by shining circularly polarised light. Using a perturbation expansion known as the Brillouin-Wigner expansion, we computed the effective Hamiltonian in the zero-photon subspace not only to order $\mathrm{O}(\omega^{-1})$ but by keeping all the important terms to order $\mathrm{O}(\omega^{-2})$ and obtained the photo assisted correction terms to both the hopping and the spin-orbit terms, as well as longer-ranged hopping terms. We then used the effective static Hamiltonian to compute the phase diagram in the high-frequency limit and compared it with the results of direct numerical computation of the Chern numbers of the Floquet bands and showed that at sufficiently large frequencies, the B-W theory high-frequency expansion worked well even in the presence of spin-orbit-coupling terms. We also investigated topological phase transitions beyond the high-frequency regime and unearthed many new topological phases. These phases are characterised by the spin-resolved topological invariants, $C_{0\uparrow}, C_{0\downarrow}, C_{\pi\uparrow}$ and $C_{\pi\downarrow}$, which specify the spin-resolved edge states traversing the gaps at zero quasi-energy and the Floquet zone boundaries respectively. We showed that for each phase boundary, and independently for each spin sector, the gap closure in the Brillouin zone occurred at a high symmetry point.

There is an upsurge in the study of proximity induced spin-orbit coupling in graphene which would help to integrate graphene into functional devices. There has been experimental studies on methods like hydrogenation [128], fluorination [129] and heavy adatom adsorption [130]. Our study would be relevant in these systems also. Moreover, we focussed on Dirac materials with spin-orbit

coupling in solild-state systems but, the study can also be extended to two dimensional optical lattices where one can artificially synthesise spin-orbit coupling with a combination of microwave driving and lattice shaking [131] and also to ultra cold atoms [132], in both bosonic [133, 134] and fermionic systems [135, 136] where the Raman coupling has been shown to give rise to an effective spin-orbit interaction. These are a few extensions that we have in mind for the future. Besides this, a more general understanding is required of how systems behave under low frequency driving, where it is not possible to get an effective static system. This is a more long-term future goal. Finally, our work on driven systems has mainly dealt with closed systems. It would be of interest to understand the more general problem of driving in open systems.

Chapter 6

Appendix

6.1 Derivation of momentum space Hamiltonian for spin-orbit coupled Dirac materials

The tight binding Hamiltonian of silicene like materials [1] in real space include following terms [26] -

$$\begin{aligned} H &= -t\sum_{\langle i,j\rangle,\alpha\beta} c^{\dagger}_{i\alpha}c_{j\alpha} + l\,E_z\sum_{i,\alpha}\xi_i\; c^{\dagger}_{i\alpha}c_{j\alpha} - \mu\sum_{i,\alpha} c^{\dagger}_{i\alpha}c_{i\alpha} + \frac{i\lambda}{3\sqrt{3}}\sum_{\langle\langle i,j\rangle\rangle,\alpha,\beta}\nu_{i,j}\; c^{\dagger}_{i\alpha}\,\sigma^{z}_{\alpha\beta}\,c_{j\beta} \\ &\quad + i\,\lambda_{R_1}\sum_{\langle i,j\rangle} c^{\dagger}_{i\alpha}\left(\vec{\sigma}\times\vec{d}_{ij}\right)^{z}_{\alpha\beta}c_{j\beta} - i\,\lambda_{R_2}\sum_{\langle\langle i,j\rangle\rangle,\alpha\beta}\xi_i\; c^{\dagger}_{i\alpha}\left(\sigma\times\hat{d}_{ij}\right)^{z}_{\alpha\beta}c_{j\beta}. \end{aligned} \tag{6.1}$$

where, the first term represents the nearest neighbor hopping. Second term represents the staggered potential term which is arised due to buckled structure of these materials. Chemical potential term is given by the third term which is the on-site term. Last three terms represent the effective atomic spin-orbit coupling which is next nearest neighbour, extrinsic Rashbha spin-orbit which is induced by the external electric field which is the nearest neighbour and intrinsic Rashbha spin-orbit associated with the next nearest neighbour. Now, we Fourier transform each term to get the momentum space Hamiltonian.

Fourier transforming the atomic intrinsic SOC -

$$\begin{aligned} H_{\rm so} &= \frac{i\lambda}{3\sqrt{3}}\sum_{\langle\langle i,j\rangle\rangle,\alpha\beta}\nu_{i,j}\; c^{\dagger}_{i\alpha}\,\sigma^{z}_{\alpha\beta}\,c_{j\beta} \\ &= \frac{i\lambda}{3\sqrt{3}}\sum_{j,\alpha\beta}\left[\nu_{ij}\,a^{\dagger}_{k\alpha}a_{k\beta}\sigma^{z}_{\alpha\beta}e^{ik.a_j} + \nu_{ij}\,b^{\dagger}_{k\alpha}b_{k\beta}\sigma^{z}_{\alpha\beta}e^{ik.a_j}\right] \\ &= \frac{i\lambda}{3\sqrt{3}}\sum_{j}\left[a^{\dagger}_{k\uparrow}a_{k\uparrow}\nu_{ij}\,e^{ik.a_j} - a^{\dagger}_{k\downarrow}a_{k\downarrow}\nu_{ij}\,e^{ik.a_j} + b^{\dagger}_{k\uparrow}b_{k\uparrow}\nu_{ij}\,e^{ik.b_j} - b^{\dagger}_{k\downarrow}b_{k\downarrow}\nu_{ij}\,e^{ik.b_j}\right] \end{aligned}$$

[1] We call silicene like materials to the Dirac materials with spin-orbit coupling.

Now,

$$\begin{aligned}\sum_j \nu_{ij} e^{ik.a_j} &= \Big[e^{ik.a_1} - e^{ik.a_2} + e^{ik.a_3} - e^{ik.a_4} + e^{ik.a_5} - e^{ik.a_6}\Big] \\ &= \Big[e^{ik.a_1} - e^{ik.a_2} + e^{ik.a_3} - e^{-ik.a_1} + e^{-ik.a_2} - e^{-ik.a_3}\Big] \\ &= 2\,i\Big[\sin(k.a_1) - \sin(k.a_2) + \sin(k.a_3)\Big] \end{aligned} \tag{6.2}$$

and,

$$\begin{aligned}\sum_{j=1}^{6} \nu_{ij} e^{ik.b_j} &= -\sum_{j=1}^{6} \nu_{ij} e^{ik.a_j} \\ &= -2\,i\Big[\sin(k.a_1) - \sin(k.a_2) + \sin(k.a_3)\Big] \end{aligned} \tag{6.3}$$

The intrinsic Rashbha -

$$\begin{aligned} H_{R_2} &= -i\,\lambda_{R_2} \sum_{\langle\langle i,j\rangle\rangle} \xi_i\; c^{\dagger}_{i\alpha} \Big(\vec{\sigma} \times \hat{d}_{ij}\Big)^{z}_{\alpha\beta} c_{j\beta} + h.c. \\ &= -i\,\lambda_{R_2} \sum_{\langle\langle i,j\rangle\rangle} \xi_i\; c^{\dagger}_{i\alpha} \Big\{\Big(\sigma_y \hat{d}^z_{ij} - \hat{d}^y_{ij}\sigma_z\Big)\,\hat{i} - \Big(\sigma_x \hat{d}^z_{ij} - \sigma_z \hat{d}^x_{ij}\Big)\,\hat{j} + \Big(\sigma_x \hat{d}^y_{ij} - \sigma_y \hat{d}^x_{ij}\Big)\,\hat{k}\Big\}^{z}_{\alpha\beta} c_{j\beta} + h.c. \\ &= -i\,\lambda_{R_2} \sum_{\langle\langle i,j\rangle\rangle} \xi_i\; c^{\dagger}_{i\alpha} \Big(\sigma_x \hat{d}^y_{ij} - \sigma_y \hat{d}^x_{ij}\Big)\, c_{j\beta} + h.c. \\ &= -i\,\lambda_{R_2} \sum_{\langle\langle i,j\rangle\rangle} \Big[a^{\dagger}_{i\alpha} \Big(\sigma_x \hat{d}^y_{ij} - \sigma_y \hat{d}^x_{ij}\Big)\, a_{j\beta} - b^{\dagger}_{i\alpha} \Big(\sigma_x \hat{d}^y_{ij} - \sigma_y \hat{d}^x_{ij}\Big)\, b_{j\beta}\Big] + h.c. \end{aligned} \tag{6.4}$$

Let us focus on the A-sublattice -

$$= \lambda_{R_2} \sum_{\langle\langle i,j\rangle\rangle} \Big[a^{\dagger}_{i\alpha} \Big(-i\sigma_x \hat{d}^y_{ij} + i\sigma_y \hat{d}^x_{ij}\Big)\, a_{j\beta}\Big] + h.c. \tag{6.5}$$

Now, Fourier transforming this term -

$$\begin{aligned} &= \lambda_{R_2} \sum_{k,j,\alpha\beta} a^{\dagger}_{k\alpha} \Big(-i\sigma_x^{\alpha\beta} \hat{d}^j_y + i\sigma_y^{\alpha\beta} \hat{d}^j_x\Big)\, a_{k\beta}\; e^{ik.a^j} + h.c. \\ &= \lambda_{R_2} \sum_{k,j,\alpha\beta} \Big[a^{\dagger}_{k\alpha} \Big(-i\sigma_x^{\alpha\beta} \hat{d}^j_y + i\sigma_y^{\alpha\beta} \hat{d}^j_x\Big)\, a_{k\beta}\; e^{ik.a_j} - a^{\dagger}_{k\beta} \Big(-i\sigma_x^{\beta\alpha} \hat{d}^j_y + i\sigma_y^{\beta\alpha} \hat{d}^j_x\Big)\, a_{k\alpha}\; e^{-ik.a^j}\Big] \\ &= \lambda_{R_2} \sum_{k,j} \Big[a^{\dagger}_{k\uparrow} a_{k\downarrow} \Big(-i\hat{d}^j_y + \hat{d}^j_x\Big)\, e^{ik.a_j} + a^{\dagger}_{k\downarrow} a_{k\uparrow} \Big(-i\hat{d}^j_y - \hat{d}^j_x\Big)\, e^{ik.a_j} - a^{\dagger}_{k\uparrow} a_{k\downarrow} \Big(-i\hat{d}^j_y + \hat{d}^j_x\Big)\, e^{-ik.a_j} \\ &\quad -a^{\dagger}_{k\downarrow} a_{k\uparrow} \Big(-i\hat{d}^j_y - \hat{d}^j_x\Big)\, e^{-ik.a_j}\Big] \\ &= \lambda_{R_2} \sum_{k,j} \Big[a^{\dagger}_{k\uparrow} a_{k\downarrow} \Big(e^{ik.a_j} - e^{-ik.a_j}\Big) \Big(-i\hat{d}^j_y + \hat{d}^j_x\Big) - a^{\dagger}_{k\downarrow} a_{k\uparrow} \Big(e^{ik.a_j} - e^{-ik.a_j}\Big) \Big(i\hat{d}^j_y + \hat{d}^j_x\Big)\Big] \\ &= 2\,i\,\lambda_{R_2} \sum_{k,j} \sin(k.a_j) \Big[a^{\dagger}_{k\uparrow} a_{k\downarrow} \Big(-i\hat{d}^j_y + \hat{d}^j_x\Big) - a^{\dagger}_{k\downarrow} a_{k\uparrow} \Big(i\hat{d}^j_y + \hat{d}^j_x\Big)\Big] \\ &= 2\,i\,\lambda_{R_2} \sum_{k,j} \sin(k.a_j) \Big[a^{\dagger}_{k\uparrow} a_{k\downarrow}\; e^{-i\theta_j} - a^{\dagger}_{k\downarrow} a_{k\uparrow}\; e^{i\theta_j}\Big] \end{aligned} \tag{6.6}$$

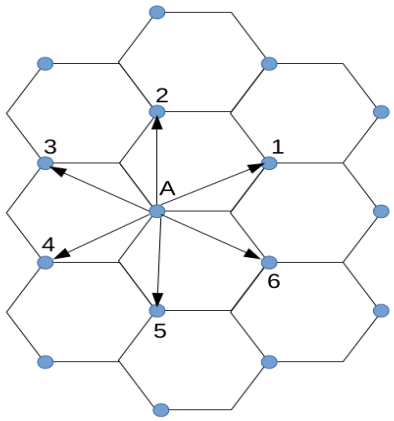

Figure 6.1: Next nearest neighbour for A and B sub lattice

where, θ_j is the angular direction of the NNN. There are six NNN for each sub lattice -

$$a_1 = -a_4 = a\left(\frac{3}{2}, \frac{\sqrt{3}}{2}\right), \quad a_2 = -a_5 = a\left(0, \sqrt{3}\right), \quad a_3 = -a_6 = a\left(\frac{-3}{2}, \frac{\sqrt{3}}{2}\right)$$

.

$$\Rightarrow \theta_1 = 30^0, \quad \theta_4 = \pi + \theta_1, \quad \theta_2 = 90^0, \quad \theta_5 = \pi + \theta_2, \quad \theta_3 = 120^0, \quad \theta_6 = \pi + \theta_3$$

$$\begin{aligned}
&= 2\,i\,\lambda_{R_2} \sum_k \Bigg[\sin(k.a_1)\left(a^\dagger_{k\uparrow}a_{k\downarrow}e^{-i\theta_1} - a^\dagger_{k\downarrow}a_{k\uparrow}e^{i\theta_1}\right) + \sin(k.a_4)\left(a^\dagger_{k\uparrow}a_{k\downarrow}e^{-i\theta_4} - a^\dagger_{k\downarrow}a_{k\uparrow}e^{i\theta_4}\right) \\
&\quad + \sin(k.a_2)\left(a^\dagger_{k\uparrow}a_{k\downarrow}e^{-i\theta_2} - a^\dagger_{k\downarrow}a_{k\uparrow}e^{i\theta_2}\right) + \sin(k.a_5)\left(a^\dagger_{k\uparrow}a_{k\downarrow}e^{-i\theta_5} - a^\dagger_{k\downarrow}a_{k\uparrow}e^{i\theta_5}\right) \\
&\quad + \sin(k.a_3)\left(a^\dagger_{k\uparrow}a_{k\downarrow}e^{-i\theta_3} - a^\dagger_{k\downarrow}a_{k\uparrow}e^{i\theta_3}\right) + \sin(k.a_6)\left(a^\dagger_{k\uparrow}a_{k\downarrow}e^{-i\theta_6} - a^\dagger_{k\downarrow}a_{k\uparrow}e^{i\theta_6}\right) \Bigg] \\
&= 2\,i\,\lambda_{R_2} \sum_k \Bigg[\sin(k.a_1)\left(a^\dagger_{k\uparrow}a_{k\downarrow}e^{-i\theta_1} - a^\dagger_{k\downarrow}a_{k\uparrow}e^{i\theta_1}\right) - \sin(k.a_1)\left(a^\dagger_{k\uparrow}a_{k\downarrow}e^{-i(\pi+\theta_1)} - a^\dagger_{k\downarrow}a_{k\uparrow}e^{i(\pi+\theta_1)}\right) \\
&\quad + \sin(k.a_2)\left(a^\dagger_{k\uparrow}a_{k\downarrow}e^{-i\theta_2} - a^\dagger_{k\downarrow}a_{k\uparrow}e^{i\theta_2}\right) - \sin(k.a_2)\left(a^\dagger_{k\uparrow}a_{k\downarrow}e^{-i(\pi+\theta_2)} - a^\dagger_{k\downarrow}a_{k\uparrow}e^{i(\pi+\theta_2)}\right) \\
&\quad + \sin(k.a_3)\left(a^\dagger_{k\uparrow}a_{k\downarrow}e^{-i\theta_3} - a^\dagger_{k\downarrow}a_{k\uparrow}e^{i\theta_3}\right) - \sin(k.a_3)\left(a^\dagger_{k\uparrow}a_{k\downarrow}e^{-i(\pi+\theta_3)} - a^\dagger_{k\downarrow}a_{k\uparrow}e^{i(\pi+\theta_3)}\right) \Bigg] \\
&= 2\,i\,\lambda_{R_2} \sum_k \Bigg[\sin(k.a_1)\left(a^\dagger_{k\uparrow}a_{k\downarrow}e^{-i\theta_1} - a^\dagger_{k\downarrow}a_{k\uparrow}e^{i\theta_1} + a^\dagger_{k\uparrow}a_{k\downarrow}e^{-i\theta_1} - a^\dagger_{k\downarrow}a_{k\uparrow}e^{i\theta_1}\right) \\
&\quad + \sin(k.a_2)\left(a^\dagger_{k\uparrow}a_{k\downarrow}e^{-i\theta_2} - a^\dagger_{k\downarrow}a_{k\uparrow}e^{i\theta_2} + a^\dagger_{k\uparrow}a_{k\downarrow}e^{-i\theta_2} - a^\dagger_{k\downarrow}a_{k\uparrow}e^{i\theta_2}\right) \\
&\quad + \sin(k.a_3)\left(a^\dagger_{k\uparrow}a_{k\downarrow}e^{-i\theta_3} - a^\dagger_{k\downarrow}a_{k\uparrow}e^{i\theta_3} + a^\dagger_{k\uparrow}a_{k\downarrow}e^{-i\theta_3} - a^\dagger_{k\downarrow}a_{k\uparrow}e^{i\theta_3}\right) \Bigg]
\end{aligned} \tag{6.7}$$

$$
\begin{aligned}
&= 4\,i\,\lambda_{R_2}\sum_k\Bigg[\sin(k.a_1)\left(a^\dagger_{k\uparrow}a_{k\downarrow}e^{-i\theta_1}-a^\dagger_{k\downarrow}a_{k\uparrow}e^{i\theta_1}\right)+\sin(k.a_2)\left(a^\dagger_{k\uparrow}a_{k\downarrow}e^{-i\theta_2}-a^\dagger_{k\downarrow}a_{k\uparrow}e^{i\theta_2}\right)\\
&\quad+\sin(k.a_3)\left(a^\dagger_{k\uparrow}a_{k\downarrow}e^{-i\theta_3}-a^\dagger_{k\downarrow}a_{k\uparrow}e^{i\theta_3}\right)\Bigg]\\
&= 4\,i\,\lambda_{R_2}\sum_k\Bigg[a^\dagger_{k\uparrow}a_{k\downarrow}\left\{\sin(k.a_1)e^{-i\theta_1}+\sin(k.a_2)e^{-i\theta_2}+\sin(k.a_3)e^{-i\theta_3}\right\}\\
&\quad-a^\dagger_{k\downarrow}a_{k\uparrow}\left\{\sin(k.a_1)e^{i\theta_1}+\sin(k.a_2)e^{i\theta_2}+\sin(k.a_3)e^{i\theta_3}\right\}\Bigg] \qquad (6.8)
\end{aligned}
$$

Similarly, for B-sub lattice -

$$
\begin{aligned}
&= -4\,i\,\lambda_{R_2}\sum_k\Bigg[b^\dagger_{k\uparrow}b_{k\downarrow}\left\{\sin(k.a_1)e^{-i\theta_1}+\sin(k.a_2)e^{-i\theta_2}+\sin(k.a_3)e^{-i\theta_3}\right\}\\
&\quad-b^\dagger_{k\downarrow}b_{k\uparrow}\left\{\sin(k.a_1)e^{i\theta_1}+\sin(k.a_2)e^{i\theta_2}+\sin(k.a_3)e^{i\theta_3}\right\}\Bigg] \qquad (6.9)
\end{aligned}
$$

Let us focus on the fifth term, the extrinsic Rashbha spin-orbit coupling -

$$
\begin{aligned}
H_{R_1} &= i\,\lambda_{R_1}\sum_{\langle i,j\rangle,\alpha\beta}\left[c^\dagger_{i\alpha}\left(\vec{\sigma}\times\hat{d}_{ij}\right)^z_{\alpha\beta}c_{j\beta}+h.c.\right]\\
&= i\,\lambda_{R_1}\sum_{\langle i,j\rangle,\alpha\beta}\left[c^\dagger_{i\alpha}\left\{\left(\sigma_y\hat{d}^z_{ij}-\hat{d}^y_{ij}\sigma_z\right)\hat{i}-\left(\sigma_x\hat{d}^z_{ij}-\sigma_z\hat{d}^x_{ij}\right)\hat{j}+\left(\sigma_x\hat{d}^y_{ij}-\sigma_y\hat{d}^x_{ij}\right)\hat{k}\right\}^z_{\alpha\beta}c_{j\beta}+h.c.\right]\\
&= i\,\lambda_{R_1}\sum_{\langle i,j\rangle,\alpha\beta}\left[c^\dagger_{i\alpha}\left(\sigma_x\hat{d}^y_{ij}-\sigma_y\hat{d}^x_{ij}\right)c_{j\beta}+h.c.\right]\\
&= \lambda_{R_1}\sum_{\langle i,j\rangle,\alpha\beta}\left[a^\dagger_{i\alpha}\left(i\sigma_x\hat{d}^y_{ij}-i\sigma_y\hat{d}^x_{ij}\right)b_{j\beta}+h.c.\right]\\
&= \lambda_{R_1}\sum_{k,j,\alpha\beta}\left[a^\dagger_{k\alpha}\left(i\sigma^{\alpha\beta}_x\hat{d}^j_y-i\sigma^{\alpha\beta}_y\hat{d}^j_x\right)b_{k\beta}e^{ik.b_j}+b^\dagger_{k\beta}\left(-i\sigma^{\beta\alpha}_x\hat{d}^j_y+i\sigma^{\beta\alpha}_y\hat{d}^j_x\right)a_{k\alpha}e^{-ik.b_j}\right]\\
&= \lambda_{R_1}\sum_{k,j}\Bigg[a^\dagger_{k\uparrow}b_{k\downarrow}(i\hat{d}^j_y-\hat{d}^j_x)e^{ik.b_j}+a^\dagger_{k\downarrow}b_{k\uparrow}(i\hat{d}^j_y+\hat{d}^j_x)e^{ik.b_j}\\
&\quad+b^\dagger_{k\uparrow}a_{k\downarrow}(-i\hat{d}^j_y+\hat{d}^j_x)e^{-ik.b_j}+b^\dagger_{k\downarrow}a_{k\uparrow}(-i\hat{d}^j_y-\hat{d}^j_x)e^{-ik.b_j}\Bigg]\\
&= \lambda_{R_1}\sum_{k,j}\Bigg[-a^\dagger_{k\uparrow}b_{k\downarrow}e^{-i\theta_j}e^{ik.b_j}+a^\dagger_{k\downarrow}b_{k\uparrow}e^{i\theta_j}e^{ik.b_j}+b^\dagger_{k\uparrow}a_{k\downarrow}e^{-i\theta_j}e^{-ik.b_j}-b^\dagger_{k\downarrow}a_{k\uparrow}e^{i\theta_j}e^{-ik.b_j}\Bigg] \qquad (6.10)
\end{aligned}
$$

$$
\begin{aligned}
\Rightarrow H_{\rm so} &= \frac{i\lambda}{3\sqrt{3}}\sum_j \Big[\, a^\dagger_{k\uparrow}a_{k\uparrow}\nu_{ij}\, e^{ik.a_j} - a^\dagger_{k\downarrow}a_{k\downarrow}\nu_{ij}\, e^{ik.a_j} + b^\dagger_{k\uparrow}b_{k\uparrow}\nu_{ij}\, e^{ik.b_j} - b^\dagger_{k\downarrow}b_{k\downarrow}\nu_{ij}\, e^{ik.b_j}\Big] \\
&= \frac{i\lambda}{3\sqrt{3}}\sum_j \Big[\nu_{ij}e^{ik.a_j}(a^\dagger_{k,\uparrow}a_{k,\uparrow} - a^\dagger_{k,\downarrow}a_{k,\downarrow}) + \nu_{ij}e^{ik.b_j}(b^\dagger_{k,\uparrow}b_{k,\uparrow} - b^\dagger_{k,\downarrow}b_{k,\downarrow})\Big] \\
&= \frac{i\lambda}{3\sqrt{3}}\, 2\,i\Big(\sin(k.a_1) - \sin(k.a_2) + \sin(k.a_3)\Big)\Big(a^\dagger_{k,\uparrow}a_{k,\uparrow} - a^\dagger_{k,\downarrow}a_{k,\downarrow} - b^\dagger_{k,\uparrow}b_{k,\uparrow} + b^\dagger_{k,\downarrow}b_{k,\downarrow}\Big) \\
&= \frac{-2\lambda}{3\sqrt{3}}\Big(\sin(k.a_1) - \sin(k.a_2) + \sin(k.a_3)\Big)\Big(a^\dagger_{k,\uparrow}a_{k,\uparrow} - a^\dagger_{k,\downarrow}a_{k,\downarrow} - b^\dagger_{k,\uparrow}b_{k,\uparrow} + b^\dagger_{k,\downarrow}b_{k,\downarrow}\Big) \qquad (6.11)
\end{aligned}
$$

Finally, the full Hamiltonian in momentum space can be written as -

$$
\begin{aligned}
H_{\rm free} &= -t\sum_k\Big(\gamma_k\, a^\dagger_{k,\uparrow}b_{k,\uparrow} + \gamma^*_k\, b^\dagger_{k,\uparrow}a_{k,\uparrow}\Big) - t\sum_k\Big(\gamma_k\, a^\dagger_{k,\downarrow}b_{k,\downarrow} + \gamma^*_k\, b^\dagger_{k,\downarrow}a_{k,\downarrow}\Big) \\
&\quad + l\,E_z\sum_k\, a^\dagger_{k\uparrow}a_{k\uparrow} + l\,E_z\sum_k\, a^\dagger_{k\downarrow}a_{k\downarrow} - l\,E_z\sum_k\, b^\dagger_{k\uparrow}b_{k\uparrow} - l\,E_z\sum_k\, b^\dagger_{k\downarrow}b_{k\downarrow} \\
&\quad - \mu\sum_k\Big[a^\dagger_{k\uparrow}a_{k\uparrow} + b^\dagger_{k\uparrow}b_{k\uparrow} - a^\dagger_{k\downarrow}a_{k\downarrow} - b^\dagger_{k\downarrow}b_{k\downarrow}\Big] \\
&\quad - \frac{2\lambda}{3\sqrt{3}}\sum_k\Big(\sin(k.a_1) - \sin(k.a_2) + \sin(k.a_3)\Big)\Big(a^\dagger_{k,\uparrow}a_{k,\uparrow} - a^\dagger_{k,\downarrow}a_{k,\downarrow} - b^\dagger_{k,\uparrow}b_{k,\uparrow} + b^\dagger_{k,\downarrow}b_{k,\downarrow}\Big) \\
&\quad + \lambda_{R_1}\sum_{k,j}\Big[-a^\dagger_{k\uparrow}b_{k\downarrow}e^{-i\theta_j}e^{ik.b_j} + a^\dagger_{k\downarrow}b_{k\uparrow}e^{i\theta_j}e^{ik.b_j} + b^\dagger_{k\uparrow}a_{k\downarrow}e^{-i\theta_j}e^{-ik.b_j} - b^\dagger_{k\downarrow}a_{k\uparrow}e^{i\theta_j}e^{-ik.b_j}\Big] \\
&\quad + \frac{8\,i}{3}\lambda_{R_2}\sum_k\Big[a^\dagger_{k\uparrow}a_{k\downarrow}\Big(\sin(k.a_1)e^{-i\theta_1} + \sin(k.a_2)e^{-i\theta_2} + \sin(k.a_3)e^{-i\theta_3}\Big) \\
&\quad - a^\dagger_{k\downarrow}a_{k\uparrow}\Big(\sin(k.a_1)e^{i\theta_1} + \sin(k.a_2)e^{i\theta_2} + \sin(k.a_3)e^{i\theta_3}\Big) \\
&\quad - b^\dagger_{k\uparrow}b_{k\downarrow}\Big(\sin(k.a_1)e^{-i\theta_1} + \sin(k.a_2)e^{-i\theta_2} + \sin(k.a_3)e^{-i\theta_3}\Big) \\
&\quad + b^\dagger_{k\downarrow}b_{k\uparrow}\Big(\sin(k\cdot a_1)e^{i\theta_1} + \sin(k.a_2)e^{i\theta_2} + \sin(k.a_3)e^{i\theta_3}\Big)\Big] \qquad (6.12) \\
&= t\sum_k\gamma_k\Big(a^\dagger_{k\uparrow}b_{k\uparrow} + a^\dagger_{k\downarrow}b_{k\downarrow}\Big) + t\sum_k\gamma^*_k\Big(b^\dagger_{k\uparrow}a_{k\uparrow} + b^\dagger_{k\downarrow}a_{k\downarrow}\Big) \\
&\quad + l\,E_z\sum_k\Big(a^\dagger_{k\uparrow}a_{k\uparrow} + a^\dagger_{k\downarrow}a_{k\downarrow}\Big) - l\,E_z\sum_k\Big(b^\dagger_{k\uparrow}b_{k\uparrow} + b^\dagger_{k\downarrow}b_{k\downarrow}\Big) \\
&\quad - \mu\sum_k\Big(a^\dagger_{k\uparrow}a_{k\uparrow} + b^\dagger_{k\uparrow}b_{k\uparrow} - a^\dagger_{k\downarrow}a_{k\downarrow} - b^\dagger_{k\downarrow}b_{k\downarrow}\Big) \\
&\quad + \sum_k\chi_{\rm so}\Big(a^\dagger_{k\uparrow}a_{k\uparrow} - a^\dagger_{k\downarrow}a_{k\downarrow} - b^\dagger_{k\uparrow}b_{k\uparrow} + b^\dagger_{k\downarrow}b_{k\downarrow}\Big) \\
&\quad + \sum_{k,j}\Big(-s_k\, a^\dagger_{k\uparrow}b_{k\downarrow} + s^*_{-k}\, a^\dagger_{k\downarrow}b_{k\uparrow} + s_{-k}\, b^\dagger_{k\uparrow}a_{k\downarrow} - s^*_k\, b^\dagger_{k\downarrow}a_{k\uparrow}\Big) \\
&\quad + \sum_k\Big(\eta_k\, a^\dagger_{k\uparrow}a_{k\downarrow} + \eta^*_k\, a^\dagger_{k\downarrow}a_{k\uparrow} - \eta_k\, b^\dagger_{k\uparrow}b_{k\downarrow} - \eta^*_k\, b^\dagger_{k\downarrow}b_{k\uparrow}\Big) \qquad (6.13) \\
&= \psi^\dagger_k \quad \mathcal{H}_{\rm free} \quad \psi_k \qquad (6.14)
\end{aligned}
$$

where,

$$\begin{aligned}
\gamma_k &= \sum_{i=1}^{3} e^{ik\cdot\delta_i} \\
\chi_{\rm so} &= \frac{-2\lambda}{3\sqrt{3}}\left(\sin(k.a_1)-\sin(k.a_2)+\sin(k.a_3)\right) \\
s_k &= \lambda_{R_1}\sum_{j=1}^{3} e^{-i\theta_j}e^{ik.b_j} \\
\eta_k &= \frac{8\,i\lambda_{R_2}}{3}\sum_{j}\sin(k.a_j)e^{-i\theta_j}
\end{aligned} \tag{6.15}$$

6.2 Derivation of B-W Hamiltonian from Fourier components of momentum space Hamiltonian

The Hamiltonian for ↑-spin charge carriers in silicene -

$$H(\mathbf{k},t)=\begin{pmatrix} \xi(\mathbf{k},t) & \delta(\mathbf{k},t) \\ \delta(\mathbf{k},t)^* & -\xi(\mathbf{k},t)\end{pmatrix} \tag{6.16}$$

where,

$$\begin{aligned}
\delta(\mathbf{k},t) &= t\left[e^{-i\left(\frac{\sqrt{3}}{2}k_x+\frac{1}{2}k_y\right)a_0}+e^{-i\left(-\frac{\sqrt{3}}{2}k_x+\frac{1}{2}k_y\right)a_0}+e^{ik_ya_0}\right] \\
\xi(\mathbf{k},t) &= i\Lambda\left[e^{-i\left(\frac{\sqrt{3}}{2}k_x-\frac{3}{2}k_y\right)a_0}-e^{i\left(\frac{\sqrt{3}}{2}k_x+\frac{3}{2}k_y\right)a_0}+e^{i\sqrt{3}k_xa_0}\right. \\
&\quad \left.-e^{-i\sqrt{3}k_xa_0}-e^{-i\left(\frac{\sqrt{3}}{2}k_x+\frac{3}{2}k_y\right)a_0}+e^{i\left(\frac{\sqrt{3}}{2}k_x-\frac{3}{2}k_y\right)a_0}\right]
\end{aligned} \tag{6.17}$$

With Pierels substitution -

$$\begin{aligned}
\delta(\mathbf{k},t) &= t\Big[e^{-i\left(\frac{\sqrt{3}}{2}k_x+\frac{1}{2}k_y\right)a_0}e^{-i\left(\frac{\sqrt{3}}{2}\cos\Omega t+\frac{1}{2}\sin\Omega t\right)\alpha}+e^{-i\left(-\frac{\sqrt{3}}{2}k_x+\frac{1}{2}k_y\right)a_0}e^{-i\left(-\frac{\sqrt{3}}{2}\cos\Omega t+\frac{1}{2}\sin\Omega t\right)\alpha} \\
&\quad +e^{ik_ya_0}e^{i(\sin\Omega t)\alpha}\Big] \\
\xi(\mathbf{k},t) &= i\Lambda\Big[e^{-i\left(\frac{\sqrt{3}}{2}k_x-\frac{3}{2}k_y\right)a_0}e^{-i\left(\frac{\sqrt{3}}{2}\cos\Omega t-\frac{3}{2}\sin\Omega t\right)\alpha}-e^{i\left(\frac{\sqrt{3}}{2}k_x+\frac{3}{2}k_y\right)a_0}e^{i\left(\frac{\sqrt{3}}{2}\cos\Omega t+\frac{3}{2}\sin\Omega t\right)\alpha} \\
&\quad +e^{-i\sqrt{3}k_xa_0}e^{-i(\sqrt{3}\cos\Omega t)\alpha}-e^{i\sqrt{3}k_xa_0}e^{i(\sqrt{3}\cos\Omega t)\alpha}-e^{-i\left(\frac{\sqrt{3}}{2}k_x+\frac{3}{2}k_y\right)a_0}e^{-i\left(\frac{\sqrt{3}}{2}\cos\Omega t+\frac{3}{2}\sin\Omega t\right)\alpha} \\
&\quad +e^{i\left(\frac{\sqrt{3}}{2}k_x-\frac{3}{2}k_y\right)a_0}e^{i\left(\frac{\sqrt{3}}{2}\cos\Omega t-\frac{3}{2}\sin\Omega t\right)\alpha}\Big]
\end{aligned}$$

To restore the Bloch form, we make a gauge transformation on B-sites,

$$c_{Bk}\rightarrow c_{Bk}\;e^{i\mathbf{k.a1}} \tag{6.18}$$

hence, we will get $\delta(\mathbf{k},\mathbf{t})$ as -

$$\begin{aligned}\delta(\mathbf{k},t) &= t\Big[e^{-i\left(\frac{\sqrt{3}}{2}k_x+\frac{3}{2}k_y\right)a_0}e^{-i\left(\frac{\sqrt{3}}{2}\cos\Omega t+\frac{1}{2}\sin\Omega t\right)\alpha}+e^{-i\left(-\frac{\sqrt{3}}{2}k_x+\frac{3}{2}k_y\right)a_0}e^{-i\left(-\frac{\sqrt{3}}{2}\cos\Omega t+\frac{1}{2}\sin\Omega t\right)\alpha}\\ &\quad+e^{i(\sin\Omega t)\alpha}\Big]\end{aligned}$$

There won't be any change in $\xi(\mathbf{k},\mathbf{t})$.

So, $\delta(\mathbf{k},\mathbf{t})$ and $\xi(\mathbf{k},\mathbf{t})$ in eq.(6.17) with Peierls substitution have following form -

$$\begin{aligned}\delta(\mathbf{k},t) &= t\Big[e^{-i\left(\frac{\sqrt{3}}{2}k_x+\frac{3}{2}k_y\right)a_0}e^{-i\left(\frac{\sqrt{3}}{2}\cos\Omega t+\frac{1}{2}\sin\Omega t\right)\alpha}+e^{-i\left(-\frac{\sqrt{3}}{2}k_x+\frac{3}{2}k_y\right)a_0}e^{-i\left(-\frac{\sqrt{3}}{2}\cos\Omega t+\frac{1}{2}\sin\Omega t\right)\alpha}\\ &\quad+e^{i(\sin\Omega t)\alpha}\Big]\\ \xi(\mathbf{k},t) &= i\Lambda\Big[e^{-i\left(\frac{\sqrt{3}}{2}k_x-\frac{3}{2}k_y\right)a_0}e^{-i\left(\frac{\sqrt{3}}{2}\cos\Omega t-\frac{3}{2}\sin\Omega t\right)\alpha}-e^{i\left(\frac{\sqrt{3}}{2}k_x+\frac{3}{2}k_y\right)a_0}e^{i\left(\frac{\sqrt{3}}{2}\cos\Omega t+\frac{3}{2}\sin\Omega t\right)\alpha}\\ &\quad+e^{-i\sqrt{3}k_xa_0}e^{-i(\sqrt{3}\cos\Omega t)\alpha}-e^{i\sqrt{3}k_xa_0}e^{i(\sqrt{3}\cos\Omega t)\alpha}-e^{-i\left(\frac{\sqrt{3}}{2}k_x+\frac{3}{2}k_y\right)a_0}e^{-i\left(\frac{\sqrt{3}}{2}\cos\Omega t+\frac{3}{2}\sin\Omega t\right)\alpha}\\ &\quad+e^{i\left(\frac{\sqrt{3}}{2}k_x-\frac{3}{2}k_y\right)a_0}e^{i\left(\frac{\sqrt{3}}{2}\cos\Omega t-\frac{3}{2}\sin\Omega t\right)\alpha}\Big]\end{aligned}$$

Fourier components of $\delta(\mathbf{k},\mathbf{t})$ and $\xi(\mathbf{k},\mathbf{t})$ -

If we have a function,

$$f(t)=e^{-i(\,\gamma_1 sin\,\phi+\gamma_2 cos\,\phi)}$$

Then the Fourier components of $f(t)$ will be -

$$f_n=J_n(\alpha)e^{-in\chi}$$

where, $\alpha=\sqrt{\gamma_1^2+\gamma_2^2}$ and $\chi=tan^{-1}\frac{\gamma_2}{\gamma_1}$

We have t-dependent exponential in each term of $\delta(\mathbf{k},\mathbf{t})$ and $\xi(\mathbf{k},\mathbf{t})$. We can use above result to find the fourier components of each time-dependent term.

We can write $\delta(\mathbf{k},\mathbf{t})$ and $\xi(\mathbf{k},\mathbf{t})$ as -

$$\begin{aligned}\delta(\mathbf{k},t) =& t\left[e^{-i\left(\frac{\sqrt{3}}{2}k_x+\frac{3}{2}k_y\right)a_0}f_1(t)+e^{-i\left(-\frac{\sqrt{3}}{2}k_x+\frac{3}{2}k_y\right)a_0}f_2(t)+f_3(t)\right]\\ \xi(\mathbf{k},t) =& i\Lambda\left[e^{-i\left(\frac{\sqrt{3}}{2}k_x-\frac{3}{2}k_y\right)a_0}f_4(t)-e^{i\left(\frac{\sqrt{3}}{2}k_x+\frac{3}{2}k_y\right)a_0}f_5(t)+e^{-i\sqrt{3}k_xa_0}f_6(t)\right.\\ &\left.-e^{i\sqrt{3}k_xa_0}f_7(t)+e^{-i\left(\frac{\sqrt{3}}{2}k_x+\frac{3}{2}k_y\right)a_0}f_8(t)-e^{i\left(\frac{\sqrt{3}}{2}k_x-\frac{3}{2}k_y\right)a_0}f_9(t)\right]\end{aligned}$$

Now the Fourier components of different functions will be -

$$\begin{aligned} f^n_{1,2}(t) &= J_n(\alpha)e^{\mp in\pi/3} \\ f^n_3(t) &= J_n(\alpha) \\ f^n_{4,5}(t) &= J_n(\sqrt{3}\,\alpha)e^{\pm in\pi/6} \\ f^n_{6,7}(t) &= J_n(\sqrt{3}\,\alpha)e^{\mp in\pi/2} \\ f^n_{8,9}(t) &= J_n(\sqrt{3}\,\alpha)e^{\mp in\pi/6} \end{aligned} \tag{6.19}$$

Hence, Fourier components of $\delta(\mathbf{k},\mathbf{t})$ becomes -

$$\begin{aligned} \delta_n(\mathbf{k},t) &= t\left[e^{-i\left(\frac{\sqrt{3}}{2}k_x+\frac{3}{2}k_y\right)a_0}J_n(\alpha)e^{-in\pi/3} + e^{-i\left(-\frac{\sqrt{3}}{2}k_x+\frac{3}{2}k_y\right)a_0}J_n(\alpha)e^{in\pi/3} + J_n(\alpha)\right] \\ &= tJ_n(\alpha)\left[e^{-i\left(\frac{\sqrt{3}}{2}k_x+\frac{3}{2}k_y\right)a_0}e^{-in\pi/3} + e^{-i\left(-\frac{\sqrt{3}}{2}k_x+\frac{3}{2}k_y\right)a_0}e^{in\pi/3} + 1\right] \\ &= tJ_n(\alpha)\left[e^{-i\frac{3}{2}k_ya_0}\left(e^{-i\frac{\sqrt{3}}{2}k_xa_0}e^{-in\pi/3} + e^{i\frac{\sqrt{3}}{2}k_xa_0}e^{in\pi/3}\right) + 1\right] \\ &= tJ_n(\alpha)\left[2e^{-i\frac{3}{2}k_ya_0}\cos(\frac{\sqrt{3}}{2}k_xa_0 + \frac{n\pi}{3}) + 1\right] \end{aligned} \tag{6.20}$$

Similarly, Fourier components of $\xi(\mathbf{k},\mathbf{t})$ becomes -

$$\begin{aligned} \xi_n(\mathbf{k},t) &= i\Lambda\Big[e^{-i\left(\frac{\sqrt{3}}{2}k_x-\frac{3}{2}k_y\right)a_0}J_n(\sqrt{3}\,\alpha)e^{in\pi/6} - e^{i\left(\frac{\sqrt{3}}{2}k_x+\frac{3}{2}k_y\right)a_0}J_n(\sqrt{3}\,\alpha)e^{-in\pi/6} \\ &\quad + e^{-i\sqrt{3}k_xa_0}J_n(\sqrt{3}\,\alpha)e^{-in\pi/2} - e^{i\sqrt{3}k_xa_0}J_n(\sqrt{3}\,\alpha)e^{in\pi/2} - e^{-i\left(\frac{\sqrt{3}}{2}k_x+\frac{3}{2}k_y\right)a_0}J_n(\sqrt{3}\,\alpha)e^{-in\pi/6} \\ &\quad + e^{i\left(\frac{\sqrt{3}}{2}k_x-\frac{3}{2}k_y\right)a_0}J_n(\sqrt{3}\,\alpha)e^{in\pi/6}\Big] \\ &= i\Lambda J_n(\sqrt{3}\,\alpha)\Big[e^{-i\left(\frac{\sqrt{3}}{2}k_x-\frac{3}{2}k_y\right)a_0}e^{in\pi/6} - e^{i\left(\frac{\sqrt{3}}{2}k_x+\frac{3}{2}k_y\right)a_0}e^{-in\pi/6} + e^{-i\sqrt{3}k_xa_0}e^{-in\pi/2} \\ &\quad - e^{i\sqrt{3}k_xa_0}e^{in\pi/2} - e^{-i\left(\frac{\sqrt{3}}{2}k_x+\frac{3}{2}k_y\right)a_0}e^{-in\pi/6} + e^{i\left(\frac{\sqrt{3}}{2}k_x-\frac{3}{2}k_y\right)a_0}e^{in\pi/6}\Big] \\ &= i\Lambda J_n(\sqrt{3}\alpha)\Big[e^{i\frac{3}{2}k_ya_0}2i\sin\left(-\frac{\sqrt{3}}{2}k_xa_0 + \frac{n\pi}{6}\right) - 2\,i\sin\left(\sqrt{3}k_xa_0 + \frac{n\pi}{2}\right) \\ &\quad + e^{-i\frac{3}{2}k_ya_0}2i\sin\left(-\frac{\sqrt{3}}{2}k_xa_0 - \frac{n\pi}{6}\right)\Big] \\ &= 2\Lambda J_n(\sqrt{3}\,\alpha)\Big[e^{i\frac{3}{2}k_ya_0}\sin\left(\frac{\sqrt{3}}{2}k_xa_0 - \frac{n\pi}{6}\right) - e^{-i\frac{3}{2}k_ya_0}\sin\left(\frac{\sqrt{3}}{2}k_xa_0 + \frac{n\pi}{6}\right) \\ &\quad + \sin\left(\sqrt{3}k_xa_0 + \frac{n\pi}{2}\right)\Big] \end{aligned} \tag{6.21}$$

If one considers A sublattice as B then $\xi_n(\mathbf{k},t)$ will be -

$$\begin{aligned}
\xi_n(\mathbf{k},t) &= i\Lambda\Big[e^{-i\left(\frac{\sqrt{3}}{2}k_x-\frac{3}{2}k_y\right)a_0}J_n(\sqrt{3}\,\alpha)e^{in\pi/6}-e^{i\left(\frac{\sqrt{3}}{2}k_x+\frac{3}{2}k_y\right)a_0}J_n(\sqrt{3}\,\alpha)e^{-in\pi/6} \\
&\quad + e^{-i\sqrt{3}k_xa_0}J_n(\sqrt{3}\,\alpha)e^{-in\pi/2}-e^{-i\left(\frac{\sqrt{3}}{2}k_x+\frac{3}{2}k_y\right)a_0}J_n(\sqrt{3}\,\alpha)e^{-in\pi/6} \\
&\quad -e^{i\sqrt{3}k_xa_0}J_n(\sqrt{3}\,\alpha)e^{in\pi/2}+e^{i\left(\frac{\sqrt{3}}{2}k_x-\frac{3}{2}k_y\right)a_0}J_n(\sqrt{3}\,\alpha)e^{in\pi/6}\Big] \\
&= i\Lambda J_n(\sqrt{3}\,\alpha)\Big[e^{-i\left(\frac{\sqrt{3}}{2}k_x-\frac{3}{2}k_y\right)a_0}e^{in\pi/6}-e^{i\left(\frac{\sqrt{3}}{2}k_x+\frac{3}{2}k_y\right)a_0}e^{-in\pi/6}+e^{-i\sqrt{3}k_xa_0}e^{-in\pi/2} \\
&\quad - e^{i\sqrt{3}k_xa_0}e^{in\pi/2}-e^{-i\left(\frac{\sqrt{3}}{2}k_x+\frac{3}{2}k_y\right)a_0}e^{-in\pi/6}+e^{i\left(\frac{\sqrt{3}}{2}k_x-\frac{3}{2}k_y\right)a_0}e^{in\pi/6}\Big] \\
&= i\Lambda J_n(\sqrt{3}\,\alpha)\Big[e^{i\frac{3}{2}k_ya_0}2\,i\sin\left(-\frac{\sqrt{3}}{2}k_xa_0+\frac{n\pi}{6}\right)-2\,i\sin\left(\sqrt{3}k_xa_0+\frac{n\pi}{2}\right) \\
&\quad +e^{-i\frac{3}{2}k_ya_0}2\,i\sin\left(-\frac{\sqrt{3}}{2}k_xa_0-\frac{n\pi}{6}\right)\Big] \\
&= 2\Lambda J_n(\sqrt{3}\,\alpha)\Big[e^{-i\frac{3}{2}k_ya_0}\sin\left(\frac{\sqrt{3}}{2}k_xa_0+\frac{n\pi}{6}\right)-e^{i\frac{3}{2}k_ya_0}\sin\left(\frac{\sqrt{3}}{2}k_xa_0-\frac{n\pi}{6}\right) \\
&\quad -\sin\left(\sqrt{3}k_xa_0+\frac{n\pi}{2}\right)\Big]
\end{aligned} \tag{6.22}$$

Now, the Fourier components of the Hamiltonian can be written as -

$$H_n(\mathbf{k},t)=\begin{pmatrix}\xi_n(\mathbf{k},t) & \delta_n(\mathbf{k},t)\\ \delta_n(\mathbf{k},t)^* & -\xi_n(\mathbf{k},t)\end{pmatrix} \tag{6.23}$$

where, the Fourier components of δ_n and ξ_n are given by eq.(6.20) and (6.21). Now, one can use the Fourier components of the Hamiltonian to derive the effective time-independent Hamiltonian using B-W expansion given by eq.(3.8) and (3.9).

Bibliography

[1] T. O. Wehling, A. M. Black-Schaffer, A. V. Balatsky, Advances in Physics, Vol **63**, Iss. 1 (2014).

[2] K. S. Novoselov, A. K. Geim, S. V. Morozov, D. Jiang, Y. Zhang, S. V. Dubonos, I. V. Grigorieva, A. A. Firsov, Science Vol. **306**, pp. 666-669 (2004); M. C. Lemme, T. J. Echtermeyer, M. Baus, H. Kurz, Ieee Electr Device L **28**, 282-284 (2007).

[3] Y.-W. Son, M. L. Cohen, and S. G. Louie, Phy. Rev. Lett. **97**, pp. 216803-1-216803-4 (2006).

[4] F. Xia, D. B. Farmer, Y. M. Lin, P. Avouris, Nano Lett. **10**, 715-178 (2010).

[5] Y. Zhang, T. T. Tang, C. Girit, Z. Hao, M. C. Martin, A. Zettl, M. F. Crommie, Y. R. Shen, F. Wang, Nature **459**, 820-823 (2009); S. Y. Zhou, G.-H. Gweon, A. V. Fedorov, P. N. First, W. A. de Heer, D.-H. Lee, F. Guinea, A. H. Castro Neto, A. Lanzara, Nature Materials **6**, 770-775 (2007).

[6] Y. Zhang, T. T. Tang, C. Girit, Z. Hao, M. C. Martin, A. Zettl, M. F. Crommie, Y. R. Shen, F. Wang; Nature **459**, 820-823 (2009); E. V. Castro, K. S. Novoselov, S. V. Morozov, N. M. R. Pers, J. M. B. Lopes dos Santos, J. Nilsson, F. Guinea, A. K. Geim, A. H. Castro Neto, Phys. Rev. Lett. **99**, 216802 (2007).

[7] F. D. M. Haldane, Phys. Rev. Lett. **61**, 18 (1988).

[8] F. Matusalem, D. S. Koda, F. Bechstedt, M. Marques, L. K. Teles, Scientific Reports **7**, Article number: 15700 (2017); S. Cahangirov, M. Topsakal, E. AkTURK, H. Sahin, and S. Ciraci, Phys. Rev. Lett. **102**, 236804 (2009); L. Tao, E. Cinquanta, D. Chiappe, C. Grazianetti, M. Fanciulli, M. Dubey, A. Molle, D. Akinwande, Nature Nanotechnology **10**, 227-231 (2015).

[9] Zeyuan Ni, Emi Minamitani, Yasunobu Ando, and Satoshi Watanabe, Phys. Rev. B **96**, 075427 (2017); M. Ezawa, J. Phys. Soc. Jpn **84**, 121003 (2015); M. Ezawa, J. Phys. Soc. Jpn. **81**, 064705 (2012); K. Shakouri, P. Vasilopoulos, V. Vargiamidis, F. M. Peeters, Phys. Rev. B **90**, 235423 (2014); M. Ezawa, Phys. Rev. Lett. **109**, 055502 (2012).

[10] G. Schmidt, D. Ferrand, L. W. Molenkamp, A. T. Filip, B. J. van Wees; Phys. Rev. B **62**, R4790(R) (2000); I. Zutic, J. Fabian, S. D. Sarma, Rev. Mod. Phys. **76**, 323 (2004); C. Chappert, A. Fert, F. N. V. Dau, Nature Materials **6**, 813-823 (2007); J. Schliemann, J. C. Egues, D. Loss, Phys. Rev. Lett. **90**, 146801 (2003); D. D. Awschalom, M. E. Flatte, Nature Physics **3**, 153-159 (2007).

[11] J. Cayssol, B. DÃra, F. Simon, and R. Moessner, Phys. Status Solidi **RRL 7**, 101 (2013); N. H. Lindner, G. Refael, and V. Galitski, Nat. Phys. **7** 490 (2011); N. H. Lindner, D. L. Bergman, G. Refael, and V. Galitski, Phys. Rev. B **87**, 235131 (2013); H. L. Calvo, H. M. Pastawski, S. Roche, and L. E. F. Foa Torres, Appl. Phys. Lett. **98**, 232103 (2011); P. Delplace, A. GÃmez-LeÃn, and

G. Platero, Phys. Rev. B **88**, 245422 (2013); A. G. Grushin, A. GÃmez-LeÃn, and T. Neupert, Phys. Rev. Lett. **112**, 156801 (2014).

[12] G. Jotzu, M. Messer, R. Desbuquois, M. Lebrat, T. Uehlinger, D. Greif, T. Esslinger, Nature **515**, 237-240 (2014); G. Liu, N. Hao, S.-L. Zhu, and W. M. Liu, Phys. Rev. A **86**, 013639 (2012); L.-K. Lim, C. Morais Smith, and A. Hemmerich, Phys. Rev. Lett. **100**, 130402 (2008); M. Aidelsburger, M. Lohse, C. Schweizer, M. Atala, J. T. Barreiro, S. Nascimbene, N. R. Cooper, I. Block, N. Goldman, Nature Physics **11** 162-166 (2015); A. R. Kolovsky, Europhys. Lett. **93**, 20003 (2011); C. E. Creffield and F. Sols, Europhys. Lett. **101**, 40001 (2013).

[13] T. Kitagawa, E. Berg, M. Rudner, E. Demler, Phys. Rev. B **82**, 235114 (2010).

[14] Y. H. Wang, H. Steinberg, P. Jarillo- Herrero, N. Gedik, Science **25**, Vol. 342, Issue 6157, pp. 453-457 (2013).

[15] L.-K. Lim, C. Morais Smith, and A. Hemmerich Phys. Rev. Lett. **100**, 130402 (2008)

[16] A. R. Kolovsky, Europhys. Lett. **93**, 20003 (2011); C. E. Creffield and F. Sols, Europhys. Lett. **101**, 40001 (2013).

[17] M. Aidelsburger, M. Lohse, C. Schweizer, M. Atala, J. T. Barreiro, S. Nascimbene, N. R. Cooper, I. Block, N. Goldman, Nature Physics **11** 162-166 (2015)

[18] Z. Qin, G. S. Jung, M. J. Kang, M. J. Buehler Science Advance **3**, 1 (2017)

[19] D. Szondy newatlas.com, retrieved 17 Feb 2017

[20] W. Cal, A. L. Moore, Y. Zhu, X. Li, S. Chen, L. Shl, R. S. Ruoff Graphene Grown by Chemical Vapor Deposition Nano Lett. **10** (5), pp 1645-1651 (2010)

[21] Jae-Ung Lee, D. Yoon, H. Kim, S. W. Lee, H. Cheong Phys. Rev. B **83**, 081419 (R) (2011)

[22] Q. Zheng, W. H. Ip, X. Lin, N. Yousefi, K. K. Yeung, Z. Ll, Jang-Kyo Kim ACS Nano bf5 (7), pp 6039-6051 (2011)

[23] A. H. Castro Neto, F. Guinea, N. M. R. Peres, K. S. Novoselov, A. K. Geim Rev. Mod. Phys. **81**, 109 (2009)

[24] Klitzing K. V., Dorda G., Pepper M. Phys. Rev. Lett. **45**, 494 (1980)

[25] Konig M., Wiedmann S., Brune C., Roth A., Buhmann H., Molenkamp LW, Qi XL, Zhang SC., Science 318, 766770 (2007)

[26] M. Ezawa Phys. Rev. Lett. **109**, 055502 (2012)

[27] C.-C. Liu, H. Jiang, Y. Yao Phys. Rev. B **84**, 195430 (2011)

[28] S. Ryu, Y. Hatsugai Topological origin of zero-energy edge states in particla-hole symmetric systems Phys. Rev. Lett **89**, 077002 (2002)

[29] W. Yao, S. A. Yang, Q. Niu Phy. Rev. Lett. **102**, 096801 (2009)

[30] M. S. Rudner, N. H. Lindner, E. Berg, and M. Levin, Phys. Rev. X **3**, 031005 (2013).

[31] P. Titum, E. Berg, M. S. Rudner, G. Refael, N. H. Lindner, Phys. Rev. X **6**, 021013 (2016).

[32] M. C. Rechtsman, J. M. Zeuner, Y. Plotnik, Y. Lumer, D. Podolsky, F. Dreisow, S. Nolte, M. Segev, and A. Szameit, Nature **496**, 196 (2013).

[33] G. Jotzu, M. Messer, R. Desbuquois, M. Lebrat, T. Uehlinger, and D. Greif Nature **515**, 237240 (2014)

[34] H. Lignier, C. Sias, D. Ciampini, Y. Singh, A. Zenesini, O. Morsch, E. Arimondo; Phys. Rev. Lett. **99**, 220403 (2007); E. Kierig, U. Schnorrberger, A. Schietinger, J. Tomkovic, M. K. Oberthaler; Phys. Rev. Lett. **100**, 190405 (2008); C. E. Creffield, D. Ciampini, O. Morsch, E. Arimondo; Phys. Rev. A **82**, 035601 (2010); A. Eckardt, M. Holthaus, H. Lignier, A. Zenesini, D. Ciampini, O. Morsch, E. Arimondo; Phys. Rev. A **79**, 013611 (2009);

[35] R. Ma, E. M. Tai, M. P. Preiss, S. W. Bakr, J. Simon, M. Greiner; Phys. Rev. Lett. **107**, 095301 (2011); A. Alberti, G. Ferrari, V. V. Ivanov, L. M. Chiofalo, M. G. Tino; New J. Phys. **12**, 065037 (2010); A. Alberti, V. V. Ivanov, M. G. Tino, G. Ferrari; Nat. Phys. **5**, 547 (2009); C. Sias, H. Lignier, Y. Singh, A. Zenesini, D. Ciampini, O. Morsch, E. Arimondo; Phys. Rev. Lett. **100**, 040404 (2008)

[36] A. Eckardt, C. Weiss, M. Holthaus; Phys. Rev. Lett. **95**, 260404 (2005); A. Zenesini, H. Lignier, D. Ciampini, O. Morsch, E. Arimondo; Phy. Rev. Lett. **102**, 100403;

[37] N. Gemelke, E. Sarajlic, Y. Bidel, S. Hong, S. Chu; Phys. Rev. Lett. **95**, 170404 (2005) S. W. Bakr, M. P. Preiss, M. Tai Eric, R. Ma, J. Simon, M. Greiner; Nature **480**, 500 (2011); V. C. Parker, L-C Ha, C. Chin; Nature **9**, 769 (2013) ; L-C Ha, L. W. Clark, C. V. Parker, B. M. Anderson, C. Chin; Phys. Rev. Lett. **114**, 055301 (2015)

[38] A. Eckardt, P. Hauke, P. Soltan-Panahi, C. Becker, K. Sengstock, M. Lewenstein, P. Windpassinger, K. Sengstock; EPL **89**, 10010 (2010); J. Struck, C. Ölschlager, R. Target Ie, P. Soltan-Panahi, A. Eckardt, M. Lowenstein, P. Windpassinger, K. Sengstock; Science **333**, 996 (2011)

[39] T. Oka and H. Aoki, Phys. Rev. B **79**, 081406(R) (2009).

[40] A. R. Kolovsky; Europhys. Lett. **93**, 20003 (2011); A. Bermudez, T. Schatz, D. Porras; Phys. Rev. Lett. **107**, 150501 (2011); M. Aidelsburger, M. Lohse, C. Schweizer, M. Atala, J. T. Barreiro, S. Nascimbene, N. R. Cooper, I. Bloch, N. Goldman; Nat. Phys. **11**, 162 (2015); G. Jotzu, M. Messer, R. Desbuquois, M. Lebrat, T. Uehlinger, D. Greif, T. Esslingen; Nature **515**, 237 (2014); H. Miyake, G. A. Siviloglou, C. J. Kennedy, W. C. Burton, W. Ketterle; Phys. Rev. Lett. **111**, 185302 (2013) M. Aidelsburger, M. Atala, M. Lohse, J. T. Barreiro, B. Paredes, I. Bloch; Phys. Rev. Lett. **111**, 185301 (2013); P. Hauke et al; Nat. Phys. **109**, 145301 (2012); J. Struck et al; Nat. Phys. **9**, 738 (2013)

[41] K. Jimenez-Garcia, L. J. LeBlanc, R. A. Williams, M. C. beeler, C. Qu, M. Gong, C. Zhang, I. B. Spielman; Phys. Rev. Lett. **114**, 125301 (2015)

[42] X. Luo, L. Wu, J. Chen, Q. Guan, K. Gao, Z-F Xu, L. You, R. Wang; Scientific Reports **6**, 18983 (2016)

[43] E. B. Fel'dman, Phys. Lett. A **104**, 479 (1984).

[44] F. Casas, J. A. Oteo and J. Ros, J. Phys. A: Math. Gen. **34**, 3379 (2001).

[45] E. S. Mananga and T. Charpentier, J. Chem. Phys. **135**, 044109 (2011)

[46] T. Kuwahara, T. Mori, and K. Saito, Annals of Physics **367**, 96-124 (2016).

[47] T. Mikami, S. Kitamura, K. Yasuda, N. Tsuji, T. Oka, and H. Aoki, Phys. Rev. B **93**, 144307 (2016).

[48] M. Bukov, L. DAlessio, and A. Polkovnikov, Advances in Physics **64**, 139 (2015).

[49] A. Eckardt and E. Anisimovas, New J. Phys. **17**, 093039 (2015).

[50] Master's thesis in Physics Niels Bohr Institute, University of Copenhagen

[51] Driven quantum systems

[52] A. Gomez-Leon, P. Delplace, G. Platero Phys. Rev. B **89**, 205408 (2014)

[53] A. Verdeny, A. Mielke, F. Mintert Phys. Rev. Lett. **111**, 175301 (2013)

[54] C. W. J. Beenakker Rev. Mod. Phys. **80**, 1337 (2008)

[55] C. W. J. Beenakker Phys. Rev. Lett **97**, 067007 (2006)

[56] Qing-feng Sun, X. C. Xie J. Phys.: Condens Matter **21**, 344204 (2009)

[57] J. Zou, G. Jin Europhys. Lett. **87**, 27008 (2009)

[58] H. Haugen, D. Huertas-Hernando, A. Brataas Phys. Rev. B **77**, 115406 (2008)

[59] Y. Hajati AIP Advance **5**, 047112 (2015)

[60] T. Yokoyama Phys. Rev. B **77**, 073413 (2008)

[61] T. Yokoyama, J. Linder Phys. Rev. B **83**, 081418 (2011)

[62] M. Zargar Shoushtari, Y. Hajati, B. Jafari Zadeh Solid State Communications **200**, 42 (2014)

[63] C. L. Kane, E. J. Mele Phys. Rev. Lett. **95**, 226801 (2005).

[64] S. Rachel, M. Ozawa Phys. Rev. B **89**, 195303 (2014).

[65] X. T. An, Y. Y. Zhang, J. J. Liu, S. S. Li New J. Phys. **14**, 083039 (2012).

[66] W. F. Tsai, C. Y. Huang, T. R. Chang, H. Lin, H. T. Jeng, A. Bansil Nat. Commun. **4**, 1500 (2013).

[67] K. Shakouri, H. Kimchi, M. Esmaeilzadeh, H. Mazidabadi, F. M. Peeters Phys. Rev. B **92**, 35413 (2015).

[68] T. Yokoyama Phys. Rev. B **87**, 241409 (2013)

[69] M. Ezawa New J. Phys. **14**, 033003 (2013)

[70] H. X. Yang, A. Hallal, D. Terrade, X. Waintal, S. Roche, M. Chshiev Phys. Rev. Lett. **110**, 046603 (2013)

[71] J. Zou, G. Jin, Y. Ma J. Phys. Cond. Matt. **87**, 241409 (2009)

[72] S. Datta, Electronic properties in mesoscopic systems (Cambridge University Press, Cambridge, 1995)

[73] J. S. Moodera, G. Mathon J. Magn. Mater **200**, 248 (1999)

[74] C. C. Liu, H. Jiang, Y. Yao Phys. Rev. B **84**, 195430 (2011)

[75] H. Haugen, D. Huertas-Hernando, A. Brataas Phys. Rev. B **77**, 115406 (2008)

[76] For reviews see X.-L. Qi and S.-C. Zhang, Rev. Mod. Phys. **83**, 1057 (2011); M. Z. Hasan and C. L. Kane, Rev. Mod. Phys. **82**, 3045 (2010)

[77] T. Kitagawa, E. Berg, M. Rudner, and E. Demler, Phys. Rev. B **82**, 235114 (2010).

[78] N. H. Lindner, G. Refael, and V. Galitski, Nature Phys. **7**, 490 (2011).

[79] B. Dora, J. Cayssol, F. Simon, and R. Moessner, Phys. Rev. Lett. **108**, 056602 (2012).

[80] Y. Wang, H. Steinberg, P. Jarillo-Herrero, and N. Gedik, Science **342**, 453 (2013).

[81] L. Jiang, T. Kitagawa, J. Alicea, A. R. Akhmerov, D. Pekker, G. Refael, J. I. Cirac, E. Demler, M. D. Lukin, and P. Zoller, Phys. Rev. Lett. **106**, 220402 (2011).

[82] A. Kundu and B. Seradjeh, Phys. Rev. Lett. **111**, 136402 (2013).

[83] Y. Li, A. Kundu, F. Zhong and B. Seradjeh, Phys. Rev. B **90**, 121401(R) (2014).

[84] Q. J. Tong, J. H. An, J. B. Gong, H. G. Luo, and C. H. Oh, Phys. Rev. B **87**, 201109 (R) (2013).

[85] Z. Gu, H.A. Fertig, D. P. Arovas, and A. Auerbach, Phys. Rev. Lett. **107**, 216601 (2011).

[86] A. Kundu, H.A. Fertig, and B. Seradjeh, Phys. Rev. Lett. **113**, 236803 (2014).

[87] P. Titum, N. H. Lindner, M. C. Rechtsman, and G. Refael, Phys. Rev. Lett. **114**, 056801 (2015).

[88] A. Farrell and T. Pereg-Barnea, Phys. Rev. Lett. **115**, 106403 (2015).

[89] D. Y. H. Ho and J. B. Gong, Phys. Rev. Lett. **109**, 010601 (2012).

[90] A. Kundu, H.A. Fertig and B. Seradjeh, Phys. Rev. Lett. **116**, 016802 (2016).

[91] J. Klinovaja, P. Stano, and D. Loss, Phys. Rev. Lett. **116**, 176401 (2016).

[92] H. Sambe, Phys. Rev. A **7**, 2203 (1973).

[93] S. Konschuh, M. Gmitra, and J. Fabian, Phys. Rev. B **82**, 245412 (2010).

[94] C. C. Liu, H. Jiang and Y. Yao, Phys. Rev. B **84**, 195430 (2011).

[95] C. C. Liu, H. Jiang and Y. Yao, Phys. Rev. B **84**, 195430 (2011).

[96] C. C. Liu, W. Feng and Y. Yao, Phys. Rev. Lett. **107**, 076802 (2011).

[97] M. Ezawa, Phys. Rev. Lett. **110**, 026603 (2013).

[98] Phys. Rev. Lett. **113**, 266801 (2014).

[99] T. Iadecola, T. Neupert, and C. Chamon, Phys. Rev. B **91**, 235133 (2015).

[100] L. D'Alessio and M. Rigol, Nature Communications **6**, 8336 (2015)

[101] K. I. Seetharam, C-E. Bardyn, N. H. Lindner, M. S. Rudner, and G. Refael, Phys. Rev. X **5**, 041050 (2015).

[102] A. Russomanno and E. G. Dalla Torre, Europhys. Lett. **115**, 30006 (2016).

[103] T. Mori, T. Kuwahara, and Keiji Saito, Phys. Rev. Lett. **116**, 120401 (2016).

[104] M. M. Maricq, Phys. Rev. B **25**, 6622 (1982).

[105] H. Dehghani, T. Oka, and A. Mitra, Phys. Rev. B **90**, 195429 (2014).

[106] T. Mori, Phys. Rev. A **91**, 020101(R) (2015).

[107] P. Mohan, R. Saxena, A. Kundu, S. Rao, Brillouin Wigner Theory for Floquet Topological Phase Transitions in Spin-orbit Coupled Materials, Phys. Rev. B **94**, 235419 (2016)

[108] A. Kundu, H.A. Fertig, and B. Seradjeh, Phys. Rev. Lett. **113**, 236803 (2014).

[109] P. M. Perez-Piskunow, L. E. F. Foa Torres, and G. Usaj, Physical Review A bf 91, 043625 (2015).

[110] P. M. Perez-Piskunow, G. Usaj, C. A. Balseiro, and L. E. F. Foa Torres Physical Review B, 89, 121401(R) (2014).

[111] L. E. F. Foa Torres, P. M. Perez-Piskunow, C. A. Balseiro, G. Usaj Phys. Rev. Lett. **113**, 266801 (2014).

[112] H. L. Calvo, H. M. Pastawski, S. Roche and L. E. F. Foa Torres, App. Phys. Lett. **98**, 232103 (2011); H. L. Calvo, P. M. Perez-Piskunow, S. Rocje and L. E. F. Foa Torres, App. Phys. Lett. 98, 232103 (2012); H. L. Calvo, P. M. Perez-Piskunow, H. M. Pastawski, S. Roche and L. E. F. Foa Torrres, Jnl of Phys; Cond,. Matt. **25**, 144202 (2013).

[113] J. Atteia, J. H. Bardarson and J. Cayssol, arXiv number, 1709.00090.

[114] M. A. Sentef, M. Claasen, A. F. Kemper, B. Moritz, T. Oka, J. K. Freericks and T. P. Devereaux, Nat. Comm. **6**, 7047 (2015).

[115] M. V. Fistul and K. B. Efetov, Phys. Rev. B **90**, 125416 (2014).

[116] B. Mukherjee, P. Mohan, D. Sen and K. Sengupta, arxiv number, 1709.06554.

[117] M. Rodriguez-Vega and B. Seradjeh, arxiv number, 1706.05303.

[118] T. Fukui, Y. Hatsugai, and H. Suzuki, J. Phys. Soc. Jpn. **74**, (2005) pp. 1674-1677.

[119] T. Mikami, S. Kitamura, K. Yasuda, N. Tsuji, T. Oka, and H. Aoki, Phys. Rev. B **93**, 144307 (2016).

[120] F. Gallego-Marcos, G. Platero, C. Nietner, G. Schaller, and T. Brandes, Phys. Rev. A **90**, 033614 (2014).

[121] Z. Yi-Fu, Y. Yun-You, J. Yan, S. Li, S. Rui, S. Dong-Ning and X. Ding-Yu, Chinese Physics B **22**, Number 11.

[122] P. Titum, E. Berg, M. S. Rudner, G. Refael, and N. H. Lindner, Phys. Rev. X **6**, 021013 (2016).

[123] A. Quelle, C. Weitenberg, K. Sengstock, and C. Morais Smith, arXiv:1704.00306.

[124] A. Kundu, M. Rudner, E. Berg, N. H. Lindner, arXiv:1708.05023.

[125] Aaron Farrell and T. Pereg-Barnea Phys. Rev. Lett. **115**, 106403 (2015).

[126] Aaron Farrell and T. Pereg-Barnea Phys. Rev. B **93**, 045121 (2016).

[127] H. H. Yap, L. Zhou, J.-S. Wang, and J. Gong, Phys. Rev. B **96**, 165443 (2017).

[128] A. A. Kaverzin, B. J. van Wees Phys. Rev. B **91**, 165412 (2015)

[129] A. Avsar, J. H. Lee, G. K. W. Koon, and B. Ozyilmaz, 2D Mater. **2**, 044009 (2015)

[130] Z. Jia, B. Yan, J. Niu, Q. Han, R. Zhu, D. Yu, and X. Wu, Phys. Rev. B **91**, 085411 (2015)

[131] F. Grusdt, T. Li, I. Bloch, E. Demler Phys. Rev. A **95**, 063617 (2017)

[132] L. Dong, L. Zhou, B. Wu, B. Ramachandran, H. Pu Phys. Rev. A **89**, 011602 (2014)

[133] Y. J. Lin, K. Jimenez-Garcia, I. B. Spielman Nature (London) **471**, 83 (2011)

[134] Y.-J. Lin, R. L. Compton, K. Jimenez-Garcia, W. D. Phillips, J. V. Porto, I. B. Spielman Nature Phys. **7**, 531 (2011)

[135] P. Wang, Z.-Q. Yu, Z. Fu, J. Miao, L. Huang, S. Chai, H. Zhai, J. Zhang Phys. Rev. Lett. **109**, 095301 (2012)

[136] L. W. Cheuk, A. T. Sommer, Z. Hadzibabic, T. Yefsah, W. S. Bakr, M. W. Zwierlein Phys. Rev. Lett. **109**, 095302 (2012)